



VCU

Virginia Commonwealth University
VCU Scholars Compass

Theses and Dissertations

Graduate School

2022

Novel Microfabricated Systems to Elucidate the Role of Anisotropic Stiffness in the Tumor Microenvironment

Jiten Narang
Virginia Commonwealth University

Follow this and additional works at: <https://scholarscompass.vcu.edu/etd>



Part of the [Molecular, Cellular, and Tissue Engineering Commons](#)

© The Author

Downloaded from

<https://scholarscompass.vcu.edu/etd/6957>

This Dissertation is brought to you for free and open access by the Graduate School at VCU Scholars Compass. It has been accepted for inclusion in Theses and Dissertations by an authorized administrator of VCU Scholars Compass. For more information, please contact libcompass@vcu.edu.

© Jiten D Narang _____ 2022
All Rights Reserved

Novel Microfabricated Systems to Elucidate the Role of Anisotropic Stiffness in the Tumor Microenvironment

A dissertation submitted in partial fulfillment of the requirement for the degree of
Doctor of Philosophy in Biomedical Engineering at Virginia Commonwealth
University.



By

Jiten D Narang
Bachelor of Science, Virginia Commonwealth University, 2012

Advisor: Dr. Christopher Lemmon
Associate Professor and Associate Department Chair
Biomedical Engineering

Virginia Commonwealth University
Richmond, Virginia
May 2022

ACKNOWLEDGEMENTS

I wish to thank Dr. Christopher Lemmon for his guidance, insightful discussions, and support on this work. I would like to thank Caleb Dalton, Devin Mair, and Lewis Scott for their direct contributions to this work, as well as current and prior members of the Lemmon Lab for their support. Finally, I would like to thank my family and most of all my amazing wife Juhi Khamar for the support and always pushing me to work harder.

TABLE OF CONTENTS

Cover Page.....	1
Acknowledgements.....	2
Table of Contents.....	3
List of Figures.....	4
Glossary.....	8
Abstract.....	10
Chapter 1: Introduction.....	13
Chapter 2: Background.....	19
Chapter 3: A novel multi-stiffness platform.....	30
Chapter 4: Investigating anisotropic stiffness in a breast cancer progression model.....	86
Chapter 5: Migratory response of cells to <i>in vitro</i> mimetics of Tumor-Associated Collagen Signature (TACS) biomechanics	150
Chapter 6: Summary and Future Directions.....	193
References.....	201
Curriculum Vitae.....	210

List of Figures

Figure 1: Multiphoton laser scanning microscopy image of TACS in a live mammary tumor	23
Figure 2: SEM image of oval and circular cross-section micropillars	26
Figure 3: Calculating forces from micropillar arrays	27
Figure 4: NIH-3T3s on circular micropillars	42
Figure 5: NIH-3T3s on oval micropillars	43
Figure 6: 3T3 cell area	45
Figure 7: 3T3 total fibril area	47
Figure 8: 3T3 cell forces on circular micropillars	50
Figure 9: Nuclear micropillar deflections of circular micropillars	51
Figure 10: 3T3 cell forces on oval micropillars	52
Figure 11: Nuclear micropillar deflections of oval micropillars	53
Figure 12: NIH-3T3 cell orientation rose plots	55
Figure 13: Analysis of 3T3 orientation	56
Figure 14: Immunofluorescence images of ASCs on circular micropillars	59
Figure 15: Immunofluorescence images of ASCs on oval micropillars	61
Figure 16: ASC cell area quantification	63
Figure 17: ASC total fibril area quantification	65
Figure 18: ASC force analysis on circular micropillars	68
Figure 19: ASC force analysis on oval micropillars	69
Figure 20: Rose plots of cell ASC alignment on circular and oval micropillars	71

Figure 21: ASC cell orientation quantification.....	72
Figure 22: 3T3 vs ASC cell area comparison.....	74
Figure 23: 3T3 vs ASC total fibril area comparison.....	75
Figure 24: 3T3 vs ASC total force comparison.....	79
Figure 25: 3T3 vs ASC force per cell area comparison.....	81
Figure 26: 3T3 vs ASC Orientation comparison.....	82
Figure 27: MCF10As on circular micropillars.....	94
Figure 28: MCF10As on oval micropillars.....	95
Figure 29: MCF-10A cell area.....	97
Figure 30: 10A Total fibril area quantification.....	99
Figure 31: Quantification of 10A traction forces on circular micropillar substrates.....	102
Figure 32: Quantification of 10A traction forces on oval micropillar substrates.....	103
Figure 33: Rose plots of 10A alignment.....	105
Figure 34: Quantification of 10A orientation on circular and oval micropillar substrates.....	106
Figure 35: MCF10AT1s on circular micropillars.....	109
Figure 36: MCF10AT1s on oval micropillars.....	110
Figure 37: MCF10AT1 cell area.....	112
Figure 38: MCF10AT1 Total fibril area quantification.....	114
Figure 39: Quantification of AT1 traction forces on circular micropillar substrates.....	117
Figure 40: Quantification of AT1 traction forces on oval micropillar substrates.....	118
Figure 41: Rose plots of AT1 alignment.....	120
Figure 42: AT1 alignment quantified on circular and oval micropillars.....	121
Figure 43: MDA-MB-231s on circular micropillars.....	124

Figure 44: MDA-MB-231s on oval micropillars.....	125
Figure 45: 231 Cell area on circular and oval micropillars.....	127
Figure 46: Quantification of 231 FN assembly on circular and oval micropillars.....	129
Figure 47: Analysis of 231 forces on circular micropillars.....	132
Figure 48: Analysis of 231 forces on oval micropillars.....	133
Figure 49: Rose plots of 231 orientation on circular and oval micropillars.....	135
Figure 50: 231 orientation quantification analysis on between circular and oval micropillars	136
Figure 51: Comparison of MCF10A, MCF10AT1, and MDA-MB-231 cell area on circular and oval micropillars.....	138
Figure 52: Total fibril area compared across MCF10A, MCF10AT1, and MDA-MB-231 on circular and oval micropillars	140
Figure 53: Epithelial cell traction forces on circular and oval micropillars.....	143
Figure 54: Epithelial cell total force normalized against cell area.....	145
Figure 55: 10A, AT1, and 231 cell orientations on oval micropillars.....	147
Figure 56: Translating TACS mechanics to a micropillar/microfluidic approach.....	153
Figure 57: TACS-Mimicking Micropillar Arrangements.....	154
Figure 58: Radial Microfluidic Assembly.....	157
Figure 59: Radial Microfluidic Assembly Within Specimen Holder.....	159
Figure 60: Top-down view Radial Microfluidic Assembly Within Specimen Holder.....	160
Figure 61: Inner reservoir tube setup.....	161
Figure 62: Radial Microfluidic On Custom Stage Insert.....	162
Figure 63: Microfluidic tube routing.....	163

Figure 64: Syringe pump and microscope arrangement.....	164
Figure 65: FITC Visualization of Chemoattractant Gradient Profiles.....	165
Figure 66: NIH-3T3 Migration On TACS 1 Design.....	171
Figure 67: NIH-3T3 Migration On Circumferential Design (TACS 2).....	172
Figure 68: NIH-3T3 Migration On Radial Design (TACS 3).....	173
Figure 69: 1% serum 3T3 migration analysis.....	176
Figure 70: 1% serum 3T3 displacement, persistence, and velocity analysis.....	179
Figure 71: Serum gradient 3T3 migration analysis.....	182
Figure 72: Serum gradient 3T3 displacement, persistence, and velocity analysis.....	184
Figure 73: R, S, and S/R comparison between 1% serum and serum gradient.....	188
Figure 74: Displacement, persistence, and velocity comparison between 1% serum and serum gradient experiments.....	190

GLOSSARY

Abbreviations

α -SMA	Alpha - Smooth Muscle Actin
ASC	Adipose derived Mesenchymal Stem Cell
ECM	Extracellular Matrix
FN	Fibronectin
HMSC	Human Mesenchymal Stem Cell
kPa	Kilopascal
MBC	Metastatic Breast Cancer
NHLF	Normal Human Lung Fibroblast
PDMS	Polydimethylsiloxane
TACS	Tumor Associated Collagen Signature
TGF- β 1	Transforming Growth Factor Beta 1
TME	Tumor Microenvironment
μ m	Micrometer (micron)
231CM	MDA-MB-231 Conditioned Media

Keywords

Mechanobiology

Tumor Microenvironment

Fibronectin

Tumor Associated Collagen signatures

Extracellular Matrix

Micropillar Array

Microfluidic

Breast Cancer

Abstract

NOVEL MICROFABRICATED SYSTEMS TO ELUCIDATE THE ROLE OF ANISOTROPIC STIFFNESS IN THE TUMOR MICROENVIRONMENT

By Jiten Narang Ph.D

A dissertation submitted in partial fulfillment of the requirement for the degree of Doctor of Philosophy in Biomedical Engineering at Virginia Commonwealth University.

Virginia Commonwealth University, 2022

Advisor: Dr. Christopher Lemmon
Associate Professor and Associate Department Chair
Biomedical Engineering

Cancer is the second leading cause of death in women and late stage (metastatic) cancers have abysmal survival rates compared to early stage regional cases (27% vs 86%). Thus, there is a great need to elucidate the mechanisms behind metastasis. Once malignant cells enter the vasculature it is nearly impossible to prevent the formation of distant metastases. We believe that the best stage for intervention is before or during malignant cell invasion into surrounding tissue. To develop new treatments at this stage, we need to develop a better understanding of the biomechanical and biochemical signals that drive invasion.

As a tumor grows, it progresses through three distinctly identifiable extracellular matrix (ECM) morphologies known as Tissue Associated Collagen Signatures (TACS): TACS 1, a small, dense region of increased collagen content, TACS 2, circumferentially aligned collagen fibers encapsulating the central cell mass, and TACS 3, tracks of collagen fibers leading perpendicularly away from the tumor. These TACS arrangements provide unique mechanical cues: increased

stiffness and aligned collagen fiber architecture. In TACS 3 specifically, the mechanical cues greatly promote stromal invasion. Turnover of healthy matrix with dense collagen rich matrix also constricts local vasculature and impedes the delivery of key nutrients and signaling molecules to malignant cells inside the tumor. Instead, these nutrients and signaling molecules are delivered outside the tumor and rely on diffusion to reach the malignant cells. This creates a chemotactic gradient where there is a high concentration of these factors outside the tumor and a low concentration inside the tumor. Both biomechanical and biochemical cues play important roles in facilitating malignant cell invasion into the stromal tissue in metastasis.

In this work we developed two novel assays to study these phenomena *in vitro*. We first developed a novel substrate composed of circular and oval cross section micropillars to study the effect of mechanical cues on cell behavior. Oval micropillars present mechanical cues (anisotropic stiffness and contact guidance) like those provided by collagen fibers in TACS arrangements. By studying cell behavior on our novel substrate, we were able to gain a better understanding of how mechanical cues affect cell alignment, size, ECM assembly, and traction force. Using methods to downregulate (Y-27632 and blebbistatin) and upregulate (MDA-MB-231 conditioned media) traction force, we demonstrate that fibroblasts (NIH-3T3 and adipose derived stem cells (ASC)) feel the mechanical properties of their surroundings by applying force and downregulating force disrupts mechanoresponse.

Second, we developed a novel multi-cue microfluidic assay to simulate both biomechanical and biochemical cues of the tumor microenvironment concurrently. NIH-3T3s were used to demonstrate that migration is primarily influenced by TACS mimicking mechanical cues and chemotactic gradients failed to alter migration characteristics significantly. We conclude that, at least in fibroblasts, mechanical cues dominate chemotactic cues in directed migration. To

summarize, in this work we demonstrate that oval micropillars can influence key cellular behaviors such as alignment, migration, spreading, ECM assembly, and traction force. We also developed and characterized a novel multi-cue assay capable of mimicking the unique combination of biomechanical and biochemical cues present in tumor development. The results from these experiments imply that mechanical cues influence cell behavior greater than chemotactic cues.

Chapter 1

Introduction

Cancer is the second leading cause of death in women; breast cancer alone is responsible for approximately 30% of all new cases^{1,2}. Although early stage cancer survival rates have greatly improved (99% in local and 86% in regional), late stage survival rates remain abysmal (27% in distant or metastatic)³. This clearly presents the need for a deeper understanding of the mechanisms behind metastasis so that we may develop new treatments and minimize deaths due to metastatic breast cancer (MBC). Metastasis is the process where malignant cells leave the primary tumor, migrate to a new area of the body via vasculature, and develop another tumor. Signals that promote metastasis can be broken down into two main categories: biochemical and biomechanical. Biochemical signals consist of chemokine gradients between the tumor and stromal tissues. Many studies have demonstrated that biochemical signals, such as epidermal growth factor (EGF),

vascular endothelial growth factor (VEGF), fibroblast growth factor (FGF), platelet-derived growth factor (PDGF), normoxia and high glucose concentration, form gradients which can draw cells out of less favorable conditions within the tumor⁴⁻⁶. Biomechanically, greater extracellular matrix (ECM) stiffness due to increased collagen content and aligned architecture also promotes invasive behavior^{4,7-9}.

As a tumor grows, it progresses through three distinctly identifiable ECM morphologies known as Tissue Associated Collagen Signatures (TACS): TACS 1, a small, dense region of increased collagen content, TACS 2, circumferentially aligned collagen fibers encapsulating the central cell mass, and TACS 3, tracks of collagen fibers leading perpendicularly away from the tumor through the circumferential layer^{9,10}. Many studies have demonstrated that aligned microarchitecture promotes cell alignment and persistent migration using various *in vitro* methods, such as aligned collagen scaffolds, silk scaffolds, microcontact printed lines, microfabricated line structures, and microfabricated oval micropillars¹¹⁻¹⁴. The collagen-rich ECM also significantly increases regional tissue stiffness, and numerous studies have correlated this with increased metastatic potential^{8,15,16}. The aforementioned studies demonstrate the significance of biochemical and biomechanical signals in metastasis. Many of them rely on techniques that singularly recapitulate either chemical or mechanical signaling mechanisms; individually, these phenomena provide useful but incomplete data. In order to accurately mimic *in vivo* conditions, cells must be exposed to a combination of biochemical and biomechanical signals. Few have studied these effects concomitantly, and, to date, none have examined this relationship using mechanical representations of each TACS scenario. Traditional chemotherapies work well through early-stage cancers prior to metastasis, but poorly after. Treatments that could prevent or slow cancers from reaching a metastatic stage or prevent malignant cells from escaping the primary tumor would

greatly increase survival rates. We believe that preventing biomechanical changes, such as increased collagen content, increased stiffness, and aligned ECM architecture, may be a viable treatment option.

To develop therapeutics against these biomechanical changes, we need to better understand how biochemical and biomechanical signals work together to drive ECM turnover and reorganization. Through this work, we gained a better understanding of cellular response to anisotropic stiffness, aligned topographies, and chemotactic gradients.

In the following chapters, we began by demonstrating that anisotropic stiffness and contact guidance provided by oval micropillars mediate cell alignment, size, and ECM assembly. We demonstrated that cells “feel” the mechanical properties of their surroundings using force, and that mechanoresponse can be downregulated by using force inhibitors, such as Y27632 and blebbistatin. We also demonstrated that stimulating cells with conditioned media from metastatic cells promotes increased cell size and ECM assembly. Next, we used this knowledge to develop a novel migration assay to mimic the three distinct biomechanical phases across a tumor life span. The assay enabled us to study how various biomechanical scenarios, in the form of various ECM architectures, influence malignant cell invasion into the surrounding stromal tissue. Stromal invasion, the first step of metastasis, is the ideal step at which to develop preventative measures; once malignant cells enter the vasculature, it becomes nearly impossible to prevent the formation of distant metastases. We demonstrated that radially aligned fibers of collagen, a hallmark of a tumor at the metastatic stage, greatly enhance malignant cell invasion. Therefore, blocking mechanisms by which cells sense the mechanical stimuli provided by aligned collagen fibers could greatly decrease stromal invasion, and consequently, reduce the severity of metastatic cancer.

In essence, we developed a tool that mimics the biochemical and biomechanical signals in the tumor microenvironment simultaneously. It allowed us to better understand which signals promote metastasis, and the timeframe in which they do so, but ultimately, it will serve as a representative testing platform for potential therapies. In the following chapters, we describe the approach we took to probe cell mechanoresponse and create biochemically and biomechanically relevant *in vitro* models of the tumor microenvironment.

In Chapter 3, we begin by developing a novel microfabricated platform that presents cells with regions of both isotropic and anisotropic stiffness within a single sample. Many tissues in the body have anisotropic mechanical properties, so using isotropic substrates, such as glass or tissue culture polystyrene (TCPS), can present cells with grossly misrepresentative mechanical stimuli. Not only do they fail to recapitulate the anisotropy of *in vivo* ECM, but traditional substrates like glass and TCPS present substrate stiffnesses orders of magnitude greater than most soft tissues in the body¹⁷. Studying cell behavior on these substrates can yield unrepresentative data, substrate stiffness has been shown to influence an inflammatory-like response, or activation, in some cells, while even guiding differentiation in others¹⁸⁻²⁰.

Using microfabrication techniques, we developed a substrate with both isotropic and anisotropic stiffness surfaces much closer to *in vivo* values (5-40 kPa). We utilized circular cross section micropillars to represent isotropic tissues and oval cross section micropillars to mimic tissues with anisotropic stiffness and aligned ECM. Fibroblast cell lines, well known to respond to mechanical cues, were used to validate the effectiveness of the mechanical stimuli provided by our platform. Our novel substrate, with both isotropic and anisotropic areas, allowed us to study a single population of cells, on a single sample, while exposed to two distinctly different mechanical

environments. The results discussed in this chapter support our theory that various mechanical scenarios drive changes in cell behavior and morphology.

Next, in Chapter 4, we utilized our validated microfabricated substrate in a breast cancer progression model. It is well known that as a tumor grows, it remodels the surrounding ECM to include more collagen; these collagen fibers are assembled in a linearly aligned architecture⁹. This remodeled ECM presents two distinct mechanical cues: 1) increased regional stiffness and 2) and aligned topography. We utilized our oval micropillars to simulate this environment to and observed how changes in the ECM of the tumor microenvironment influence cell alignment, ECM assembly, and traction forces.

Often, as these ECM changes are occurring, we also observe an increase in epithelial cell malignancy. As epithelial cells become increasingly malignant, they display weaker cell-cell junctions, mesenchymal morphology, and increased motility²¹. To mimic this transition, we seeded cell lines of increasing malignancy (MCF10A, MCF10AT1, and MDA-MB-231) on our novel platform and examined their response to anisotropic mechanical stimuli. Our results suggest that epithelial cells are minimally mechanoresponsive but do show changes in response to inflammatory cytokine signaling.

Finally, we wanted to build on our base knowledge of biomechanical response in a tumor microenvironment, which we developed in Chapter 4, by utilizing oval micropillars to mimic the collagen architectures of the tumor microenvironment in a live cell migration assay. To reiterate, these various stages of tumor ECM architectures are commonly known as tumor associated collagen signatures (TACS). In Chapter 5, we developed a migration assay which not only mimics the mechanical stimuli exhibited at each TACS stage, but also recreates *in vivo* chemotactic gradients which help promote stromal invasion. By simulating both stimuli *in vitro*, we elucidated

the underlying roles of each signaling mechanism in promoting malignant cell invasion. Our novel migration assay provides a better *in vitro* model of invasion to test novel therapies. Testing each TACS stage will allow us to determine the timeframe during which each signal is most dominant, and when therapies can be applied for maximum efficacy.

Overall, in this work we discuss the development of a novel anisotropic platform to simulate the mechanical properties of anisotropic tissues *in vitro*. We then demonstrated the utility of our novel platform by investigating the role of anisotropic mechanical properties in tumor progression. Finally, we discuss the significant progress made towards developing a microfluidic system to replicate chemotactic gradients and TACS biomechanics of the tumor microenvironment.

Chapter 2

Background

2.1 Cancer: Cancer is the second leading cause of death in women, and breast cancer alone is responsible for approximately 30% of all new cases^{1,2}. Although early stage cancer survival rates have greatly improved (99% in local and 86% in regional), late stage survival rates remain abysmal (27% in distant or metastatic)³. This clearly presents the need for a deeper understanding of the mechanisms behind metastasis so that we may develop new treatments to minimize deaths from metastatic breast cancer (MBC).

2.2 Metastasis: Metastasis is the process during which malignant cells leave the primary tumor, migrate through stromal tissue, enter the vasculature, travel to a distant site, and form a new colony²². Metastatic cancer greatly decreases survival rates due to the difficulty in application of targeted therapies. Metastasis is potentiated by biochemical and biomechanical cues which influence malignant cells to leave the primary tumor. As a tumor grows, the ECM remodeling that

occurs serves as the basis for development of two migratory cues. The deposition of dense collagen fibers limits vascularization, leading to low levels of growth factors, nutrients, and oxygen inside the tumor. This creates chemotactic gradients, which influence cells to find more favorable conditions outside the tumor^{5,23,24}.

Increased collagen deposition is also responsible for biomechanical cues by way of 1) increasing tissue stiffness and 2) aligned fiber architecture. It is known that cells exhibit enhanced migration on stiffer surfaces, or on surfaces with stiffness gradients; this method of migration is coined durotaxis^{14,25,26}. Previous works have also demonstrated that ECMs with aligned fiber architecture also elicit enhanced persistent migration²⁷⁻²⁹. Both biochemical and biomechanical cues presented above promote the migration of malignant cells into the stroma. We believe that intervention at this step, known as invasion, provides the best opportunity to mitigate metastasis and increase survival rates.

2.3 Chemotactic Signaling In The Tumor Microenvironment: As mentioned above, dense collagen deposition in tumor growth limits vascularization throughout the tumor, leaving diffusion as the only method of transport for nutrients and growth factors to reach internal cells. As the tumor grows larger, the distance between internal cells and the tumor boundary grows, increasing the distance that cytokines need to diffuse across. This results in a multi-factor chemotactic gradient that stimulates invasion. Some of these factors, that have been demonstrated *in vitro* to elicit a strong migratory response, include glucose, epidermal growth factor (EGF), fibroblast growth factor (FGF), vascular endothelial growth factor (VEGF), platelet derived growth factor (PDGF), and oxygen^{5,6}.

2.4 ECM Remodeling In The Tumor Microenvironment: As a tumor grows, it progresses through three main stages of ECM remodeling. First, cells begin to degrade and replace the healthy

ECM with a collagen-rich composition resulting in a locally dense region of collagen matrix (Fig 1A). Second, the ECM is reorganized so that the tumor is encapsulated in long, circumferentially aligned, collagen fibers surrounding the inner cell mass (Fig 1B). Finally, metastasizing cells tunnel through the encapsulating layer and begin migrating away from the tumor. As they migrate, they degrade and reorganize the ECM (both within the collagen layer and stromal tissue surrounding it) forming tracks of aligned collagen fibers leading away from the tumor (Fig 1C). These three ECM arrangements are often referred to as Tissue Associated Collagen Signatures (TACS) 1,2 and 3¹⁰.

The collagen tracks are tunnels which provide a path of least resistance for following cells while also enhancing their migration by providing anisotropic stiffness and contact guidance cues. During these stages, not only does the local stiffness of the tissue increase, it increases in an anisotropic manner¹¹. Imagine a piece of string with tension applied at both ends; once completely taut, the string provides a strong resistance against tensile loads. However, if we were to grab the string in the middle and try to deflect (pull or push) it orthogonally, one would find that the string deflects easily. This analogy can be scaled up to a woven blanket and then to layers of woven blankets. One would observe that the layers provide greater resistance (stiffness) against loads applied in the tensile direction when compared to loads applied orthogonally. We predict that the circumferential collagen layers that encapsulate the tumor provide anisotropic stiffness cues (dual stiffness) in a similar fashion; exhibiting greater stiffness along the circumferential axis versus the perpendicular direction^{30,31}. In conjunction with anisotropic stiffness, we believe that aligned collagen fibers also provide contact guidance cues which influence cells to migrate in a circumferential manner in TACS 2. In the same manner, we predict that collagen tracks enhance outward migration in TACS 3.

It is not well understood how the aforementioned biomechanical signals of each TACS scenario interact with biochemical signals to promote tumor development and metastasis. Do they work together constructively or destructively, and how does the relationship vary as a function of tumor stage?

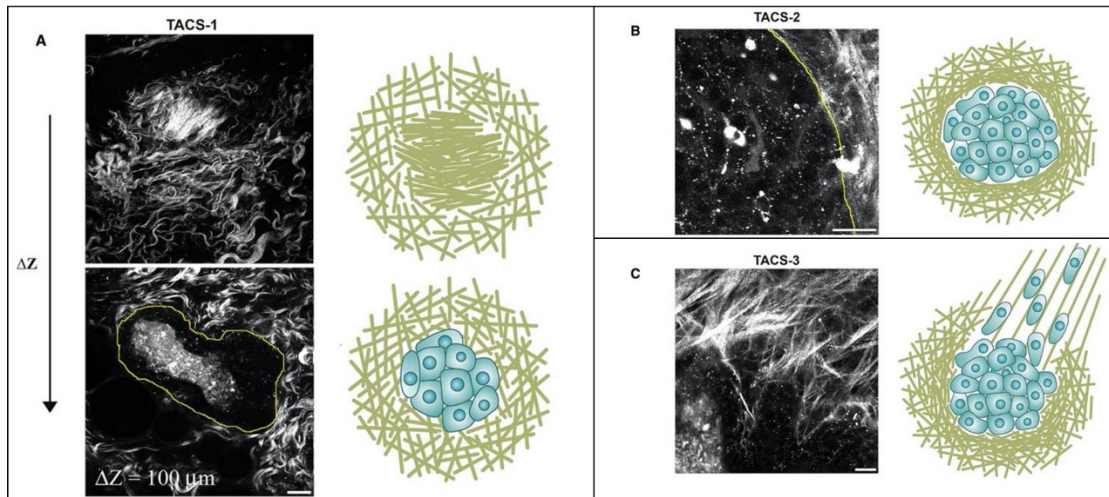


Figure 1: Multiphoton laser scanning microscopy image of TACS in a live mammary tumor

(A) TACS-1: The top image shows a small, dense region of collagen surrounded by wavy collagen. The bottom image is a cross section through the middle of the tumor showing a lack of ECM where the central cell mass is located. (B) TACS-2: At the next stage of tumor growth collagen fibers align parallel (circumferential alignment) to the tumor boundary. (C) TACS-3: Finally, at the metastatic stage, collagen fibers are aligned perpendicular (radial alignment) to the boundary.

Reproduced with permission from Provenzano et al. ³²

2.5 Modeling Anisotropic Stiffness And Aligned Topographies In Vitro: Most *in vitro* models of substrate stiffness utilize gels or polymers with isotropic stiffness; that is, uniform stiffness regardless of which direction the substrate is strained. In contrast, the tumor microenvironment, as described above, is anisotropic and varies depending on which direction it is strained. Other works have described the development of various tools to recapitulate anisotropic stiffness, but none have the customizability of oval micropillars. Stressed thin films are easy to produce and set up but are limited in stiffness range, and, under high strain, buckle in the perpendicular direction³³. Aligned collagen scaffolds excel at providing regions of linearly aligned fibers but do not allow circumferential fiber alignment or multiple regions with varied mechanical properties^{29,31,34}. Polyacrylamide gels can be created in a wide range of stiffness and even multiple regions of different stiffnesses, but they fail to replicate anisotropic cues present in many tissues^{35,36}. Microcontact printed lines allow users to generate various patterns for contact guidance but fail to present anisotropic stiffness and regions of various stiffness^{37,38}. Microfabricated line structures allow determination of effective substrate stiffness and contact guidance, but again, only in a linear fashion³⁹. We believe oval micropillars are best suited for the task because we can easily modulate substrate stiffness, anisotropic stiffness, directional contact guidance cues, and have local regions with different mechanical properties^{40,41}.

2.6 Micropillar Arrays: Micropillars were originally developed as a technique to quantify the forces that cells exert on their environment⁴². Micropillars are elastomeric pillars which cells sit on top of, attach to, and deflect. When used to measure cellular forces, they are generally created with diameters of 2-5 μm and heights of 5-12 μm (Fig 2). Forces are calculated by first taking images at the top and bottom surfaces to measure deflection (Fig 3B). Utilizing known mechanical properties and beam bending theory, we can back calculate how much force was exerted by the

cell (Fig 3A). Depending on cell type, a single cell may occupy anywhere from 10 to 150 micropillars. Force vectors are calculated at each attachment site and summed to generate total force. Summing the force vectors allows for the generation of a net force vector, which can indicate if the cell was stationary or migrating, and the direction of movement. (Fig 3C).

Micropillars are fabricated from a unique bio-compatible silicone polymer called polydimethylsiloxane (PDMS). PDMS is formed using two viscous components, a base and a crosslinker, which can be mixed at various ratios to modify its bulk elastic modulus. Essentially, increasing the quantity of crosslinker in the mix increases its stiffness. Once mixed, PDMS is heat cured in an oven, resulting in a rigid viscoelastic material. The stiffness of the micropillars can be tuned by modifying diameter (increasing diameter results in increased stiffness), height (decreasing pillar height results in increased stiffness), and the PDMS blend as mentioned above. Micropillars of circular cross-section are ideal for measuring cell-generated forces due to their isotropic nature; they require the same amount of force to be deflected in any direction. In this work, I have utilized a less common variation: micropillars of oval cross-section, which have anisotropic stiffness. They present both a high stiffness along the major axis and a low stiffness along the minor axis. Their elongated shape also provides a contact guidance cue which cells often use to orient themselves. Contact guidance was coined to describe the phenomenon in which cells align to and migrate along linear patterns or structures, such as microfabricated lines, microcontact printed lines of proteins, and aligned fibrillar structures.

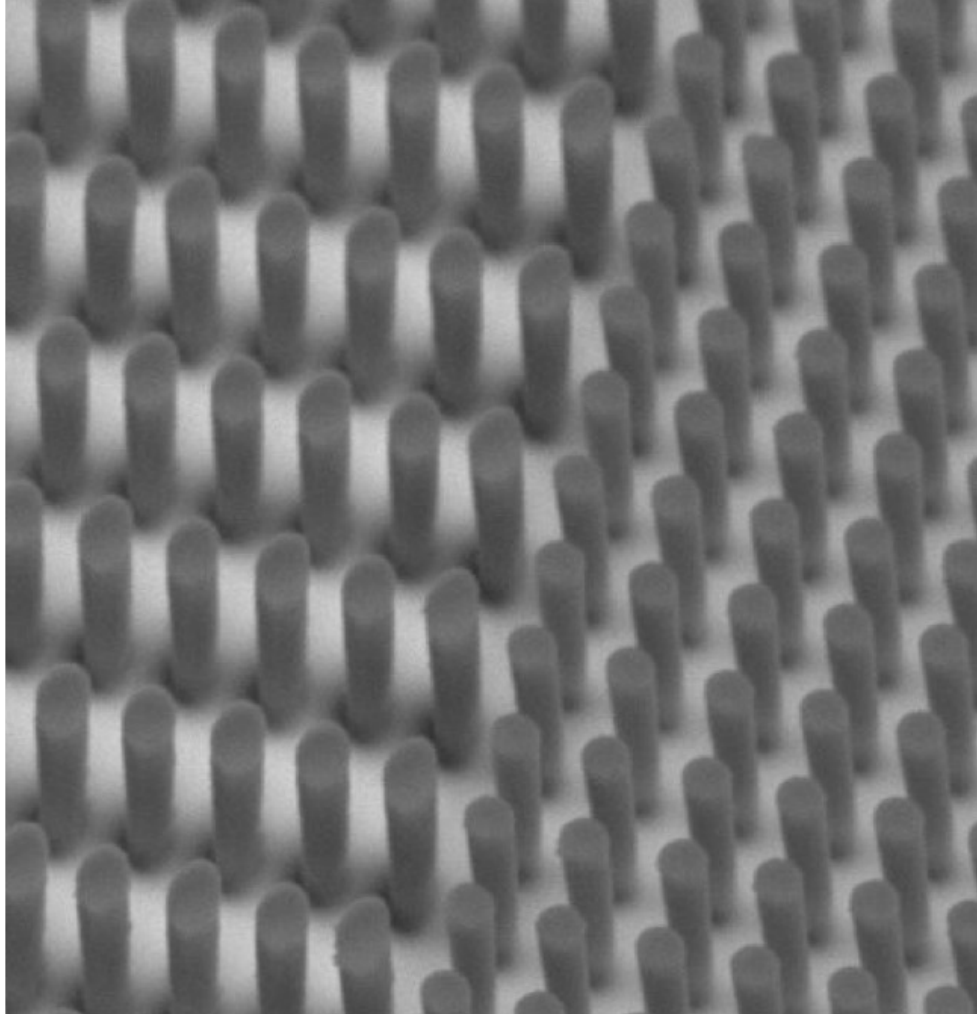


Figure 2: SEM image of oval and circular cross-section micropillars

Scanning electron microscope image of oval and circular cross-section micropillars. Pillars were created using standard photolithography techniques. SU-8 photoresist was spun to a height of 6 μm on a silicon wafer. UV exposure through a mask and removal of non-crosslinked photoresist results in rigid micropillars. Oval micropillars measure 4.5 μm (major axis) x 2.5 μm (minor axis) x 6 μm and are spaced apart 5 μm (minor axis) and 10 μm (major axis). Circular micropillars measure 2.6 μm x 6 μm and are spaced 5 μm apart.

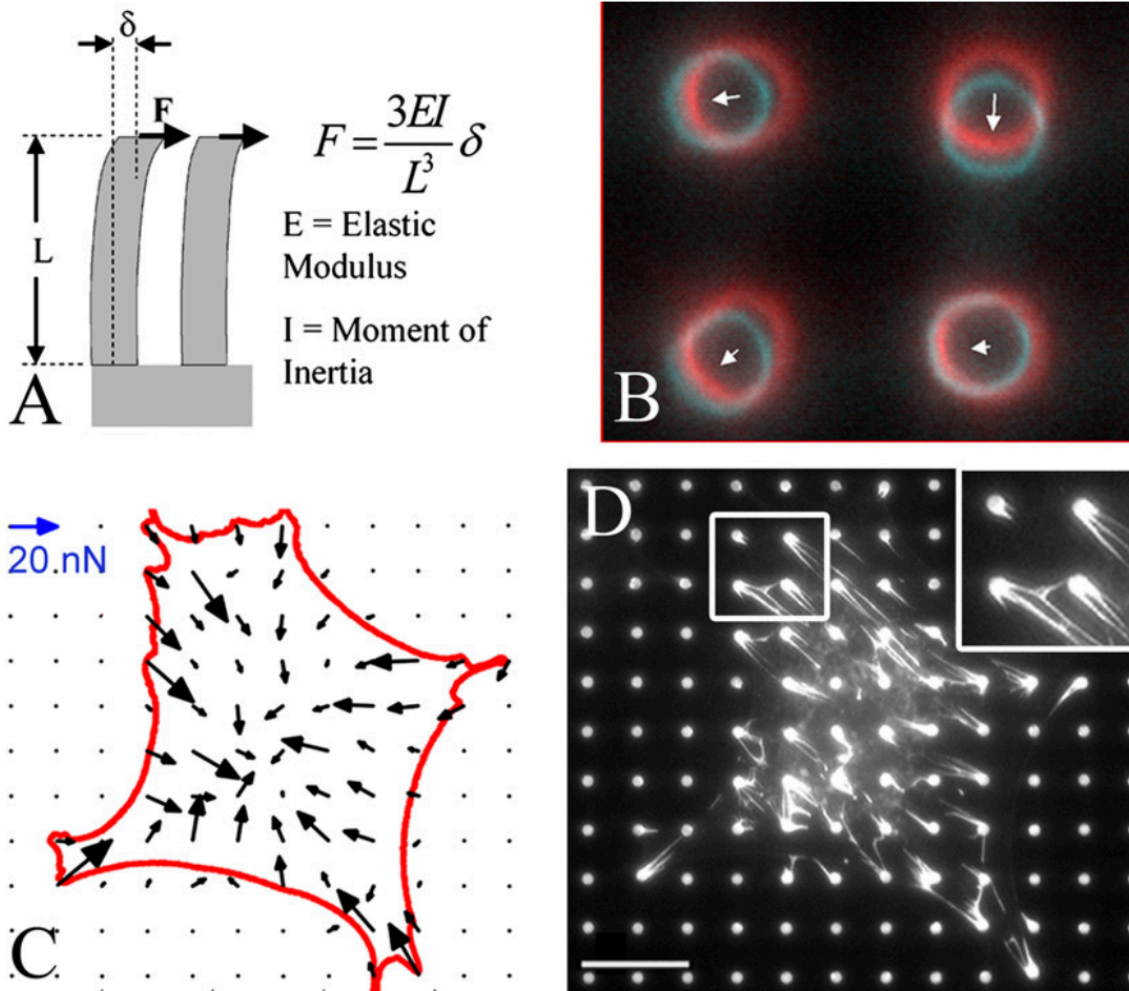


Figure 3: Calculating forces from micropillar arrays

A) Beam bending equation utilized to calculate force from measured deflections. Micropillars are $3 \mu\text{m} \times 10 \mu\text{m}$ with a spacing of $9 \mu\text{m}$. B) Fluorescent images at the top (blue) and bottom (red) of micropillars showing the measured deflections. C) Map of force vectors under a single cell. Net force shown at top left. D) Fibronectin fibrils assembled on the tops of micropillars. Reproduced with permission from Lemmon et al.⁴³

2.7 Innovations

2.7.1 Innovation #1: Microfabricated pillar arrays with anisotropic stiffness:

Oval micropillars present a unique opportunity to influence cells with both anisotropic stiffness and aligned contact guidance cues. Previous studies have utilized methods such as polyacrylamide gels with varying stiffness, microfabricated lines, aligned collagen scaffolds, and aligned electrospun scaffolds. None of these methods can match the accuracy, repeatability, and most importantly, the adaptability of oval micropillars. We can easily change the aspect ratio of oval micropillars to increase or decrease the effect of aligned topography/contact guidance, and we can easily modulate substrate stiffness by altering the height or the cross-sectional area of the micropillars. Due to the multitude of options in stiffness and oval aspect ratio, oval micropillars are one of the most versatile methods to mimic the mechanical signals present in anisotropic tissues.

2.7.2 Innovation #2: A multi-cue microfluidic device that mimics TACS mechanics:

Mimicking more than one stimulus in cell-based assays has always been a challenge. Many have studied the effects of biochemical and biomechanical cues individually, but few have studied them concomitantly. Generally, when discussing external stimuli that influence cell behavior, we think of cytokine concentration and gradients as well as changes in the mechanical properties of ECM. The difficulty lies in the ability to present multiple stimuli in a precise manner within a single assay. We have accomplished just this in developing an assay that will allow us to consistently control mechanical properties while also generating a chemotactic gradient. Using combinations of circular and oval micropillars, we recreated the various arrangements of collagen present in TACS 1-3. Circular micropillars were used to mimic isotropic collagen in TACS 1. Circumferentially aligned ovals were used to mimic TACS 2, and finally, radially aligned ovals were used to mimic TACS 3. We developed a novel microfluidic assay which allowed us to

generate a chemotactic gradient across the migration area of each of the aforementioned designs. To our knowledge, this is the first assay to mimic anisotropic mechanical stimuli and chemotactic gradients, which promote malignant cell invasion, present in the developing tumor microenvironment. Our novel design allowed us to further elucidate the roles of mechanical and chemical signaling in malignant cell invasion and will serve as a novel platform for testing of new strategies and therapies against metastasis.

In this dissertation, we expand on the works described above by developing an *in vitro* assay to simulate anisotropic stiffness. In Chapter 3 we describe the development and validation of arrays of microfabricated pillars with either circular cross-section, which exhibit isotropic stiffness, or oval cross-section, which exhibit anisotropic stiffness. We then use these substrates to probe fibroblast morphology, ECM assembly, traction force, and alignment in response to anisotropic stiffness and aligned topography. We use NIH-3T3 fibroblasts and adipose derived mesenchymal stem cells (ASCs) to demonstrate the efficacy of our design. In Chapter 4, we use our validated platform to probe the effects of anisotropic mechanical properties on healthy (MCF10A), premalignant (MCF10AT1), and metastatic (MDA-MB-231) breast epithelial cell lines. These cell lines were selected as representatives of various stages of tumor development. Finally, in Chapter 5 we develop a microfluidic device, utilizing our previously developed anisotropic substrate, to mimic the ECM mechanics at all three TACS stages. We integrate our oval micropillars into a microfluidic device to recapitulate the chemotactic gradients present in the tumor microenvironment. We demonstrate that both anisotropic stiffness and contact guidance cues play significant roles in mediating malignant cell invasion into surrounding healthy tissue, thereby facilitating metastasis.

Chapter 3

A novel multi-stiffness platform

3.1 Rationale

Previous works have demonstrated the effect of substrate stiffness on cell size, traction forces, and migratory capability. Some examples of substrates used in these works are collagen gels, polyacrylamide gels, and polydimethylsiloxane (PDMS). Generally, researchers vary the bulk material properties of these substrates, such as the elastic modulus. While these are effective resources to modulate stiffness, they unfortunately lack the ability to precisely mimic anisotropic ECM architectures present in tissues, such as vasculature, muscle, tendons and even tumors. To meet this need, we developed a substrate utilizing oval micropillars which mimics two important mechanical cues present natively in anisotropic tissues. Oval micropillars exhibit 1) anisotropic stiffness (stiffer in the major axis vs minor) and 2) an elongated shape to imitate contact guidance

cues provided by aligned ECM fibers. Our novel substrate contains regions of both circular cross section micropillars (isotropic stiffness) and oval micropillars (anisotropic stiffness) on a single sample, allowing us to compare the effects of varying substrate mechanical properties across the same cell population to minimize any variance. Due to the complex nature of micropillar array preparation, there are many instances in which error can be introduced, namely: varying age of cells, accurate PDMS blend formulation, quality of microcontact printing of FN onto micropillars, and variance in cell lifting, counting, and seeding protocols. By combining two micropillar designs into one sample, we also increased experimental efficiency by halving the number of samples that need to be prepared and imaged.

We began by using fibroblast cell lines to validate that our design was indeed able to influence cell behaviors, such as morphology, force, FN assembly, and alignment. Fibroblast cell lines were chosen to act as a proof of concept for our novel substrate due to our long-held understanding that they are capable of generating large traction forces and are highly mechanoresponsive (that is, they are highly responsive to changes in mechanical properties, such as stiffness and ECM architecture). Many previous studies have demonstrated that cells generate higher traction forces, assemble more ECM, and are even more likely to differentiate down an osteogenic lineage on substrates of greater stiffness^{19,42,44,45}. Lemmon et al. seeded NIH-3T3s on micropillar arrays of various stiffness and demonstrated the correlation between substrate stiffness and increased cell force and ECM assembly⁴². Many studies have also demonstrated that cells align and migrate in response to linear contact guidance cues (microcontact printed lines, microfabricated lines, aligned fiber scaffolds) and migrate up stiffness gradients^{12,38,46}. Based on this prior knowledge of the highly mechanoresponsive nature of fibroblast cell lines, we chose to use NIH-3T3s, mouse embryonic fibroblasts, and ASCs, adipose derived mesenchymal stem cells,

to demonstrate that our substrate was indeed able to modulate cell morphology, force, alignment, and ECM assembly. Once we were able to demonstrate that our substrate elicited the desired cellular response, we wanted to further clarify the mechanism that facilitates this response.

We chose to test how mitigating the cell's ability to generate force influences mechanoresponse. Previous works have proven the existence of various methods of mechanotransduction. Integrins and cadherins transfer mechanical signals to focal adhesions or cell-cell adhesion complexes, which can trigger a number of downstream responses⁴⁷. These and other methods that convert mechanical signals into intracellular signals, such as mechanosensitive ion channels, demonstrate that cells use force to transmit mechanical signals to mechanoreceptors, which in turn induce changes in cell behavior^{48,49}. Many works have also demonstrated the effects of downregulating force on cell migration, alignment, and ECM assembly^{43,49}. We chose to use two well characterized inhibitors, Y-27632 and blebbistatin, to downregulate force and ultimately disrupt mechanosensing. We demonstrate that by limiting force, thereby decreasing signaling to the mechanoreceptors, we can downregulate responses such as cell spreading, ECM assembly, and alignment.

We bring this chapter to a conclusion by investigating the other extreme, wherein we upregulate the cells' ability to generate force through the use of inflammatory cytokines, and observe the change in mechanoresponse. In disease scenarios such as scar formation, fibrosis, and tumor development, inflammatory cytokines released by resident cells induce fibroblast activation. Activation potentiates fibroblast transformation into myofibroblasts, which go into overdrive to repair damaged tissue and are identified by the following characteristics: increased motility, larger traction forces, and increased ability to assemble new ECM. Many works point towards increased regional tissue stiffness as the initiating factor of dysregulated tissue repair. Increased stiffness

starts a positive feedback loop which leads to increased inflammatory cytokine expression, fibroblast activation, ECM assembly and further increased tissue stiffness. We chose to use the tumor microenvironment as a model of this process to determine exactly how inflammatory cytokines and increased stiffness influence fibroblast behavior. The tumor microenvironment (TME) has high concentrations of many inflammatory signaling molecules; one of the best characterized is transforming growth factor – beta 1 (TGF- β 1). TGF- β 1 participates in progressing tumor formation by activating fibroblasts to reorganize the ECM and inducing epithelial-mesenchymal transition (EMT) in healthy epithelial cells. Previous works have demonstrated that stimulation of human mesenchymal stem cells (HMSCs) with TGF- β 1 causes activation into a myofibroblast-like phenotype. Once activated, they express α -Smooth Muscle Actin (α -SMA) and display an increased capacity to assemble ECM^{50,51}. TGF- β 1 stimulation of NIH-3T3s leads to an increased expression of α -SMA and secretion of procollagen (the precursor to collagen)⁵². This enables them to assemble more collagen, leading to a stiffer ECM, and initiating the positive feedback loop described earlier. Using conditioned media from metastatic cells (MDA-MB-231s), which contain high levels of TGF- β 1 and many other important inflammatory cytokines, we investigated the relationship between activation and traction forces, cell size, ECM assembly, and alignment.

3.2 Methods

3.2.1 Fabrication of Oval Substrates, Circle Substrates, and Half-and-half substrates

Substrate designs were generated in the program CleWin. Standard photolithography processes were used to create micropillars. We utilized a Heidelberg Instruments uPG 101 to expose our pattern into a glass low reflective chrome mask. Subsequently, we developed the exposed photoresist on the mask and used chrome etchant to remove chrome from exposed areas. This yielded a mask with a cross sectional pattern of the final desired structures. Negative photoresists, such as SU-8, crosslink and form rigid structures when exposed to UV light. Considering this, our mask had transparent circular and oval areas allowing UV light to pass. Next, we spun coat wafers with SU-8 2010, using various RPMs to achieve various heights, and then exposed them using a Karl Suss MJB4 Mask Aligner. Wafers were developed using Kayaku Advanced Materials SU-8 Developer, which removed any non-crosslinked photoresist. The wafer was then submerged in hexane and pentane for 5 minutes each to wash out the SU-8 Developer and reduce the surface tension in a step wise manner. Due to the extremely low surface tension of pentane, we were able to prevent the pillars from collapsing during drying. Next, the wafer was heat treated on a hot plate at 200° C for 30 minutes to strengthen the structures, followed by treatment via vapor deposition with Trichloro(1*H*,1*H*,2*H*,2*H*-perfluorooctyl)silane (Sigma-Aldrich) to minimize surface adhesion. Polydimethylsiloxane (PDMS) was mixed at a 1:10 (crosslinker : base) ratio and poured over the wafer to create a mold with wells (inverse of the pillars). We molded from this one more time to finally create PDMS micropillars on a glass coverslip.

3.2.2 Microfabricated Pillar Array preparation

Micropillars were functionalized with fibronectin (FN) (Sigma-Aldrich Fibronectin from human plasma F0895) using the following process: Flat PDMS (30:1 blend) “stamps”, of about 1cm², were coated with 100μL of 200ng/mL FN and allowed to incubate at room temperature for 1hr. Coverslips were then exposed to UV (Novascan PSD pro series digital UV ozone system) for 10min to activate the top surfaces of the pillars to facilitate protein transfer. Excess FN was removed from stamps by gently submerging in DI water and drying with sterile nitrogen gas. Stamps were then inverted and placed in contact with the micropillar tops to transfer FN. Next, the coverslips were placed in fluids of gradually increasing surface tension (100% EtOH, 70% EtOH, and finally PBS 3 times) to avoid collapsing the micropillars. After these washes, the coverslips were submerged in a solution of 10% fluorescent Bovine Serum Albumin (BSA) in PBS (weight : volume, 5 grams BSA into 50mL PBS) for 1 hour. BSA fluorescently labels all surfaces of the micropillars which are not coated with FN. Coverslips were again washed with PBS 3 times and placed in 1% F-127 for 1 hour to prevent cell adhesion outside of FN-coated surfaces.

3.2.3 Cell culture

We chose to validate our novel substrate using well characterized fibroblast cell lines. It is known that epithelial cells themselves cannot easily degrade or reorganize the ECM. Tumor formation relies on epithelial cells that have undergone epithelial to mesenchymal transition or fibroblasts in the surrounding tissues. Resident fibroblasts and stem cells are transformed into myofibroblasts by inflammatory chemokines present in the TME, such as TGF-β1, and are collectively referred

to as cancer associated fibroblasts (CAF). CAFs are primarily responsible for ECM reorganization across all stages of tumor growth tumor growth. Since CAFs are, in fact, activated resident fibroblasts, we choose the following common fibroblast lines to validate the effects of our substrate.

NIH-3T3 and ASC cell lines were used to validate cell response to anisotropic mechanical cues (oval micropillars). NIH-3T3 cells are immortalized embryonic fibroblasts originally derived from swiss albino mouse embryonic tissue. NIH-3T3 cells display fibroblast morphology (spindle like), assemble ECM extremely well, and are highly motile. They have been used in a wide array of *in-vitro* assays and are regarded as a standard across fibroblast lines. ASCs are stem cells, derived from adipose tissues that display fibroblast-like morphology, assemble large quantities of ECM and generate large traction forces. ASCs are capable of being differentiated into adipogenic, chondrogenic, and osteogenic lineages.

Many works have demonstrated that these cell lines are highly responsive to changes in substrate stiffness as well as contact guidance cues, and that they generate relatively large traction forces. Due to these characteristics, these cell lines are the ideal choice to demonstrate that the varied stiffness and geometry between circular and oval micropillar arrays can mechanically modulate cell behavior.

3.2.4 Cell Culture

Cells were plated on fibronectin-coated micropillars at a density of 5,000 cells per sample in 2mL of media, which contain approximately 1cm² of micropillars, and allowed to incubate for 24 hours at 37°C and 5% CO₂. Cells were permeabilized using 0.5% Triton-X-100 in 4% paraformaldehyde for 2 minutes and fixed in 4% paraformaldehyde for 20 minutes. Next, samples

were rinsed with PBS 3 times and placed in a 0.1% BSA blocking solution for 5 minutes. Following the blocking step, 50-100 μ L of our primary antibody was placed on a sheet of parafilm in a 100mm petri dish. The 25mm coverslip was then flipped over and placed cell side down on top of the primary antibody droplet and incubated at 37°C for 30 minutes. After being submerged in 0.1% BSA for another five minutes, the previous step was repeated to apply the secondary antibody. The samples were immunofluorescence stained for FN (Abcam rabbit anti FN ab2413), actin (Alexa Fluor 555 Phalloidin A34055), and the nucleus (NucBlue Fixed ReadyProbes R37606). Coverslips were mounted using Fluoromount G (Invitrogen 00-4958-02) and allowed to dry at room temperature overnight in a dark environment. Samples were imaged on a Zeiss Axio Observer fluorescence microscope. Images were analyzed using an original MATLAB code written by Dr. Christopher Lemmon. Through analysis we quantified cell size, eccentricity, cell alignment, traction forces and ECM assembly.

3.2.5 MDA-MB-231 conditioned media (231CM) production and treatment

MDA-MB-231 cells were cultured in the standard media for the effector cell line in a T25 tissue culture flask from 50% confluence for 48 hours, during which they reached approximately 90-100% confluence. At 48 hours, the media was removed from the MDA-MB-231 flasks, centrifuged at 10,000 RPM for 10 minutes to remove any floating cellular debris. The media was next frozen in 1.3 mL aliquots for at least 24 hours to neutralize any remaining cells or bacteria. NIH-3T3s and ASCs were seeded on prepared micropillar substrates as stated above except only in 1mL media rather than 2 mL. 1mL 231CM was warmed and added to the seeding media at 90 minutes post seeding to create a final volume of 2 mL. Cells were allowed to culture on micropillar substrates for 24 hours before fixing and staining. Samples were immunofluorescence stained for

FN (Abcam rabbit anti FN ab2413), actin (Alexa Fluor 555 Phalloidin A34055) and the nucleus (NucBlue Fixed ReadyProbes R37606).

3.2.6 Y-27632 and Blebbistatin Treatment

A ROCK inhibitor (Y-27632 dihydrochloride, Sigma-Aldrich Y0503-1MG) and a myosin inhibitor (Blebbistatin, Sigma-Aldrich B0560-1MG) were used to downregulate force production. Y-27632 is a highly selective inhibitor of Rho-associated coiled-coil containing kinases (ROCK). One primary role of ROCK is its regulation of actin cytoskeletal organization. ROCK also has the capacity to phosphorylate myosin II regulatory light chains, which enable actomyosin contractility⁵³. Thus, inhibition of ROCK signaling limits a cell's ability to generate traction forces. Blebbistatin is a selective inhibitor of myosin II activation. It binds to the myosin head when detached from actin filaments and prevents its ability to bind again⁵⁴. This limits a cell's ability to generate forces by downregulating actomyosin contractility. Samples in these treatment conditions were seeded and allowed to attach to the micropillars for 90 minutes before being treated with either 20 μ M Y-27632 or 20 μ M Blebbistatin. Cells were incubated for 24hrs before analysis. Samples were fixed, stained, and analyzed as described above.

3.2.7 Statistical analysis

The analyzed data output from the original MATLAB analysis code authored by Dr. Christopher Lemmon was transferred into GraphPad Prism statistical analysis software. Statistically different significances were determined by a One-way ANOVA followed by a Student's t-test. Three samples per condition were analyzed with total cell counts as follows: 3T3s on circular micropillars; control n = 60, Y-27632 n = 60, blebbistatin n = 54, 231CM n = 60. 3T3s on oval micropillars; control n = 60, Y-27632 n = 60, blebbistatin n = 60, 231CM n = 60. ASCs

on circular micropillars; control n = 59, Y-27632 n = 59, blebbistatin n = 60, 231CM n = 60. ASCs

on oval micropillars; control n = 60, Y-27632 n = 60, blebbistatin n = 60, 231CM n = 60.

3.3 Results

NIH-3T3 Data

3.3.1 NIH-3T3 Immunofluorescence analysis:

We began by investigating how cells' ability to generate and exert forces onto their surroundings affects their morphology and ability to assemble ECM. Initially, we visually assessed NIH-3T3s that were cultured on isotropic (circular cross section) micropillars for 24 hours. We exposed 3T3s to Y-27632 and blebbistatin, treatments which have been extensively proven to downregulate a cell's ability to generate force. To upregulate cell force production, we utilized media that was conditioned with MDA-MB-231s (231s). 231s are a metastatic cell line known to express many inflammatory factors into the media that stimulate cells to produce greater forces and assemble more ECM^{17,18}. In Figure 4, we assembled representative images of 3T3s on circular cross section micropillars across the following treatment conditions: control, Y-27632, blebbistatin, and 231CM. Comparing the images in the actin column, we are able to note some distinct differences in morphology between the treatment conditions. Cells treated with Y-27632 displayed a more elongated phenotype than normal 3T3s. When treated with blebbistatin, cells showed distinctly smaller cell bodies and multiple long, thin filopodial protrusions. In contrast, cells treated with 231CM displayed increased actin stress fibers, depicted by thicker and more dense fibers in the cytoskeleton. Next, we assessed FN assembly potential across our conditions. 3T3s in the control conditions assembled a moderate level of FN. When force was downregulated using Y-27632 and blebbistatin, we noticed a decrease in fibrils, but an increase in intracellular or perinuclear FN staining, indicating that cells are still expressing FN, but are unable to assemble it

into fibrils on the surface of the substrate. When force was upregulated using 231CM, we noted a decrease in intracellular staining but highly increased FN fibril assembly on micropillar tops.

Next, we chose to assess how seeding cells on an anisotropic stiffness substrate affected morphology and ECM assembly. Oval micropillars are overall much stiffer than circular cross section micropillars and also expose cells to anisotropic stiffness by way of being stiffer in the major axis versus the minor axis. Substrate stiffness has been demonstrated to stimulate higher traction forces and greater ECM assembly in many cell lines. Generally, cells on oval micropillars showed a slightly more aligned morphology to the major axis of the oval micropillars. As seen in Figure 5, cells displayed similar morphological changes across the treatment conditions, which were observed on circular micropillars, such as long filopodial protrusions when treated with blebbistatin and increased actin stress fibers when treated with 231CM. FN expression and assembly also varied in a manner similar to their behavior on circular micropillars. Cells treated with Y-27632 exhibited increased intracellular FN staining and decreased fibril assembly. Blebbistatin-treated cells displayed decreased FN assembly and decreased intracellular staining, and cells in the 231CM group displayed a marked increase in FN fibril assembly. After assessing the images visually, we ran them through an original MATLAB analysis code, written by Dr. Christopher Lemmon, to quantify changes in cell area, FN expression and assembly, traction force, and alignment characteristics.

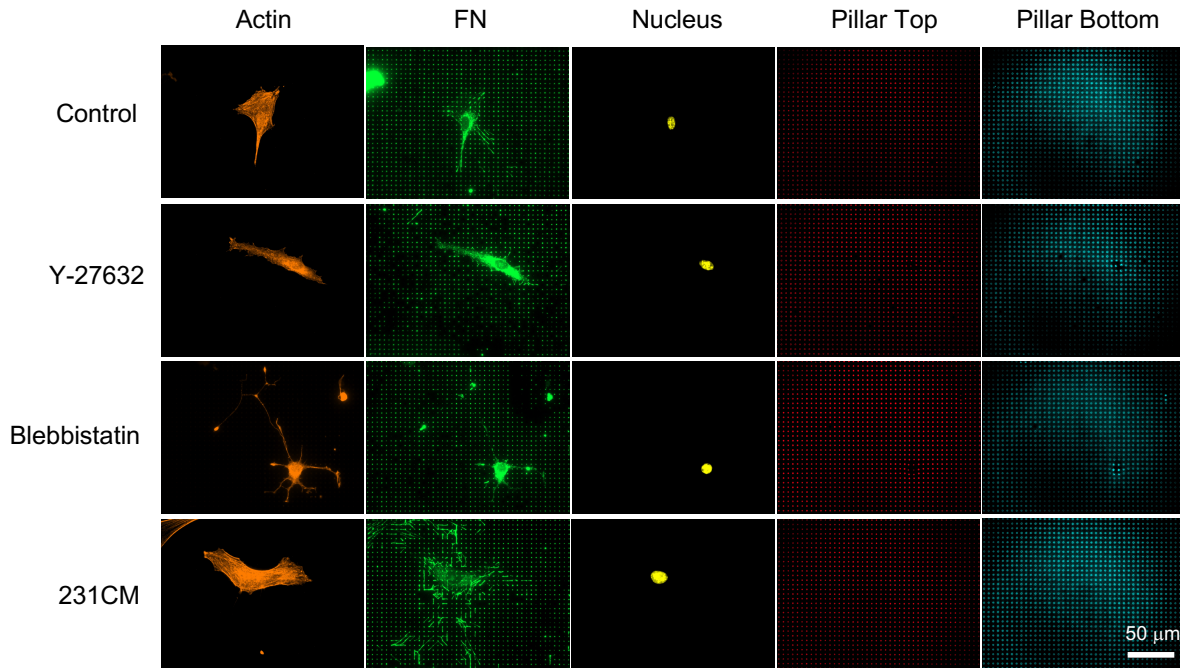


Figure 4: NIH-3T3s on circular micropillars

Representative images of NIH-3T3 cells seeded on circular cross section (isotropic) micropillars for 24 hours. Cells were stained for actin (orange), fibronectin (green), nucleus (yellow), micropillar tops (red), and micropillar bottoms (blue). Cells were treated with either 20 μ M Y-27632, 20 μ M blebbistatin, or MDA-MB-231 conditioned media 90 minutes after seeding. Compared to the control condition, cell treated with Y-27632 displayed no significant changes in morphology (actin) and greater intracellular staining for FN rather than assembled fibrils. Blebbistatin-treated cells displayed smaller cell bodies with multiple thin elongated filopodia. They also displayed decreased FN fibril assembly. Cells treated with MDA-MB-231 conditioned media displayed slightly larger cell bodies and increased actin stress fibers in the cytoskeleton. 231CM-treated cells exhibited decreased intracellular FN and greatly increased FN fibril assembly on micropillar tops. All images were taken on a Zeiss Axio Observer microscope using a 63x magnification oil objective. Scale bar represents 50 μ M.

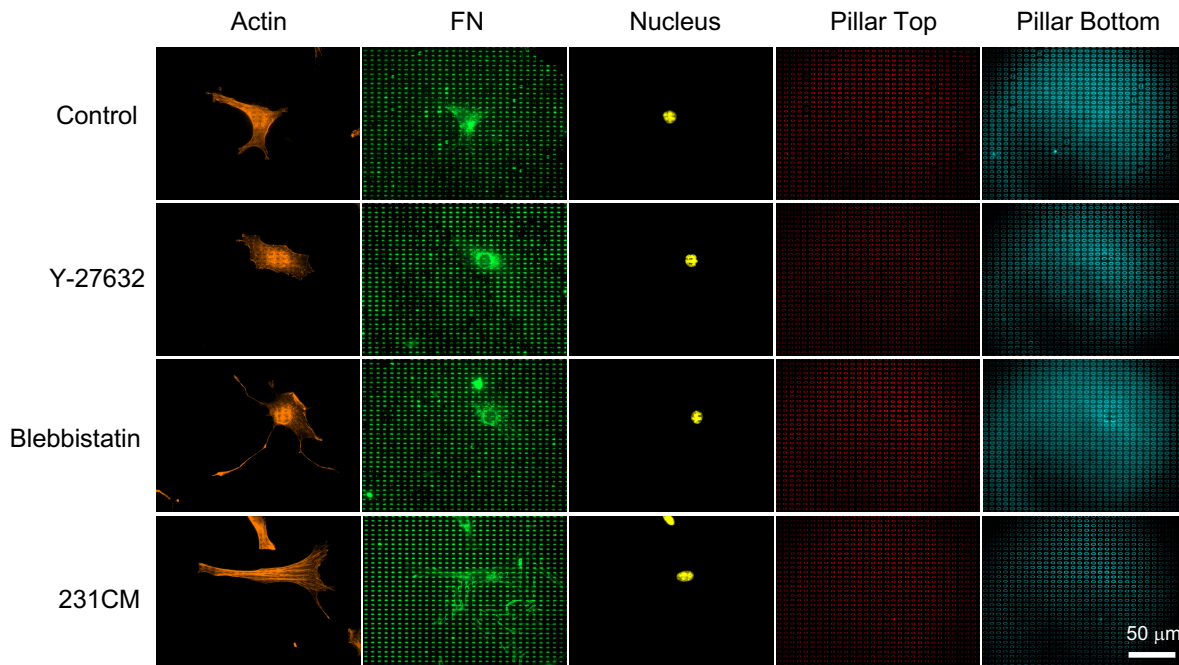


Figure 5: NIH-3T3s on oval micropillars

Representative images of NIH-3T3 cells seeded on oval cross section (anisotropic) micropillars for 24 hours. Cells were stained for actin (orange), fibronectin (green), nucleus (yellow), micropillar tops (red), and micropillar bottoms (blue). Cells were treated with either 20 μ M Y-27632, 20 μ M blebbistatin, or MDA-MB-231 conditioned media 90 minutes after seeding. When compared to the control condition, cells treated with Y-27632 displayed no significant changes in morphology (actin), but as expected, showed increased intracellular staining for FN rather than assembled fibrils. Similar to their counterparts on circular micropillars, blebbistatin-treated cells displayed smaller cell bodies with multiple thin elongated filopodia, as well as decreased intracellular FN and assembled FN fibrils. Cells treated with MDA-MB-231 conditioned media displayed slightly larger cell bodies and increased actin stress fibers in the cytoskeleton. 231CM treated cells exhibited decreased intracellular FN and greatly increased FN fibril assembly on micropillar tops. All images were taken on a Zeiss Axio Observer microscope using a 63x magnification oil objective. Scale bar represents 50 μ M.

3.3.2 3T3 MATLAB analysis of cell area, fibril area, and force:

Immunofluorescence images of NIH-3T3s were analyzed in MATLAB. Quantification of cell area revealed that none of the treatments (Y-27632, blebbistatin, or 231CM) led to any significant increases or decreases in overall cell area when compared within their micropillar groups (Figure 6 A & B). However, when comparing between circular and oval micropillar groups, cells demonstrated a significant increase in cell area on oval micropillars across all treatment conditions (Figure 6C).

Next, we quantified FN expression and assembly. On circular micropillars (Figure 7A), treatment with Y-27632 failed to significantly decrease FN area, and 231CM treatment failed to increase FN area. Treatment with blebbistatin led to a significant decrease in FN area relative to Y-27632 and 231CM conditions, but not against the control. On oval micropillars, treatment with blebbistatin decreased FN area significantly compared to all other groups (Figure 7B). When comparing between circular and oval micropillars (Figure 7C), we can clearly see that cells on oval micropillars express and assemble less FN across all treatment conditions.

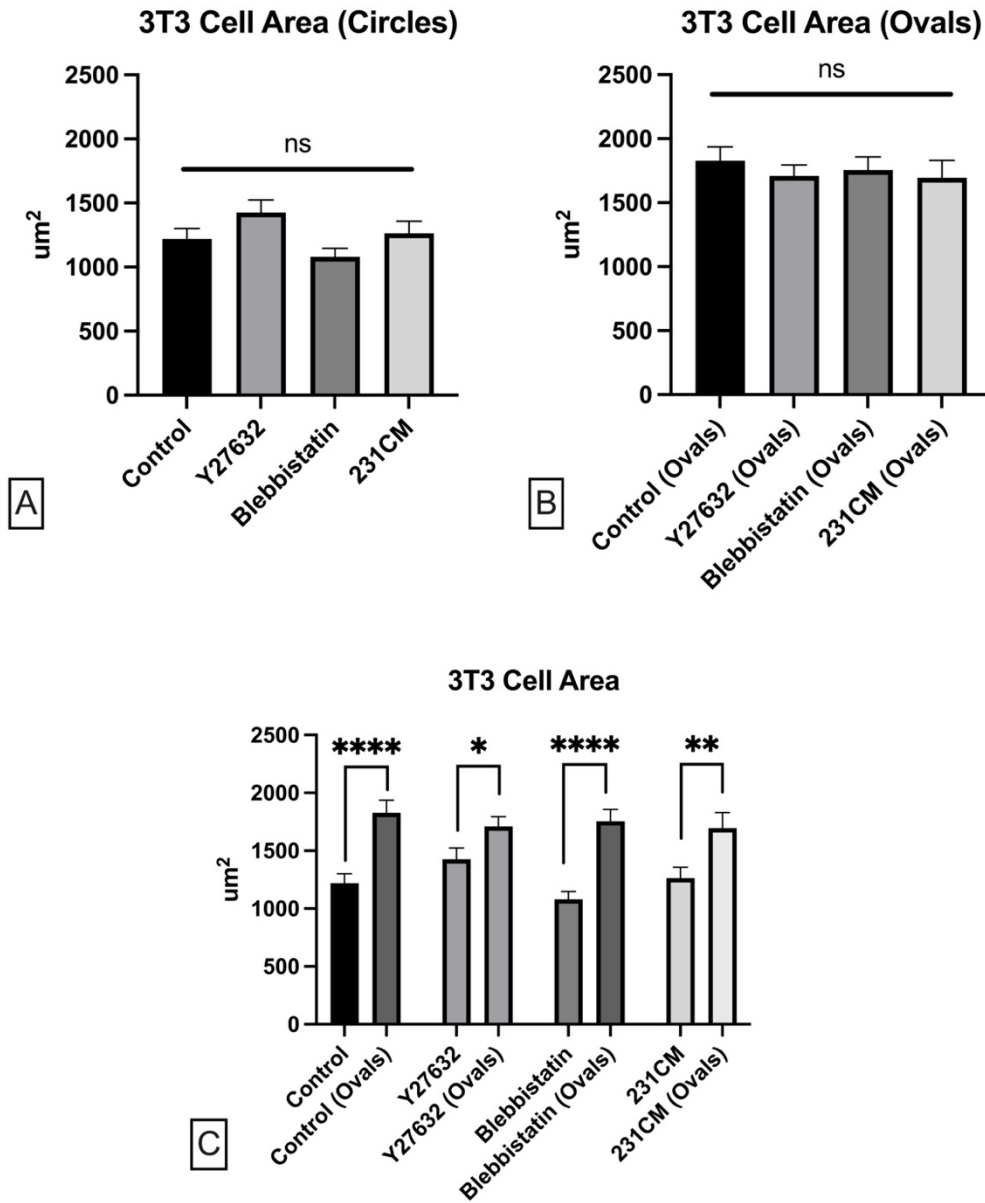


Figure 6: 3T3 cell area

3T3 cell area quantified on both circular and oval cross section micropillars across control, Y-27632, blebbistatin, and 231CM conditions. A) 3T3s on circular cross section micropillars show no significant difference in cell area across all treatment conditions. B) 3T3s on oval cross section micropillars show no significant difference in cell area across all treatment conditions. C) 3T3s

spread to a significantly larger size on oval micropillars when compared to those exposed to the same treatment on circular micropillars. While cell areas were significantly different between circular and oval micropillar substrates, treatment with Y-27632 or blebbistatin did not decrease cell area significantly and treatment with 231CM did not induce greater cell spreading compared to controls, contrary to our initial hypothesis.

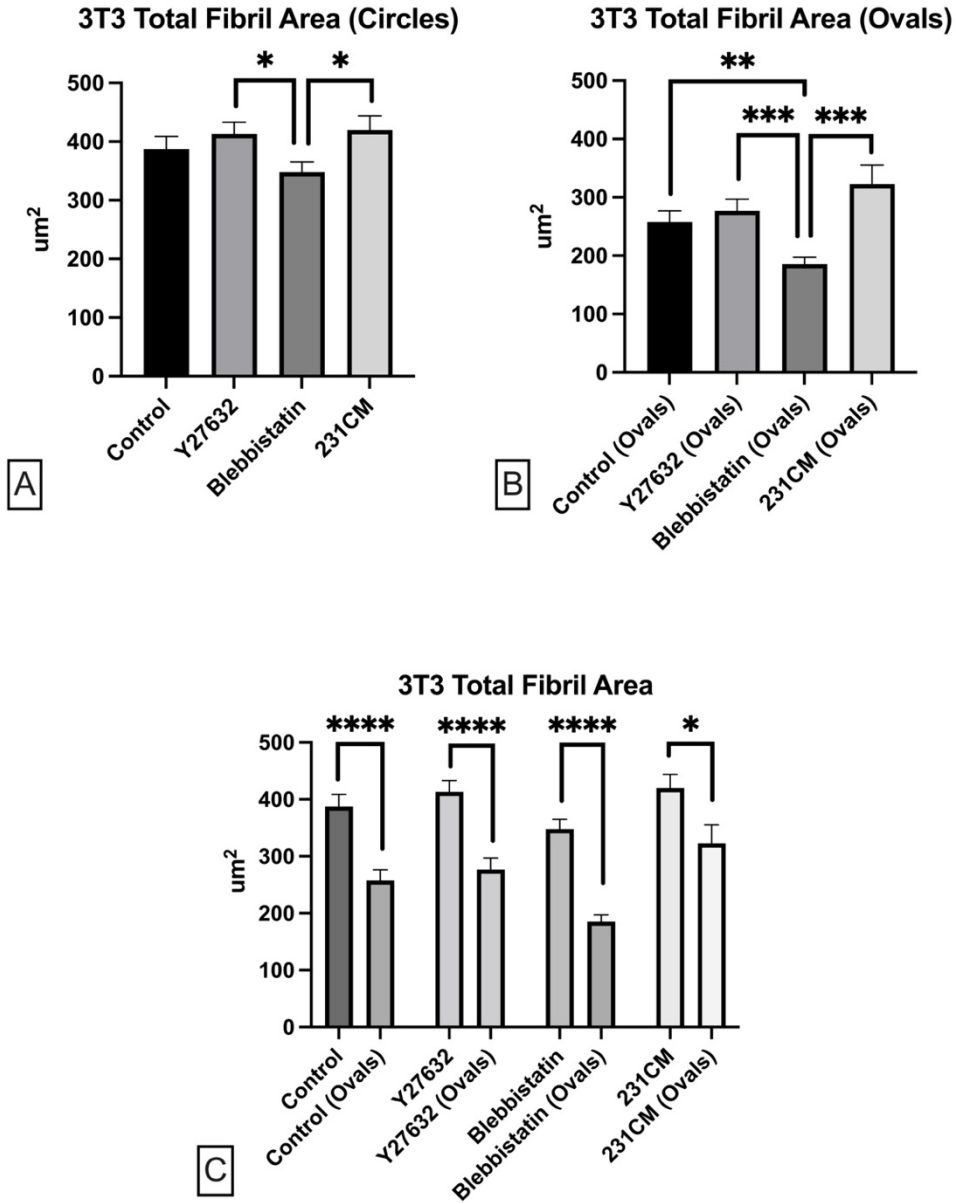


Figure 7: 3T3 total fibril area

3T3 total fibronectin fibril area on both circular and oval cross section micropillars. Cells on both areas of the substrate were analyzed across control, Y-27632, Blebbistatin, and 231CM treatment conditions. A) Cells treated with Y-27632 and 231CM failed to show a significant decrease or increase, relatively, when compared to the control. Cells treated with blebbistatin displayed significantly less assembled FN fibrils when compared to Y-27632 and 231CM conditions. B) On

oval micropillars, cells treated with blebbistatin assembled significantly less FN than all other conditions. C) Cells in all treatment groups assembled significantly less FN on oval micropillars than on circular micropillars.

Analysis of cell forces on circular micropillars revealed that treatment with blebbistatin and 231CM led to a significant increase in total force (Figure 8A), and that these differences are maintained when the force is normalized by the number of occupied micropillars (Figure 8B) and cell area (Figure 8C). The increase in cell force in the blebbistatin was unexpected, as all previous studies have reported that it causes a decrease in cell force. To elucidate this finding, we looked back at our immunofluorescence images and noticed something curious. Cells in the Y-27632 and blebbistatin conditions were exhibiting large micropillar deflections under their nuclei (Figure 9). We theorize that limiting cell force prevents cells from stretching themselves taut across the tops of the micropillars, and this allows the nucleus to sag between the pillars deflecting them. On oval micropillars, the data show a similar increase in total force and force per cell area in the blebbistatin treatment group.

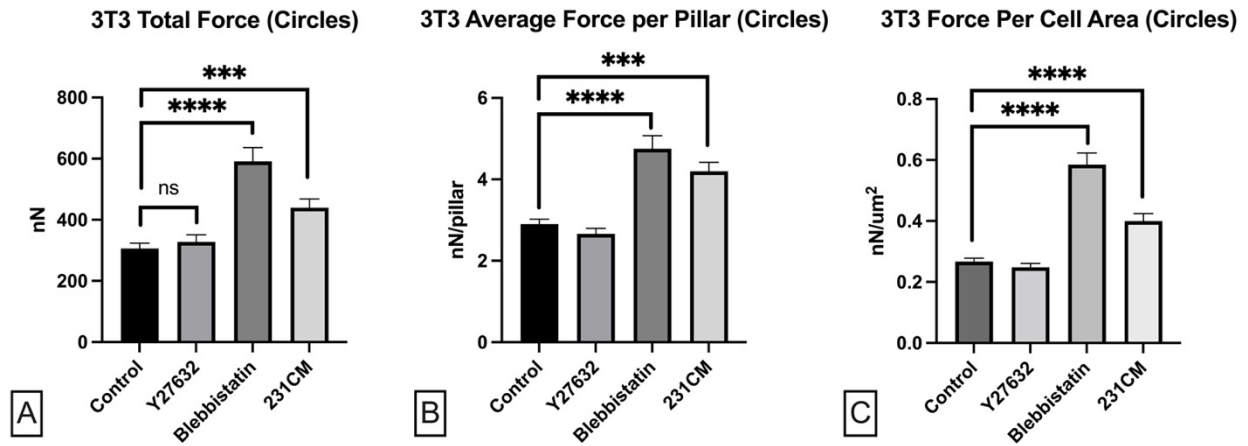


Figure 8: 3T3 cell forces on circular micropillars

Force analysis of NIH-3T3s on circular micropillars. A) On circular micropillars, 3T3s treated with blebbistatin and 231CM generated significantly higher forces when compared to the control condition. B) Total force normalized against the number of pillars yielded the same results. Cells in the blebbistatin and 231CM groups displayed significantly higher forces when compared to the control. C) When normalized by cell area, 3T3s once again display higher forces in the blebbistatin and 231CM conditions.

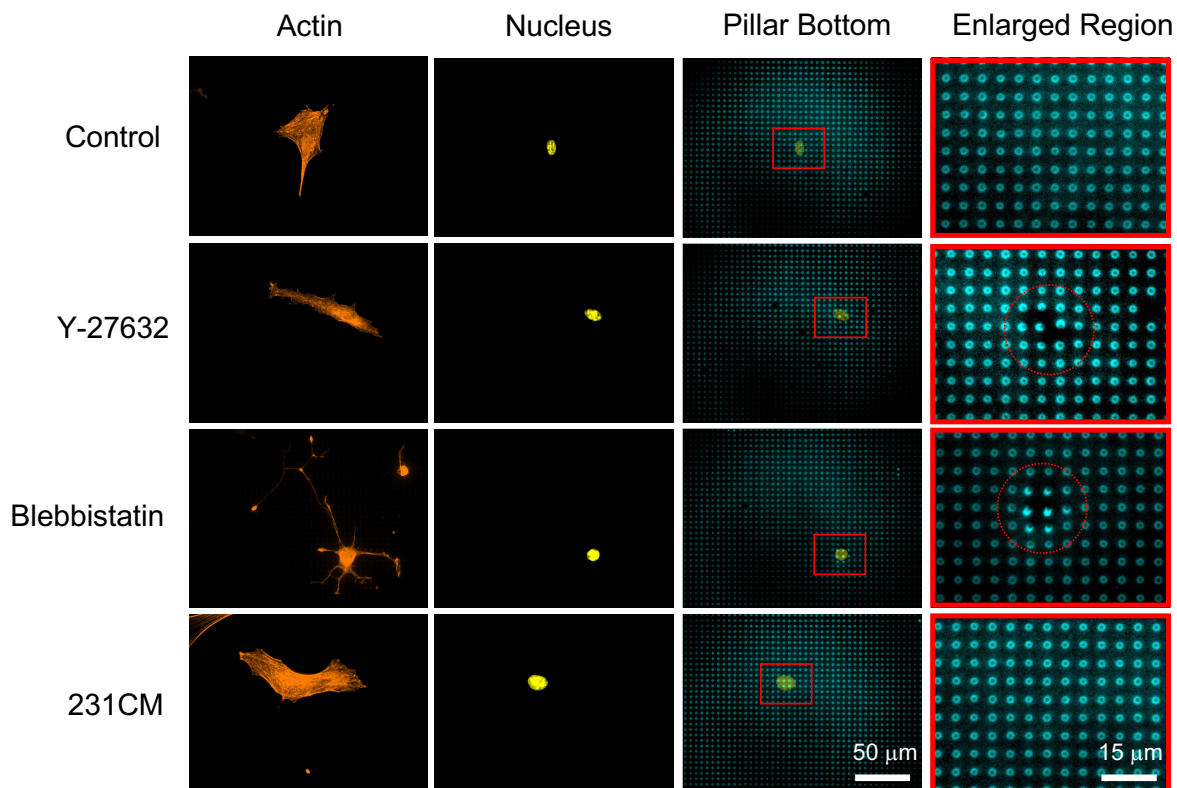


Figure 9: Nuclear micropillar deflections of circular micropillars

Referencing the same cells displayed above in Figure 4, enlarged regions of the micropillars under cell nuclei are presented in the last column. In the enlarged regions, areas directly under the nuclei in the Y-27632 and blebbistatin conditions are identified within the red dotted circle. We can clearly visualize large micropillar deflections directly under the cell nuclei in both Y-27632 and blebbistatin treatment conditions, while no deflections can be visually detected in the control and 231CM conditions. We presume that downregulating traction force limits a cell's ability to stretch itself taut over the micropillars, thus allowing the nucleus to drop onto the micropillars and deflect them in an outward fashion. Immunofluorescence channels are as follows: actin (orange), fibronectin (green), nucleus (yellow), and micropillar bottoms (blue).

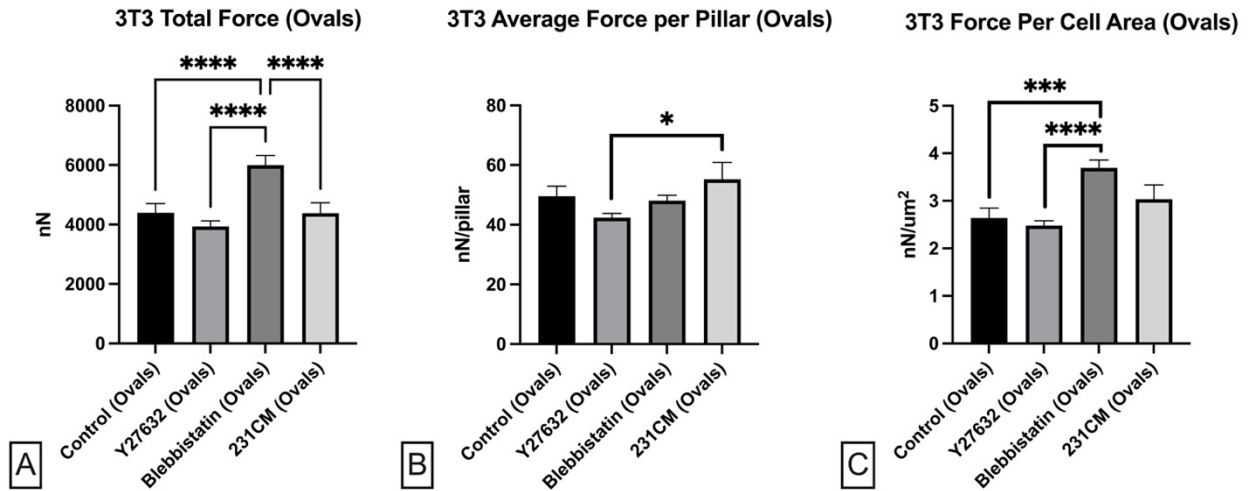


Figure 10: 3T3 cell forces on oval micropillars

Force analysis of NIH-3T3s on oval micropillars. A) Average total force of 3T3s on oval micropillars. Cells in the blebbistatin treatment group displayed significantly higher total force than all other groups. B) 3T3 total force averaged by pillar count. A significant difference in force was found between the Y-27632 treatment condition and the 231CM condition. This allows us to conclude that Y-27632 downregulates force slightly from the control, while treatment with 231CM slightly upregulates force generation. C) 3T3 force normalized by total cell area. Cells in the blebbistatin group have a significantly higher force per area than the control and Y-27632 groups.

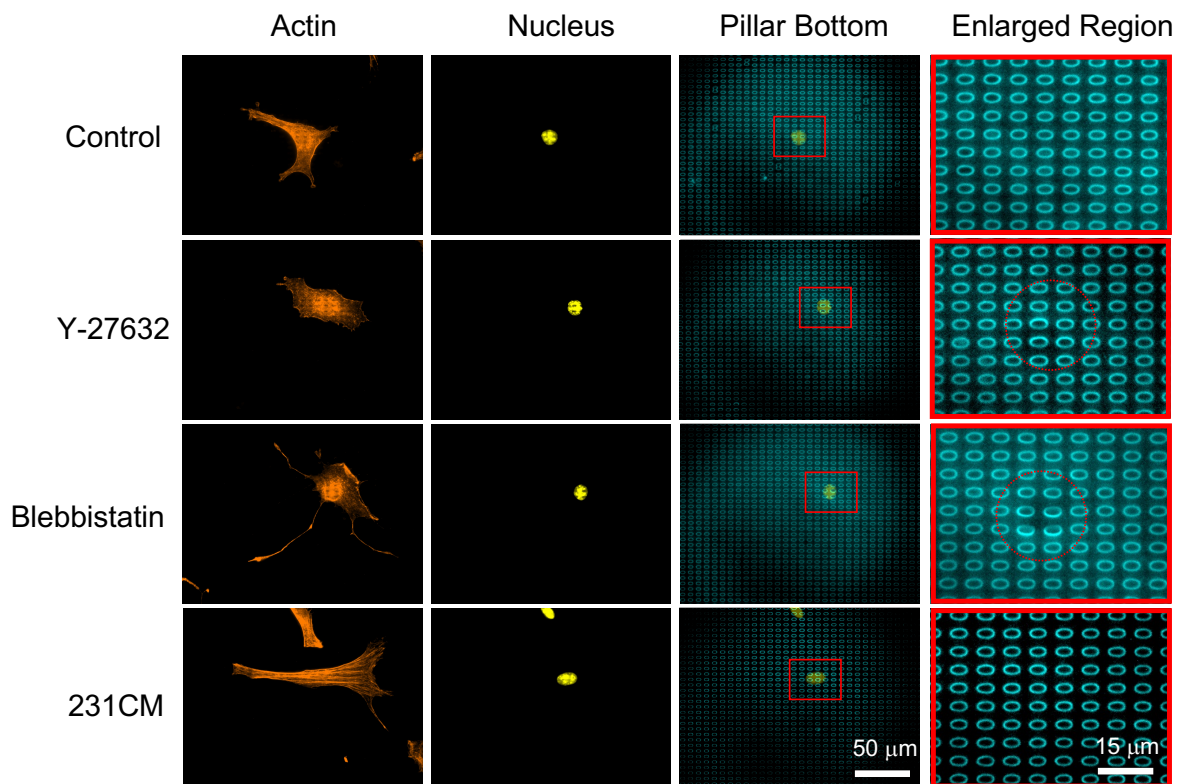


Figure 11: Nuclear micropillar deflections of oval micropillars

Referencing the same cells displayed above in Figure 5, enlarged regions of the micropillars under cell nuclei are presented in the last column. In the enlarged regions, areas directly under the nuclei in the Y-27632 and blebbistatin conditions are identified within the red dotted circle. Similar to the results on circular cross section micropillars, we can visualize micropillar deflections directly under the cell nuclei in both Y-27632 and blebbistatin treatment conditions while no deflections can be visually detected in the control and 231CM conditions. We presume that downregulating traction force limits a cell's ability to stretch itself taut over the micropillars, thus allowing the nucleus to drop onto the micropillars, deflecting them in an outward fashion. Immunofluorescence channels are as follows: actin (orange), fibronectin (green), nucleus (yellow), and micropillar bottoms (blue).

3.3.3 NIH-3T3 alignment on circular and oval micropillars:

Finally, we assessed the alignment potential of NIH-3T3s. Plotting these data as rose plots (Figure 12), we are able to visualize that 3T3s do show some alignment to the oval micropillars and Y-27632 and 231CM groups seem to align the best. Statistical analysis of the data revealed there was no difference in alignment on circular micropillars across all treatment conditions. Although there is no difference, all of their averages are near 45 degrees, in a 0 – 90-degree range, which tells us that they are, indeed, randomly aligned on circular micropillars. Between treatment groups, 3T3s also showed no significant difference in alignment on oval micropillars (Figure 13B), but when comparing all groups to the control condition on circular micropillars (Figure 13C), they show a significant decrease in their average degrees from the X axis, indicating that the ovals are stimulating cell alignment, and limiting force via Y-27632 or blebbistatin does not disrupt alignment.

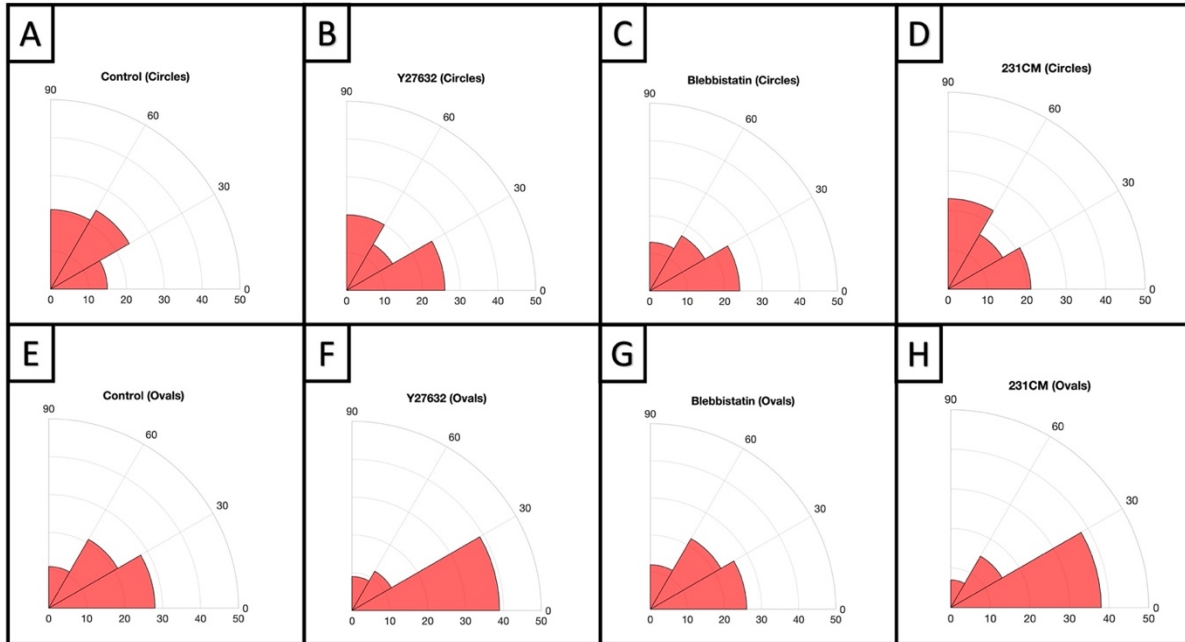


Figure 12: NIH-3T3 cell orientation rose plots

3T3s, in the control condition, on oval micropillars (E) show increased alignment when compared to their counterparts seeded on circular micropillars (A). Treatment with Y27632 (F) results in higher alignment on ovals than on circular micropillars (B). Cells in the blebbistatin treatment group display similar levels of alignment to their control on circular micropillars (C) and control cells on ovals (E). Treatment with 231CM (H) increased cell alignment when compared to control conditions. Overall, cells displayed random alignment on circular micropillars across all treatment groups as expected. On oval micropillars, cells in the Y-27632 and 231CM groups showed the highest levels of alignment.

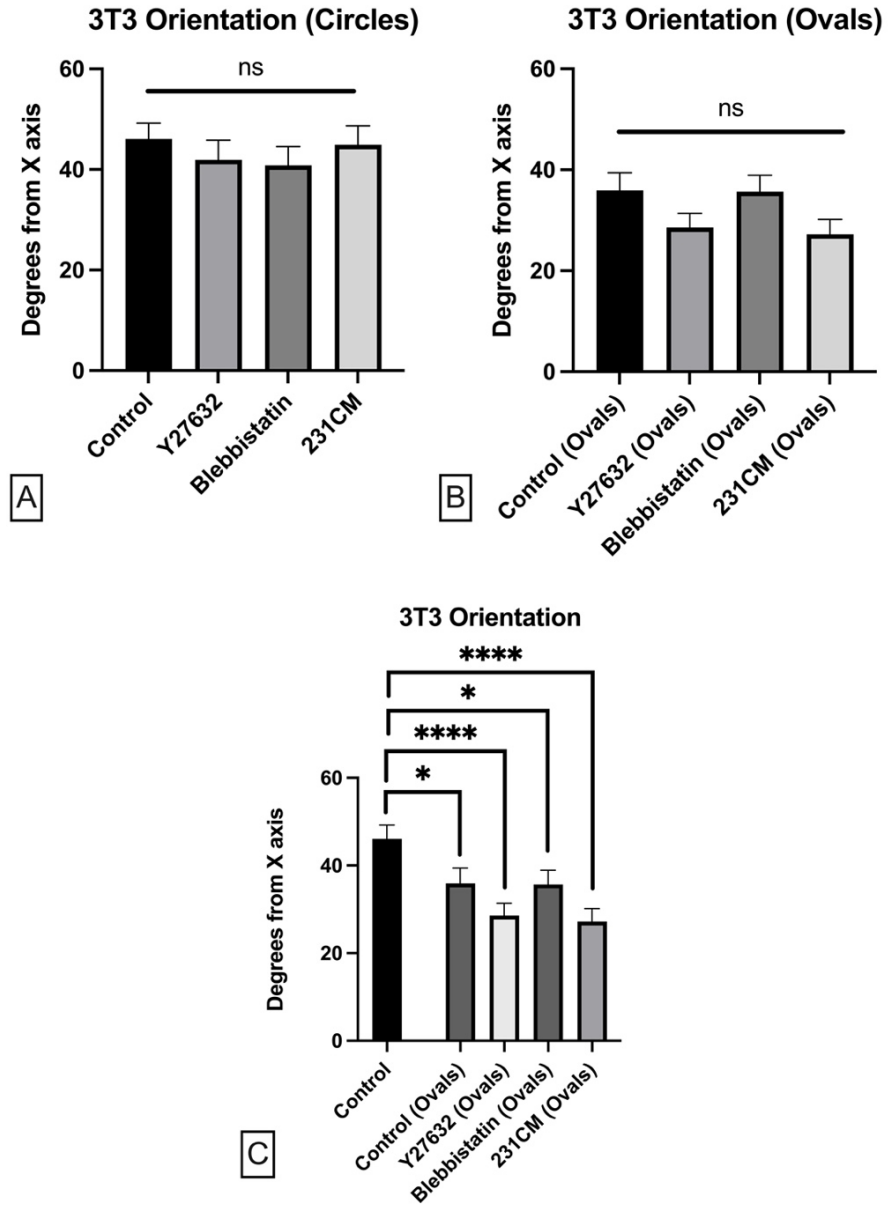


Figure 13: Analysis of 3T3 orientation

A) As expected, 3T3s on circular micropillars showed no significant differences in alignment. 3T3s treated with Y37632 or Blebbistatin showed no significant change in alignment between the circular and oval micropillar substrates. B) Average 3T3 orientation on oval micropillars. 3T3s show no significant difference in alignment across all treatment groups. C) When compared to the control on circular micropillars, cells in all treatment groups on oval micropillars showed

significantly decreased average degrees from the X axis values, indicating that they are all exhibiting some alignment to the major axis of the oval micropillars. In summary, a difference in overall alignment was seen between circular and oval micropillar groups, but none of the treatments, Y-27632, Blebbistatin, or 231CM, resulted in a significant difference in alignment on oval micropillars.

ASC Data

3.3.4 ASC Immunofluorescence analysis:

Similar to the assessment of the NIH-3T3s, we began with visual analysis of the immunofluorescence images of ASCs seeded on circular micropillars for 24 hours. Representative images of ASCs on circular micropillars across control, Y-27632, blebbistatin and 231CM treatment conditions are presented in Figure 14. Normal ASCs show distinct cell bodies with fibrillar actin and, surprisingly, minimal FN assembly. When treated with Y-27632, ASCs display a more elongated morphology with less prominent actin fibrils and increased intracellular FN staining. Blebbistatin-treated ASCs displayed an increase in thin filopodial extensions similar to the NIH-3T3s as well as increased intracellular FN staining compared to the control. ASCs in the 231CM group display larger cell bodies and strong actin stress fibers. 231CM treatment also led to a marked increase in FN assembly on micropillar tops.

On oval micropillars, ASCs displayed similar actin cytoskeleton properties. They display elongated cell bodies in the Y-27632 condition, distinct thin filopodia in the blebbistatin group, and larger cell bodies with prominent actin stress fibers in the 231CM condition. ASCs showed minimal intracellular and assembled FN staining in control, Y-27632, and blebbistatin conditions (Figure 15), but display a remarkable increase in FN assembly when treated with 231CM.

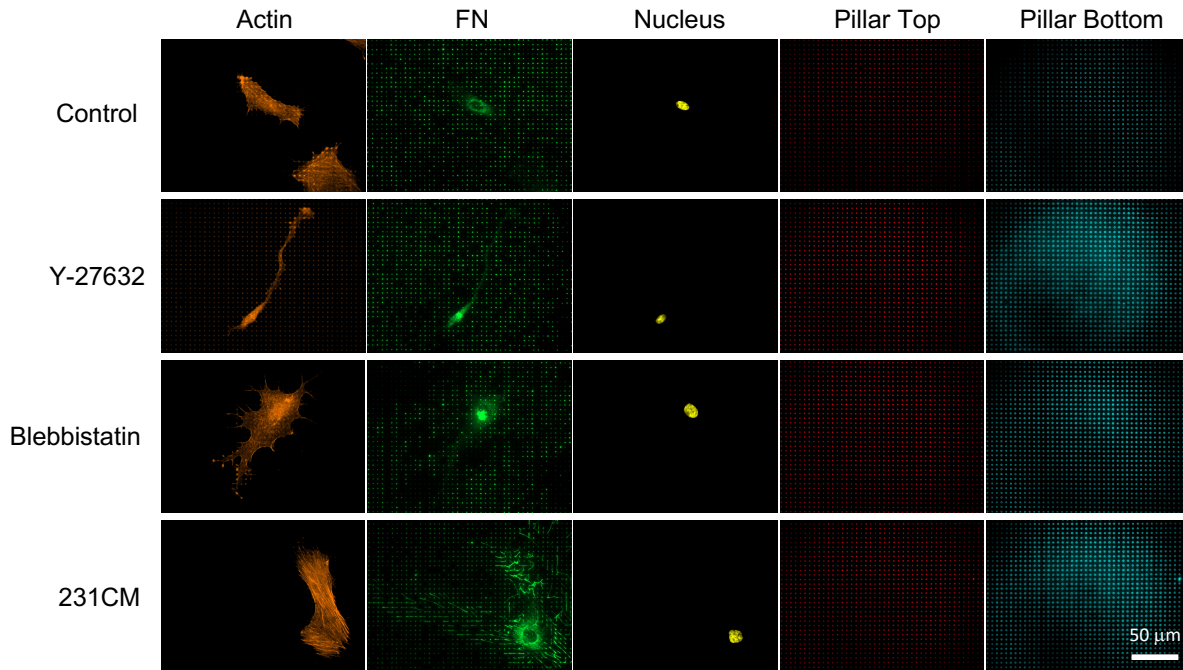


Figure 14: Immunofluorescence images of ASCs on circular micropillars

Representative images of ASCs seeded on circular cross section (isotropic) micropillars for 24 hours. Cells were stained for actin (orange), fibronectin (green), nucleus (yellow), micropillar tops (red), and micropillar bottoms (blue). Cells were treated with either 20 μ M Y-27632, 20 μ M blebbistatin, or MDA-MB-231 conditioned media 90 minutes after seeding. Cells in the control condition had distinct actin cytoskeletons with limited presence of large diameter actin stress fibers. Control cells exhibited minimal FN expression and assembly. When compared to the control condition, cell treated with Y-27632 displayed a more slim and elongated morphology (actin) and greater intracellular staining for FN. FN staining was also noted to colocalize over the nucleus. Blebbistatin-treated cells displayed larger cell bodies with multiple thin, elongated filopodia. They also displayed decreased FN fiber assembly but greater intracellular FN staining. Cells treated with MDA-MB-231 conditioned media displayed larger cell bodies and a notable increase in actin stress fibers throughout the cytoskeleton. 231CM treated cells exhibited increased

intracellular FN and greatly increased FN fibril assembly on micropillar tops. FN fibers can also be observed on unoccupied areas of the image, indicating that cells are assembling and depositing FN during migration. All images were taken on a Zeiss Axio Observer microscope using a 63x magnification oil objective. Scale bar represents 50 μM .

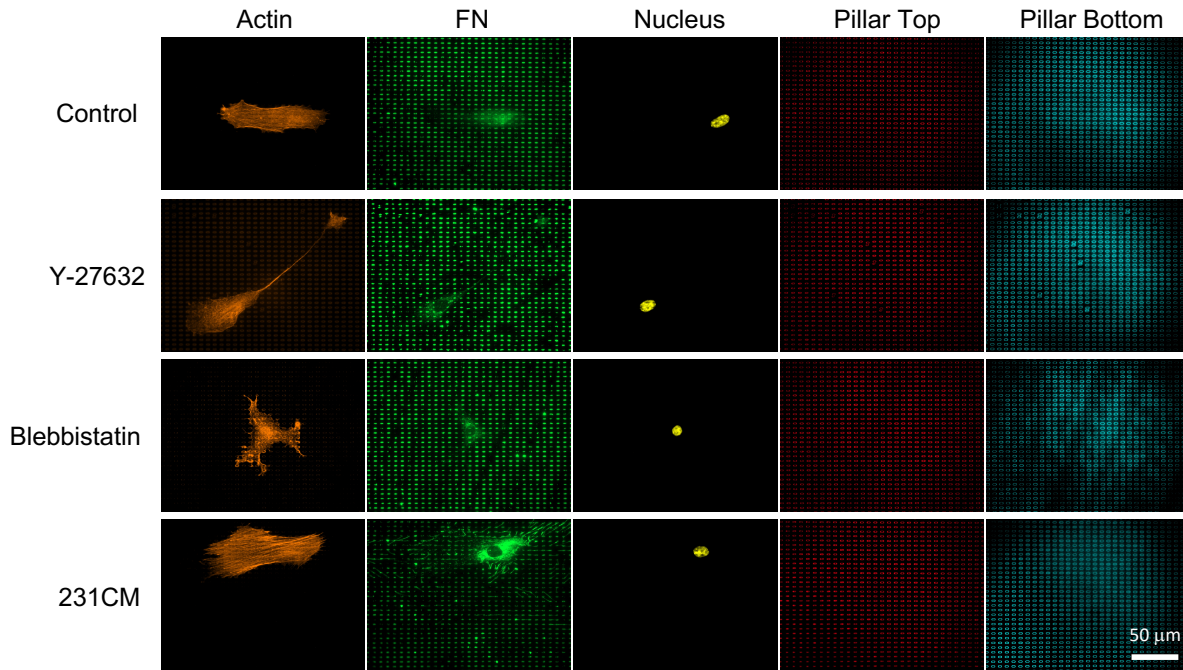


Figure 15: Immunofluorescence images of ASCs on oval micropillars

Representative images of ASCs seeded on oval cross section (anisotropic) micropillars for 24 hours. Cells were stained for actin (orange), fibronectin (green), nucleus (yellow), micropillar tops (red), and micropillar bottoms (blue). Cells were treated with either 20 μM Y-27632, 20 μM blebbistatin, or MDA-MB-231 conditioned media 90 minutes after seeding. When compared to the control condition, cells treated with Y-27632 displayed a more elongated morphology (actin) and showed no observable difference in FN staining. Similar to their counterparts on circular micropillars, blebbistatin-treated cells exhibited multiple thin elongated filopodia. Cells treated with MDA-MB-231 conditioned media displayed larger cell bodies and increased actin stress fibers in the cytoskeleton. 231CM treated cells exhibited increased intracellular FN and FN fibril assembly on micropillar tops. All images were taken on a Zeiss Axio Observer microscope using a 63x magnification oil objective. Scale bar represents 50 μM .

3.3.5 ASC MATLAB analysis of cell area, fibril area, and force:

We began by quantifying ASC cell area and viewed some unique results. On circular micropillars, none of the treatment groups showed a significant difference in cell area from the control. However, a significant difference was noted between the Y-27632 and 231CM groups, suggesting that Y-27632 could be slightly decreasing cell area and 231CM treatment could be slightly increasing cell area (Figure 16A). On oval micropillars, the difference was more distinct, as cells in the Y-27632 treatment group displayed significantly lower cell area than all other groups (Figure 16B). Interestingly, when comparing the treatment groups between circular and oval micropillars, we found the control, blebbistatin and 231CM groups showed a significant increase in cell area on oval micropillars, but cells in the Y-27632 group did not, suggesting that downregulating force with Y-27632 limits a cell's ability to respond to the mechanical cues provided by oval micropillars (Figure 16C).

Analysis of total fibril area on circular micropillars (Figure 17A) led us to find that blebbistatin treatment significantly decreased FN expression and assembly while 231CM treatment significantly increased FN assembly. On oval micropillars, both Y-27632 and blebbistatin treatments downregulated FN assembly while 231CM treatment once again significantly increased FN assembly (Figure 17B). Comparison of FN assembly between circular and oval micropillars (Figure 17C) shows that cells in all treatment conditions express and assemble less FN on oval micropillars.

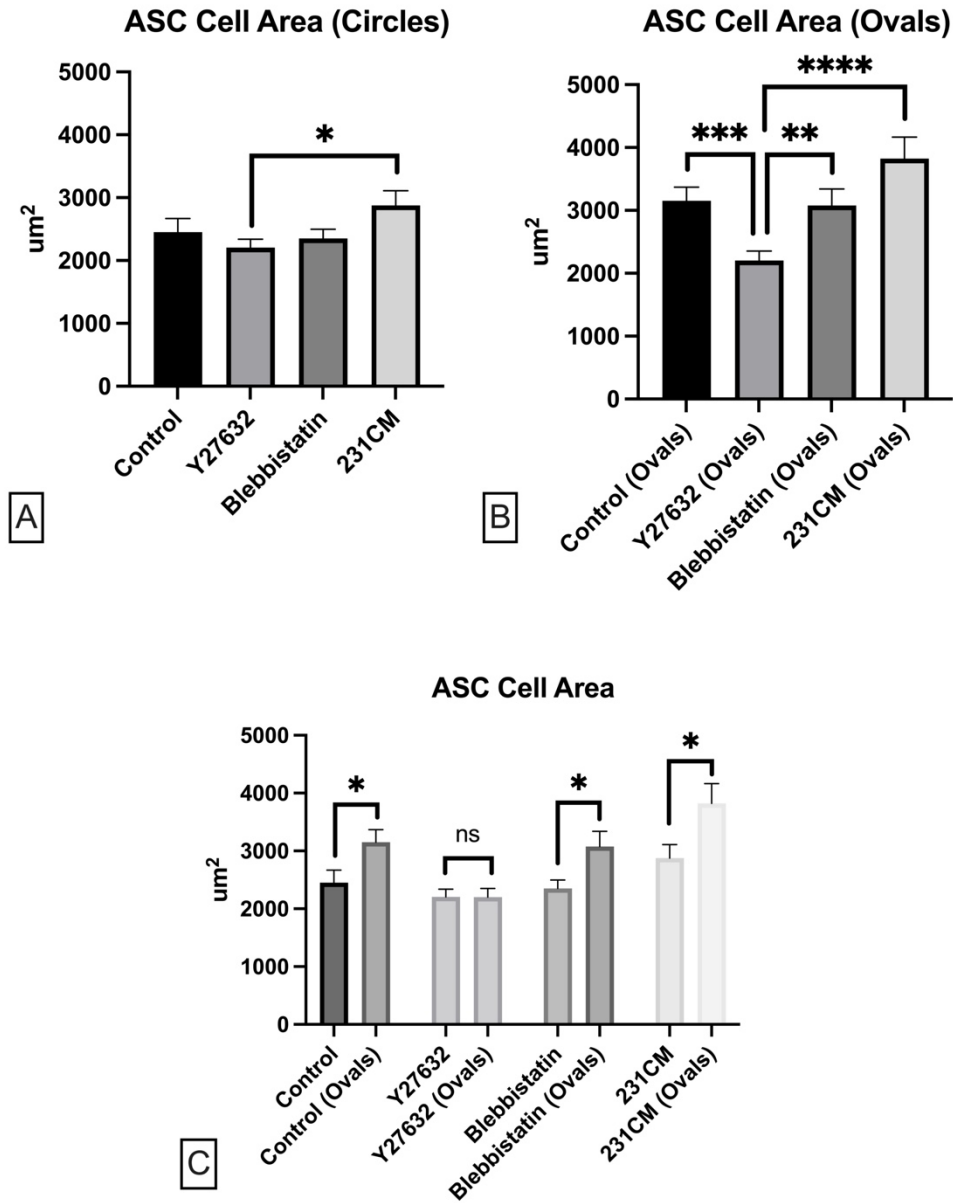


Figure 16: ASC cell area quantification

ASC cell area quantified on both circular and oval cross section micropillars across control, Y-27632, blebbistatin, and 231CM conditions. A) ASCs on circular cross sections micropillars show no significant difference across all conditions when compared to the control, however, cells treated with 231CM did show a significantly larger average area compared to the Y-27632 group. B) ASCs on oval cross section micropillars. Cells treated with Y-27632 demonstrate significantly

smaller cell area than all other groups. C) ASCs in control, blebbistatin and 231CM conditions spread to a significantly larger size on oval micropillars when compared to those exposed to the same treatment on circular micropillars. In contrast, treatment with Y-27632 on ovals decreased cell area to a level comparable to cells on circular micropillars in the control and Y-27632 groups.

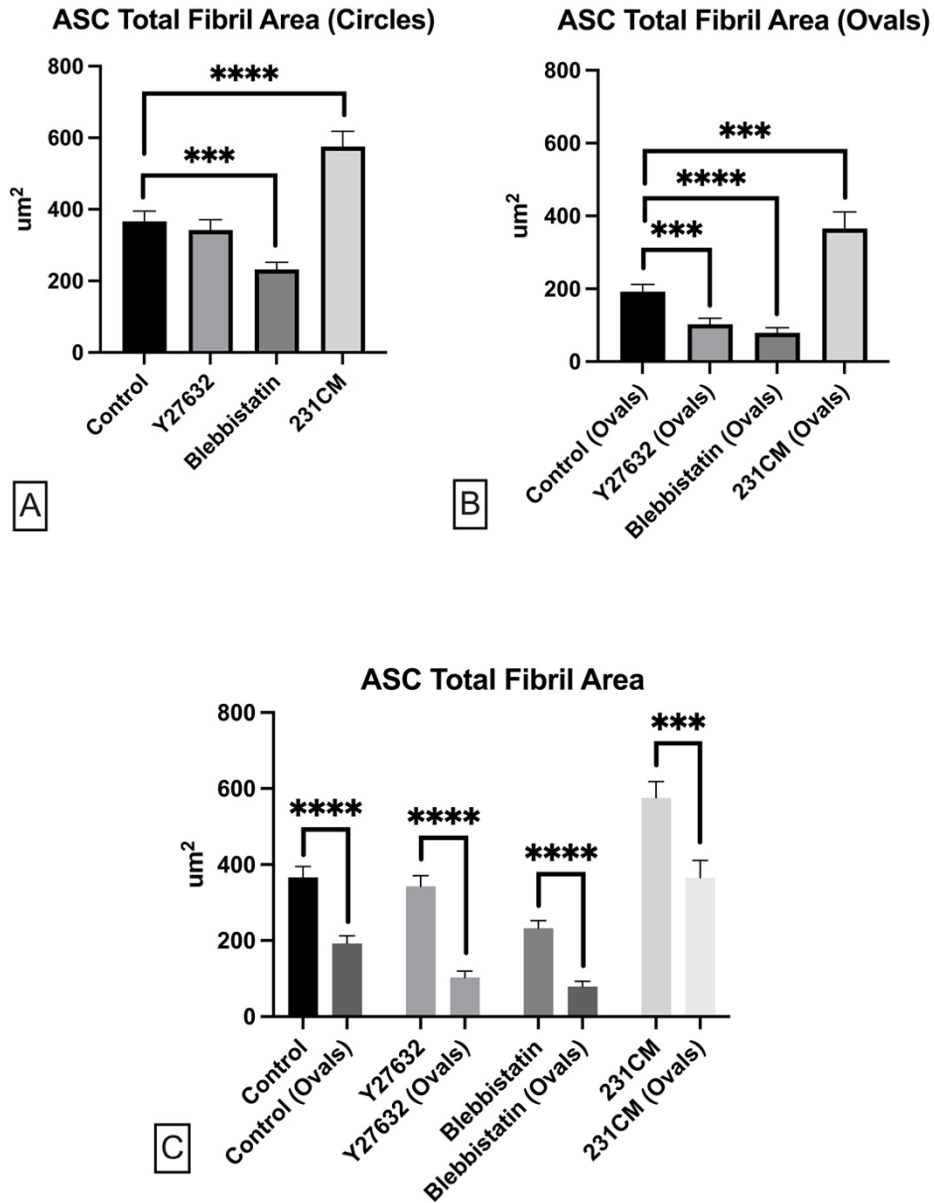


Figure 17: ASC total fibril area quantification

ASC total fibronectin fibril area on both circular and oval cross section micropillars. Cells on both areas of the substrate were analyzed across control, Y-27632, Blebbistatin, and 231CM treatment conditions. A) Cells treated with Y-27632 displayed no significant change from the control condition. Cells on circular micropillars treated with blebbistatin showed a significant decrease in fibril assembly while cells treated with 231CM showed a significant increase. B) On oval

micropillars, cells treated with Y-27632 and blebbistatin assembled significantly less FN than the control while cells treated with 231CM showed significantly increased FN assembly. C) Cells across all treatment groups assembled significantly less FN on oval micropillars than on circular micropillars.

Assessing force characteristics on circular micropillars, we found that Y-27632 and blebbistatin caused no significant change while 231CM treatment resulted in increased total force. When normalized by number of occupied pillars, Y-27632 and blebbistatin showed a significant decrease in the force applied per pillar. When normalizing total force by cell area, we see no significant differences across all groups (Figure 18C). We noted completely different characteristics on oval micropillars. When comparing total force, the data show that the blebbistatin treatment group shows a larger force than the Y-27632 treatment group. Normalizing total force to the number of occupied pillars shows us that there is no significant difference across all conditions. Finally, when normalizing by cell area, we noted that Y-27632 and blebbistatin treatment groups display a higher force per area than the control and 231CM conditions (Figure 19C).

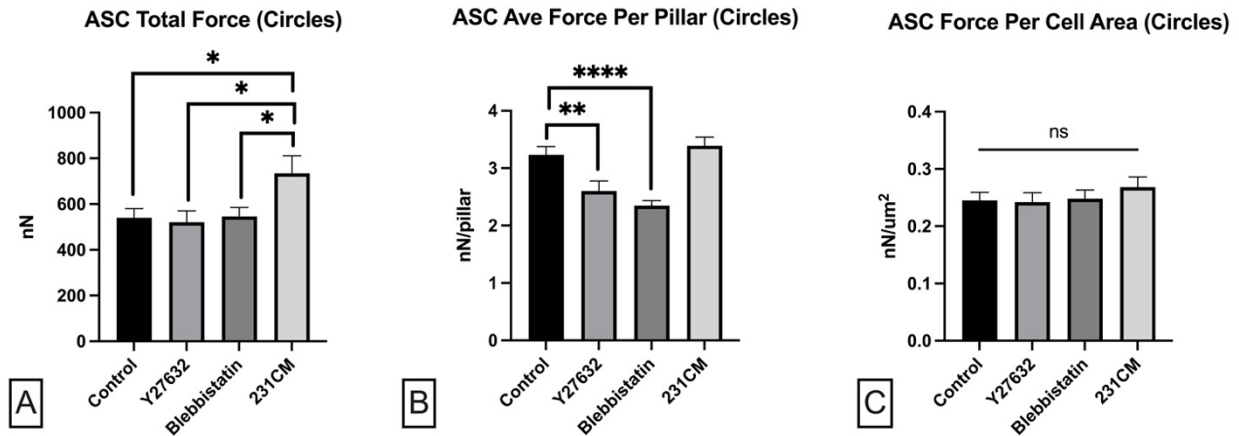


Figure 18: ASC force analysis on circular micropillars

Force analysis of ASCs on circular micropillars. A) ASCs treated with 231CM generated significantly higher total force than the control, Y-27632, and blebbistatin conditions. B) Total force normalized against the number of occupied pillars shows that cells in the Y-27632 and blebbistatin groups displayed lower force per pillar than both control and 231CM groups. C) When normalized by cell area, ASCs displayed no significant difference in force across all conditions. This is supported by the data provided in Figure 16, which shows that variance in cell size results in differences found in panels A and B, but when normalized against cell area, ASCs in all groups generated approximately the same amount of force.

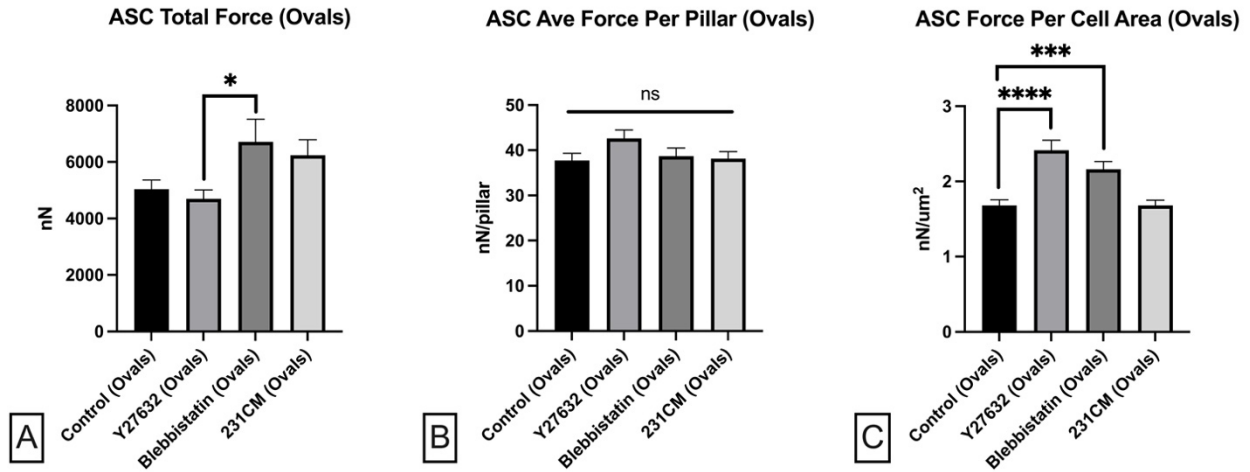


Figure 19: ASC force analysis on oval micropillars

Force analysis of ASCs on oval micropillars. A) Average total force of 3T3s on oval micropillars. Cells in the blebbistatin treatment group displayed significantly higher total force than all other groups. B) 3T3 total force averaged by occupied pillar count. There was no significant difference in force per pillar across all groups. C) 3T3 force normalized by total cell area. Cells in the Y-27632 and blebbistatin groups have a significantly higher force per square micrometer when compared to the control and 231CM groups.

3.3.6 ASC alignment on circular and oval micropillars:

Finally, when we assessed the alignment capability of ASCs, the rose plots show that ASCs are highly mechanoresponsive and align extremely well to the oval axis of the micropillars even in the control condition. Treatment with Y-27632 and blebbistatin caused a noticeable drop in overall alignment, while cells treated with 231CM align comparable control (Figure 20). Statistical analysis of the data in Figure 21A show randomized alignment on circular micropillars across all treatment groups. On oval micropillars, the control and 231CM groups show extremely strong alignment, while treatment with Y-27632 and blebbistatin disrupt mechanosensing enough to significantly decrease alignment (Figure 21B). When comparing the orientation on oval micropillars versus circular micropillars, we found that blebbistatin treatment had no significant difference from the control cells on circular micropillars. This suggests that treatment with blebbistatin disrupts mechanosensing enough to result in randomized cell alignment, meaning that the cells are totally unable to respond to the mechanical cues of the oval micropillars.

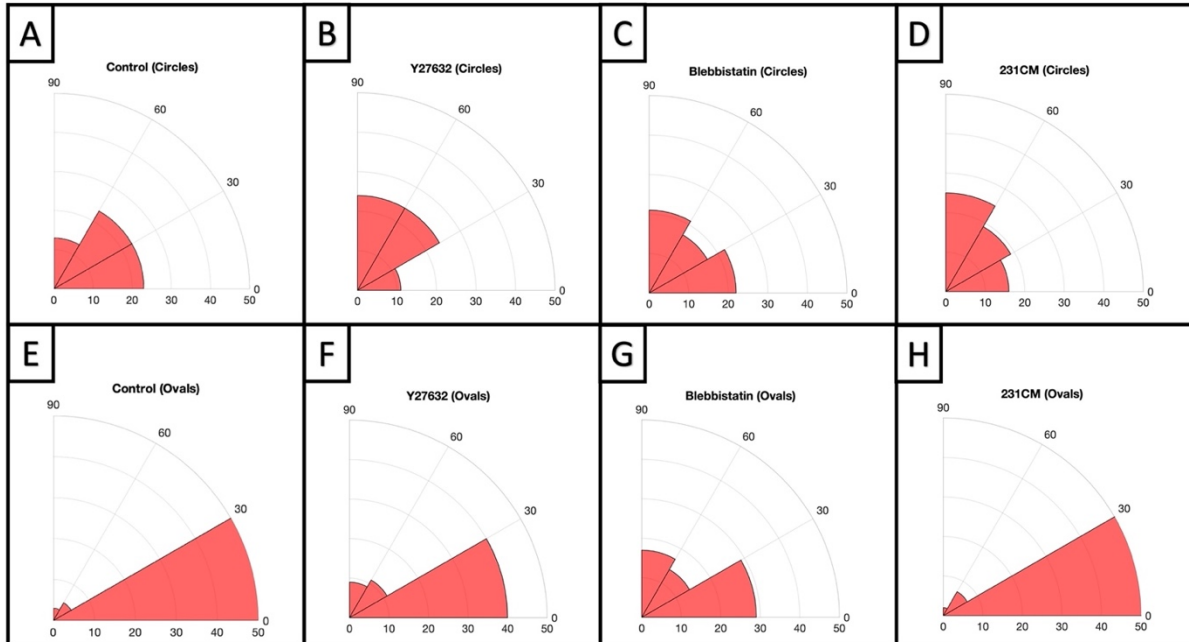


Figure 20: Rose plots of cell ASC alignment on circular and oval micropillars

Cells oriented within 0-30 degrees from the major axis of the ovals are considered to be highly aligned. Increased overall cell alignment is demonstrated by an increased number of cells in the 0-30 degree range. Cells were treated with either Y27632, blebbistatin, or 231CM. All treatment conditions showed increased cell alignment on oval micropillars. Treatment with Y27632 and Blebbistatin led to a decrease in cell alignment, as noted by an increased number of cells with higher degree offset from the major axis of the ovals (0 degrees), when compared to control and 231CM conditions.

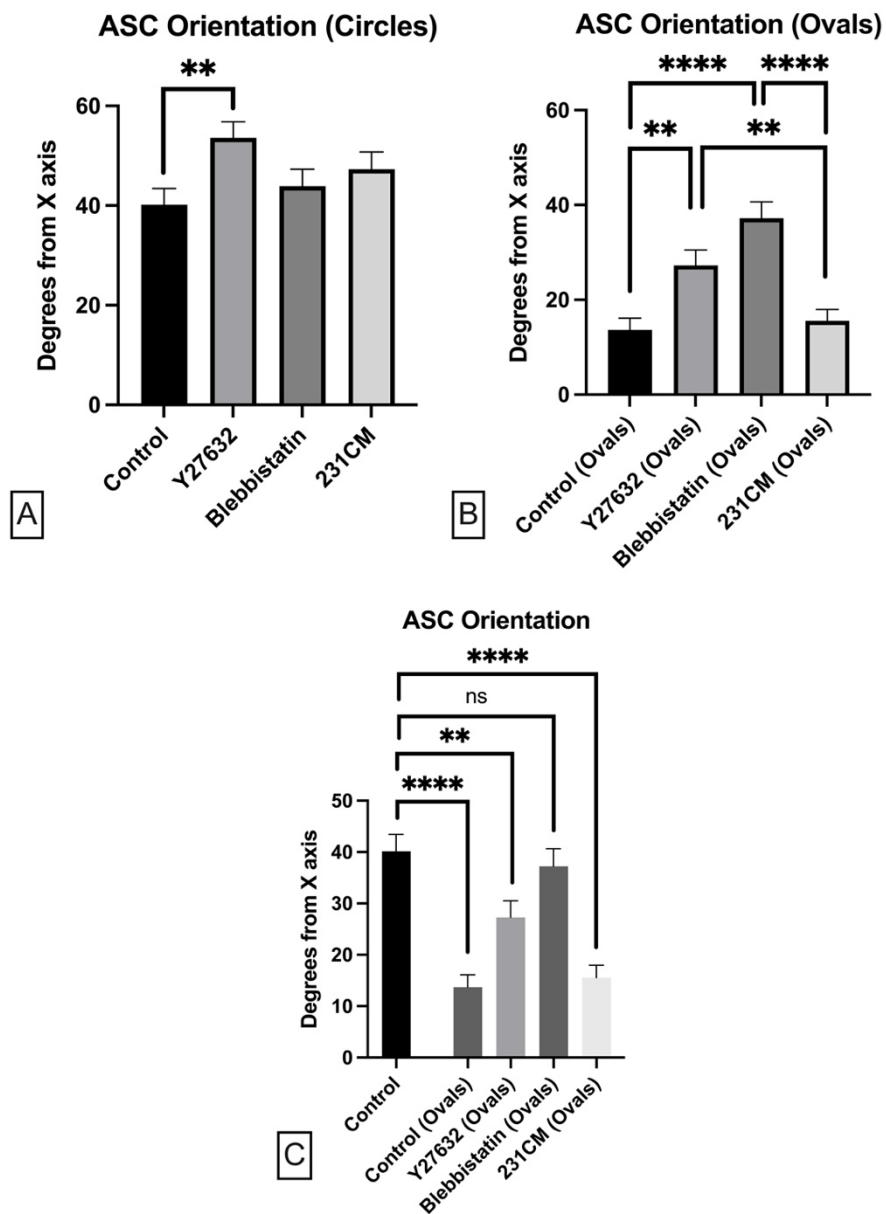


Figure 21: ASC cell orientation quantification

ASC average cell orientation on circular and oval micropillars across the following conditions: control, Y27632, blebbistatin, and 231CM. A) ASCs on circular micropillars show a high average orientation, indicating randomized alignment. B) ASCs on oval micropillars, in control and 231CM groups, show decreased average deviation from the X axis, indicating increased alignment.

Treatment with Y27632 and blebbistatin resulted in a significantly higher average orientation than the control and 231CM groups. This clearly demonstrates that treatment with Y-27632 or blebbistatin reduces a cell's mechanosensing ability, and consequently, its ability to align itself to mechanical stimuli. Treatment with 231CM showed no significant difference from the control, indicating that ASCs are highly mechanoresponsive and fully capable of alignment even in their native state.

3T3 – ASC Comparison Data

3.3.7 NIH-3T3 vs ASC MATLAB analysis of cell area, fibril area, and force:

After analyzing each cell line individually, we compared key characteristics, such as cell size, ECM assembly, force and alignment capability between the two cell lines and found some interesting results. Beginning with cell area, we were able to confirm our visual observation that generally ASCs seemed larger than 3T3s. The data in Figure 22 show that ASCs are significantly larger than 3T3s across all treatment conditions on both circular and oval micropillar substrates.

Next, we compared FN fibril assembly between the two cell lines. On circular micropillars, 3T3s and ASCs assembled the same amount of FN in the control condition. Across all other conditions, ASCs seemed to display a heightened response to the treatments when compared to 3T3s. This is indicated by a larger decrease of FN assembly when force was downregulated by Y-27632 and blebbistatin, and a larger increase in FN assembly when treated with 231CM (Figure 23A). On oval micropillars, ASCs assembled less FN than 3T3s in control, Y-27632, and blebbistatin groups, and assembled a similar amount of FN to 3T3s when treated with 231CM (Figure 23B).

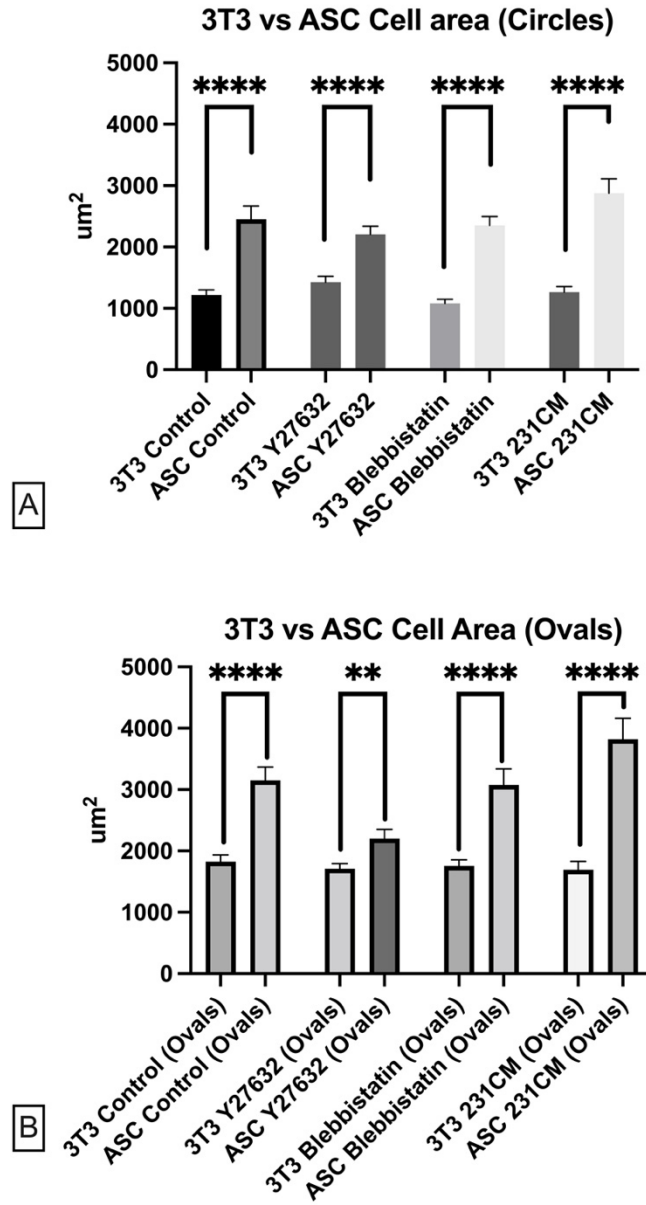
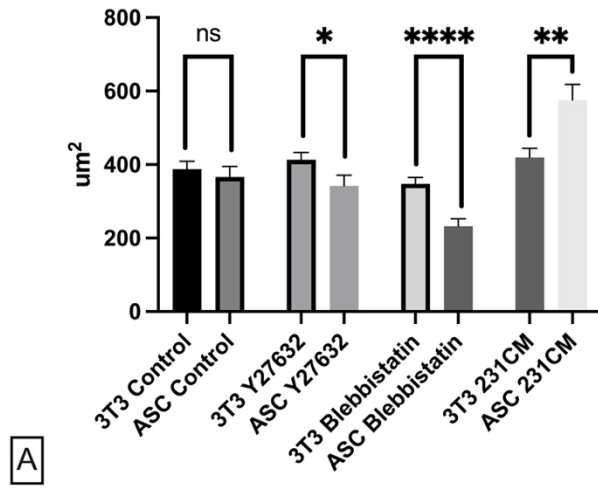


Figure 22: 3T3 vs ASC cell area comparison

Cell area comparisons on both circular (A) and oval (B) micropillars across control, Y-27632, blebbistatin and 231CM treatment conditions. ASCs were significantly larger than 3T3s in all conditions on both isotropic and anisotropic substrates.

3T3 vs ASC Total fibril area (Circles)



3T3 vs ASC Total fibril area (Ovals)

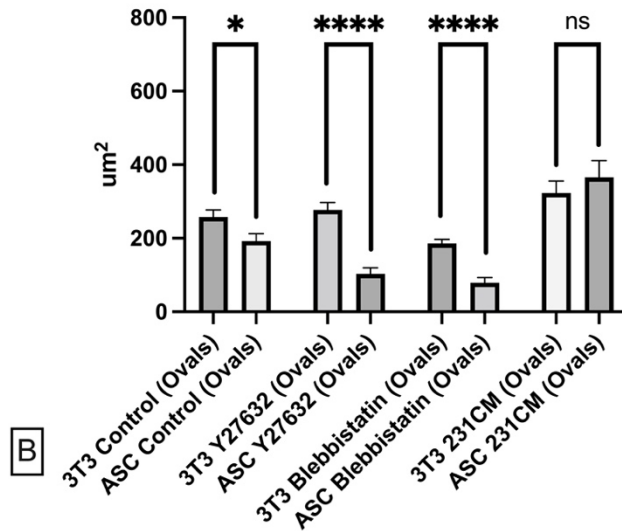


Figure 23: 3T3 vs ASC total fibril area comparison

Total fibril area comparisons on both circular (A) and oval (B) micropillars across control, Y-27632, blebbistatin and 231CM treatment conditions. On circular micropillars, 3T3s and ASCs assembled the same amount of FN in the control condition. When treated with Y-27632 and blebbistatin ASCs assembled significantly less FN than 3T3s. When exposed to 231CM, ASCs assembled significantly more FN than 3T3s. On oval micropillars, ASCs assembled less FN than

3T3s in the control, Y-27632, and blebbistatin conditions, while assembling the same amount of FN when treated with 231CM.

We then compared force generation between the two cell lines. The data in Figure 24 show total force averages in 3T3s and ASCs on both circular and oval micropillar substrates. On circular micropillars, ASCs generate higher total force than the 3T3s in the control, Y-27632, and 231CM conditions. On oval micropillars, ASCs generated significantly higher forces in the Y-27632 and 231CM conditions. In Figure 25, we normalized total force by cell area and found that 3T3s actually generate higher forces than ASCs in blebbistatin and 231CM treatment conditions on circular micropillars per μm^2 . On oval micropillars, 3T3s generated higher force per μm^2 than ASCs in control, blebbistatin, and 231CM conditions. This indicates that although 3T3s are generally smaller than ASCs, on oval micropillars, they generate higher forces for their size. It is worth noting that across both circular and oval micropillar sets of data, ASCs generate either an equivalent or lower level of force than 3T3s, but never greater.

3.3.8 NIH-3T3 vs ASC alignment on circular and oval micropillars:

Finally, we compared both cell lines' ability to respond to anisotropic stiffness and contact guidance cues by measuring their orientation with respect to the major axis of the oval micropillars. When force was not downregulated, the data in the control and 231CM conditions indicate that ASCs are able to align themselves along oval micropillars much better than 3T3s. Inhibiting force using Y-27632 or blebbistatin disrupted mechanosensing in ASCs, increasing their average orientation to match that of the 3T3s. All the data indicate that ASCs are significantly more mechanoresponsive than 3T3s and are also more susceptible to the effects of force inhibitors, such as Y-27632 and blebbistatin.

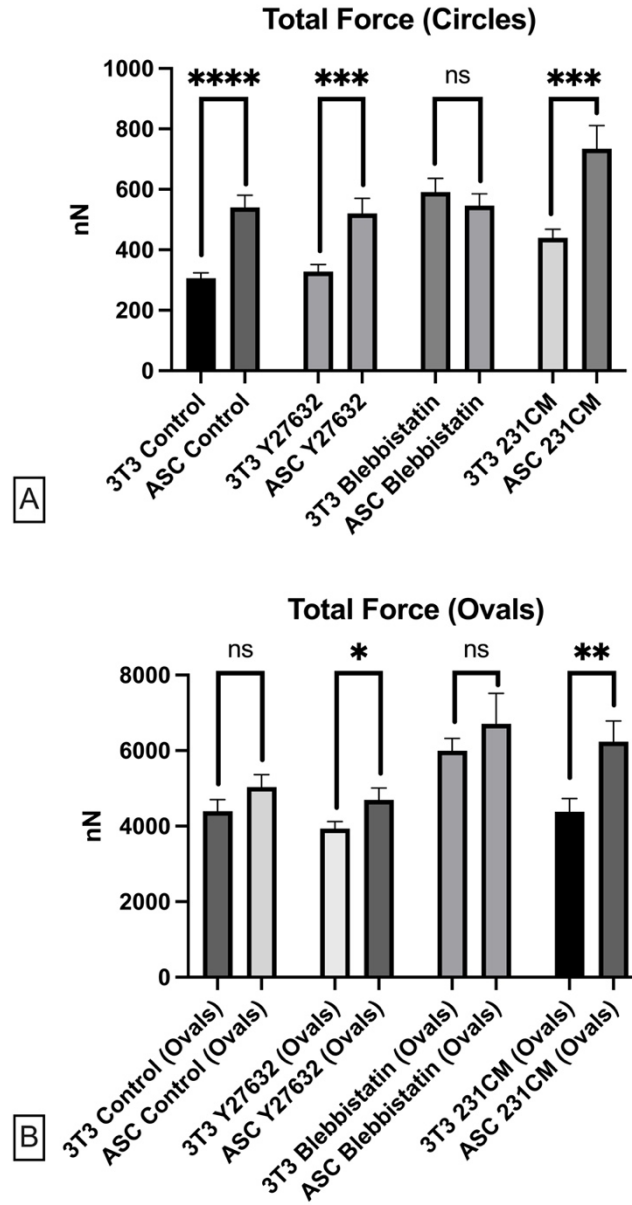


Figure 24: 3T3 vs ASC total force comparison

Total force comparison between 3T3s and ASCs across control, Y-27632, blebbistatin, and 231CM conditions on both circular and oval micropillars. On circular micropillars, ASCs generated significantly larger forces than 3T3s in the control, Y-27632, and 231CM conditions, but there was no significant difference in force when both cells were treated with blebbistatin. We predict that this unexpected difference is due to the nuclear sagging that occurs when 3T3s are treated with

blebbistatin. On oval micropillars, ASCs generated larger forces in the Y-27632 and 231CM conditions than 3T3s.

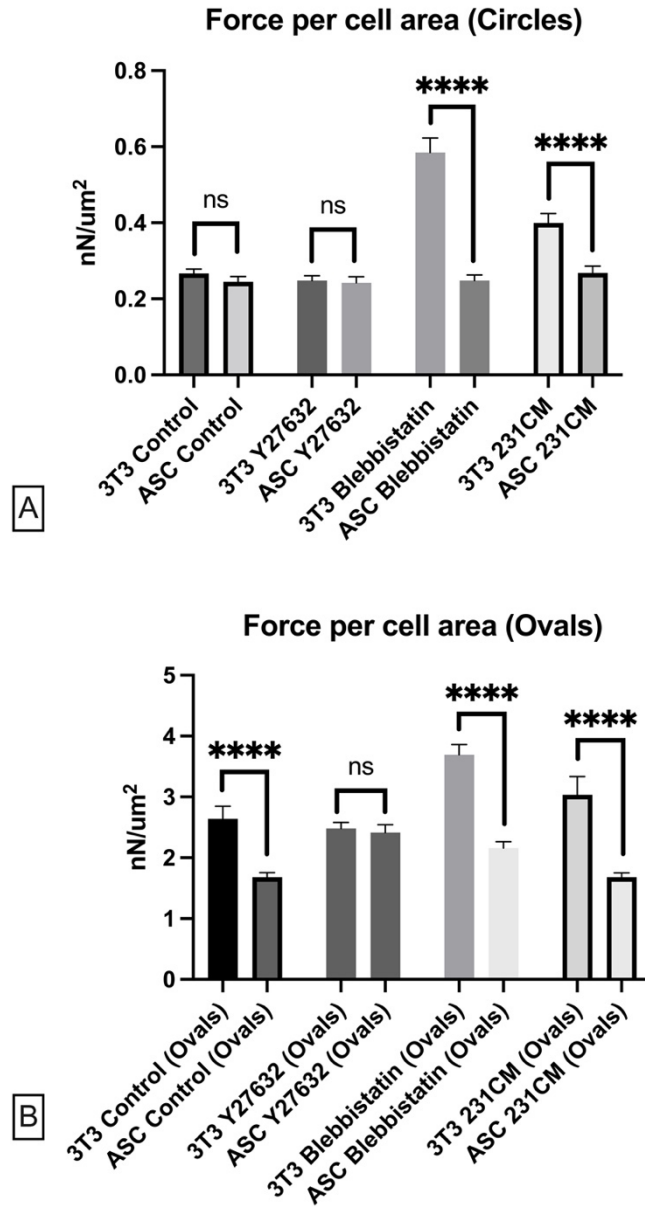


Figure 25: 3T3 vs ASC force per cell area comparison

A) When total force was normalized by cell area, 3T3s and ASCs showed no significant difference in force in the control and Y-27632 conditions. 3T3s generated significantly larger forces than ASCs in the blebbistatin and 231CM conditions. B) On oval micropillars, 3T3s generated higher traction forces than ASCs in the control, blebbistatin, and 231CM groups.

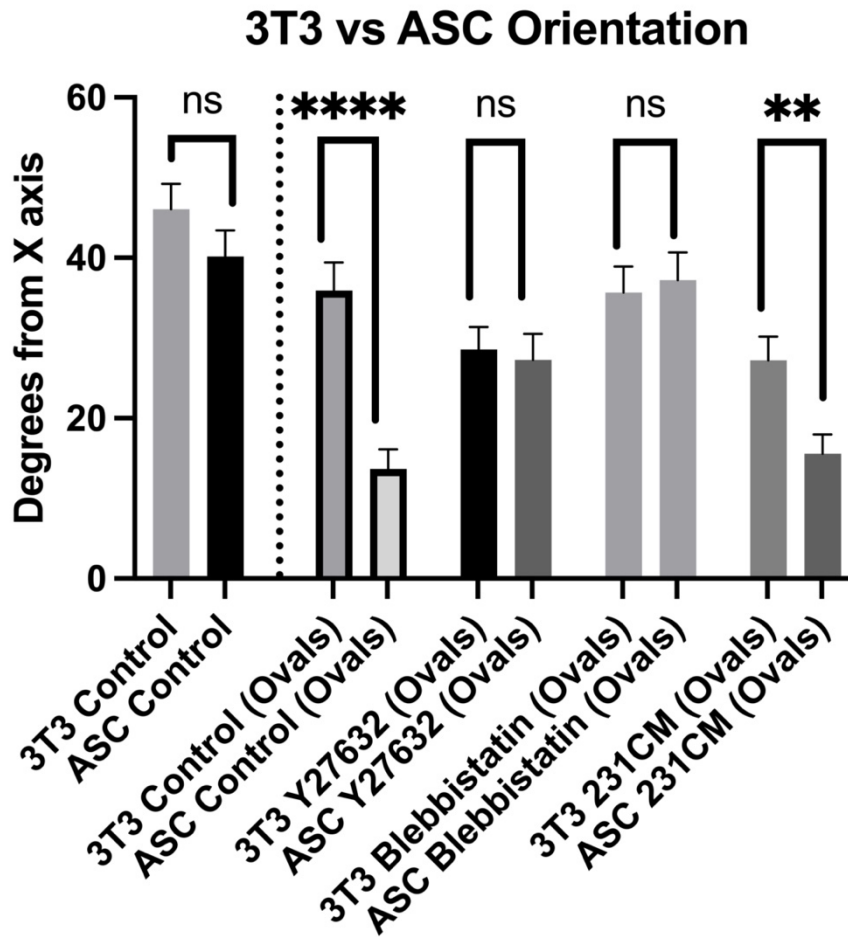


Figure 26: 3T3 vs ASC Orientation comparison

3T3s and ASCs compared across control, Y-27632, blebbistatin and 231CM treatment groups and shown relative to controls on circular micropillars. On circular micropillars, 3T3s and ASCs both showed high average orientations and were not significantly different from each other, indicating randomized alignment. When the cell lines were compared on oval micropillars, the data show a significant difference in level of alignment in control and 231CM treated groups, while showing no significant difference between the cell lines treated with Y-27632 and blebbistatin. The data indicate that ASCs are highly responsive to the anisotropic mechanical cues provided by oval

micropillars, and that downregulation of force disrupts ASC alignment, bringing it to a level comparable to that of the 3T3s.

3.4 Discussion

In this chapter we probed fibroblast response to isotropic and anisotropic substrates. NIH-3T3s and ASCs were seeded on both circular and oval cross section micropillar substrates and cultured for 24 hours. Samples were then fixed and stained for actin, the nucleus, and FN assembly. We then investigated the effect of downregulating and upregulating a cell's ability to generate and exert force onto its environment to observe the effect on mechanosensing. We used Y-27632, a ROCK inhibitor, and blebbistatin, an inhibitor of actomyosin contractility, to downregulate force, and used MDA-MB-231 conditioned media to upregulate force. Our findings show that on oval micropillars, 3T3s overall displayed larger cell areas and decreased FN assembly. ASCs also displayed larger cell areas on oval micropillars, but treatment with Y-27632 attenuated this difference, making areas comparable to ASCs on circular micropillar controls. Overall, ASCs generally displayed equivalent or greater cell area than 3T3s.

3T3s displayed generally lower FN assembly on oval micropillars, and blebbistatin treatment further reduced FN assembly. Generally, cells assemble more ECM on stiffer substrates, but here, we see the opposite result. We believe that this discrepancy is produced by our analysis of the immunofluorescence images. When quantifying FN assembly, we begin by taking the total FN area in the images. We then subtract out the total area of micropillar tops that have FN on them yielding FN produced by the cell. Since oval micropillars have a larger surface, when compared to circular micropillars, we see a greater decrease in FN area when subtracted. We believe that this is the reason behind seeing overall lower FN assembly on oval micropillar substrates.

FN fibril assembly in ASCs on circular micropillars was able to be modulated by blebbistatin (decreased FN assembly) and 231CM (increased FN assembly). On oval micropillars,

ASCs displayed overall decreased FN assembly when compared to respective treatment groups on circular micropillars. Y-27632 and blebbistatin significantly decreased ASC FN assembly and 231CM treatment greatly increased FN assembly on oval micropillars. Overall, in the control scenario on circular micropillars, 3T3s and ASCs assembled similar levels of FN, but ASCs were more responsive to treatments.

Treatment with 231CM stimulated larger traction forces in both 3T3s and ASCs on circular micropillars. Finally, 3T3s showed a significant ability to align to the major axis of oval micropillars, and we were unable to disrupt alignment by limiting force. ASCs, on the other hand, showed a much higher degree of alignment than 3T3s, and their alignment was able to be disrupted by inhibiting force with Y-27632 and blebbistatin. We postulate that these differences may be caused by two different mechanisms. One, the larger cell area of ASCs allows them to interface with a larger area of the substrate, effectively increasing the signal strength of mechanical properties. Two, we believe that ASC's ability to generate larger forces allows them to probe substrate characteristics better resulting in better mechanoresponse.

Overall, we have demonstrated that anisotropic stiffness and contact guidance can modulate key cell characteristics, such as cell size, ECM assembly, and alignment. We can inhibit or enhance these responses using force modulators, such as Y-27632, blebbistatin and 231CM.

Chapter 4

Investigating anisotropic stiffness in a breast cancer progression model

4.1 Rationale

In Chapter 3, we demonstrated that fibroblast cell lines sense and respond to anisotropic mechanical cues, proving that we can use oval micropillars to mimic anisotropic tissues with aligned fibers *in vitro*. We definitively prove that anisotropic stiffness and contact guidance, simulated with oval micropillars, can affect cell characteristics such as cell size, traction forces, ECM assembly, and alignment. We demonstrated that cells do this through the application of force: downregulating force using inhibitors, such as Y-27632 and blebbistatin, can disrupt this response, while upregulating force using 231CM can increase it. Next, we chose to use our validated platform to mimic anisotropic stiffness and contact guidance cues provided by reorganized collagen fibers in an evolving tumor microenvironment (TME).

There are three distinct collagen architectures at various stages of tumor growth which are each unique and are commonly referred to as tissue associated collagen signature (TACS) 1, 2, and 3. At the initial stage of tumor growth, there is a small central accumulation of unorganized collagen fibers (TACS 1). As the tumor continues to grow, malignant cells and resident fibroblasts reorganize this ECM into a layer of aligned collagen fibers which are oriented in a circumferential manner around a central mass of malignant cells. This circumferentially aligned collagen architecture is known as TACS 2. As the tumor continues to grow and turns into a late stage or metastatic tumor, malignant cells tunnel through the circumferential collagen layer and assemble tracks of collagen fibers leading perpendicularly away from the tumor (TACS 3)⁹. The unique collagen architectures at these 3 stages provide varied mechanical cues which can stimulate distinct cell behaviors. We theorize that these mechanical cues play an important role in promoting continued tumor development and determining the metastatic potential of a tumor. Previous works have demonstrated that malignant cells are more invasive in stiffer tissues and migrate with increased persistence and efficiency along linear features⁵⁶⁻⁵⁸. To investigate the effects of varying mechanical cues at different tumor stages, we also had to match them with appropriate cell types most likely to be present at each stage of tumor growth. We chose to use cell lines which are commonly used to represent healthy cells and cells at early and late stages of tumor progression. MCF10A (normal/healthy mammary epithelial cells), MCF10AT1 (pre-malignant/early-stage mammary epithelial cells), and MDA-MB-231 (metastatic/late-stage breast cancer cells) to investigate mechanoresponse as a function of malignancy.

We began by seeding MCF10A, MCF10AT1, and MDA-MB-231 (hereafter also referred to as 10As, AT1s, and 231s) cells on our novel dual stiffness substrate to test epithelial cell response to both anisotropic stiffness and contact guidance cues provided by oval micropillars.

Previous works have shown that healthy epithelial cells (MCF10A) assemble greater ECM when transformed to a mesenchymal phenotype using TGF- β 1²¹. It is well known that ECM assembly requires force and cells which generate more force typically assemble more ECM. Based on this knowledge, other works have demonstrated that malignant cells are responsive to substrate stiffness, migrate faster on stiffer substrates, and follow contact guidance cues^{58,59}. After we established baseline characteristics for these cell lines, we chose to investigate the effect of inflammatory cytokines, which are expressed by malignant cells and normally present in the TME, on epithelial cell morphology, ECM assembly, force, and alignment.

Malignant cells express a variety of inflammatory cytokines in the TME, such as transforming growth factor - beta 1 (TGF- β 1), tumor necrosis factor - alpha (TNF- α), and interleukin 6 (IL-6)^{60,61}. Rather than stimulating cells with individual inflammatory cytokines, we resolved to simulate the overall inflammatory cytokine profile by utilizing media conditioned by metastatic MDA-MB-231 cells. Exposing healthy epithelial cells (10As) to inflammatory cytokines, such as TGF- β 1, stimulates a transformation process known as epithelial-mesenchymal transition (EMT). In EMT, healthy epithelial cells transform from cuboidal morphology and preferring strong cell – cell junctions to a mesenchymal, or spindle-like morphology, in which they display increased motility, greater ECM assembly, and upregulated expression of inflammatory cytokines. Inflammatory cytokines expressed by malignant cells and cells that have undergone EMT also induce activation of local fibroblasts as we demonstrated in the previous chapter. Once activated, fibroblasts and epithelial cells that have undergone EMT play an integral role in reorganizing the surrounding ECM to the distinct architectures known as TACS, forming a positive feedback loop to further propagate fibroblast activation, epithelial cell transformation, and tumor progression. Since our ultimate goal was to investigate how cell response is altered between

isotropic (circular micropillars) and anisotropic (oval micropillars) substrates, we believe mimicking the overall chemotactic profile, rather than individual chemokines, of the TME would stimulate a more accurate cellular response to changes in mechanical properties of the environment.

Finally, we investigated the effect of downregulating force on cell morphology, ECM assembly, and alignment. We chose to use Y-27632 to test if downregulating force would ameliorate changes induced by 231CM treatment. Y-27632 was chosen because its effects have been extensively investigated and proven to downregulate force, as well as based on our findings of its efficacy on fibroblasts in Chapter 3. Y-27632 was added to 231CM-treated cells 90 minutes post seeding on micropillars. Overall, we investigated the effects of anisotropic stiffness on 10A, AT1, and 231 morphology, ECM assembly, force, and alignment, and we elucidated the effects of upregulating and downregulating force on mechanoresponse in a tumor progression model.

4.2 Methods

4.2.1 Fabrication of Oval Substrates, Circle Substrates, and Half-and-half substrates

All substrates were fabricated as described in 3.2.1.

4.2.2 Microfabricated Pillar Array preparation

Micropillar arrays were prepared as described in 3.2.2

4.2.3 Cell culture

We choose to use MCF10A, MCF10AT1, and MDA-MB-231 cell lines for this aim. These cell lines, often used in breast cancer research, represent cells at various stages of malignancy. MCF10As are widely regarded across literature as a model for normal mammary epithelial cells⁶². MCF10AT1 cells, HRAS transformed MCF10As, are classified as premalignant and form slow-progressing tumors in 25% of cases when implanted into mice⁶³. MDA-MB-231 are a highly invasive, triple negative (estrogen and progesterone receptor negative and lacking human epidermal growth factor receptor 2 (HER2) amplification), cell line previously demonstrated to migrate along EFG gradients and respond to variances in mechanical cues, such as stiffness and aligned topography^{6,64-66}.

Cells were prepared by seeding them in a 12 well plate at a density of 225,000 cells per well and culturing them in their respective standard media. For the 231CM treatment condition, in place of standard media, we used a 1:1 ratio of standard media to 231CM. Cells were cultured in 12 well plates for 48 hours, allowing 231CM treated cells to transform, before seeding on micropillars. Cells in the control condition were cultured on micropillars in standard media. Cells in the 231CM

and 231CM + Y-27632 groups were seeded in the same 1:1 ratio (standard : 231CM) media. 20 μ M Y-27632 was added to the 231CM + Y-27632 group 90 minutes after seeding.

Cells were seeded on fibronectin-coated micropillars at a density of 10,000 cells per sample in 2mL of media, which contain approximately 1cm² of micropillars, and allowed to incubate for 24 hours at 37C and 5% CO₂. Cells were permeabilized using 0.5% triton in 4% paraformaldehyde for 2 minutes and fixed in 4% paraformaldehyde for 20 minutes. Next, samples were rinsed with PBS 3 times and placed in a 0.1% BSA blocking solution for 5 minutes. Following the blocking step, 50-100 μ L of our primary antibody was placed on a sheet of parafilm in a 100mm petri dish. The 25mm coverslip was then flipped over and placed cell side down on top of the primary antibody droplet and incubated at 37C for 30 minutes. After being submerged in 0.1% BSA for another five minutes, the last step was repeated to apply the secondary antibody. The samples were immunofluorescence labeled for FN (Abcam rabbit anti FN ab2413), actin (Alexa Fluor 555 Phalloidin A34055), and the nucleus (NucBlue Fixed ReadyProbes R37606).

4.2.4 Statistical analysis

Statistical analysis was performed as previously described in 3.2.7. Three samples per condition were analyzed with total cell counts as follows. 10As on circular micropillars; control n = 47, 231CM n = 45, 231CM+Y-27632 n = 53. 10As on oval micropillars; control n = 49, 231CM n = 38, 231CM+Y-27632 n = 53. AT1s on circular micropillars; control n = 35, 231CM n = 50, 231CM+Y-27632 n = 44. AT1s on oval micropillars; control n = 32, 231CM n = 48, 231CM+Y-27632 n = 46. 231s on circular micropillars; control n = 49, Y-27632 n = 49. 231s on oval micropillars; control n = 50, Y-27632 n = 44.

4.3 Results

MCF10A Data

4.3.1 MCF10A Immunofluorescence analysis:

Initially, we assessed the phenotypic characteristics of 10As, our healthy epithelial cell line, on circular and oval micropillars by visual examination of immunofluorescence images. Across the following treatments: control, 231CM, and 231CM+ Y-27632, we assessed cell size, morphology, ECM assembly, force, and alignment. 10As in the control condition were cultured in standard media before and during the experiment. 10As in the 231CM group were treated with 231CM for 48 hours before seeding onto micropillars to allow time for inflammatory cytokines to initiate transformation. Cells were then lifted and seeded onto micropillars with continued 231CM treatment. Finally, we investigated the effect of downregulating force, via Y-27632, on epithelial cell mechanoresponse. Y-27632 was added 90 minutes after seeding to cells in the 231CM + Y-27632 group.

In Figure 27, we show representative images of 10As on circular micropillars in control, 231CM, and 231CM + Y-27632 treatment groups. Visual inspection of actin (first column) shows a significant increase in cell size when 10As are treated with 231CM. Treatment with Y-27632 leads to a disruption of this response, and cells display a rounded morphology. 10As in the control group assemble minimal FN, but, when treated with 231CM, cells display increased FN assembly. Cells in the 231CM + Y-27632 group maintain FN some assembly.

10As on oval micropillar display similar responses. In the control condition, 10As display small size with intracellular FN staining. Cells treated with 231CM show larger cell size as well

as a more elongated morphology, and the addition of Y-27632 negates this effect. 10As in all groups display minimal FN assembly. These images were next processed in MATLAB to assess these observations quantitatively.

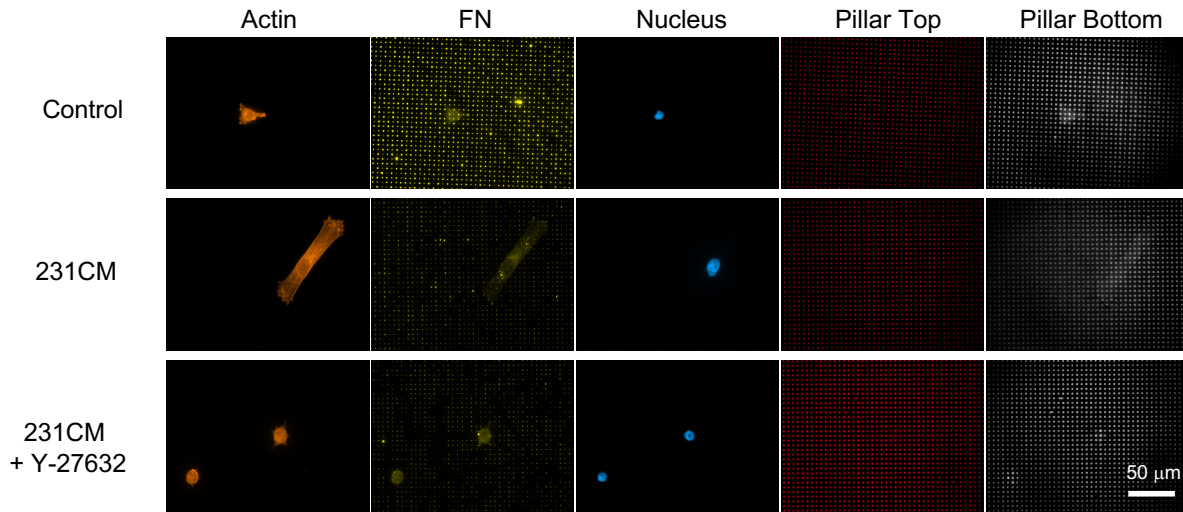


Figure 27: MCF10As on circular micropillars

Representative images of MCF10A cells seeded on circular cross section (isotropic) micropillars for 24 hours. Cells were stained for actin (orange), fibronectin (yellow), nucleus (blue), micropillar tops (red), and micropillar bottoms (white). Cells were cultured with 231CM for 48 hours prior to seeding on micropillars, with 231CM, for 24 hours. In the 231CM + Y-27632 group, Y-27632 was added 90 minutes after seeding. In the control condition (top row), 10As displayed small cell bodies and minimal FN assembly. Compared to the control condition, cells in the 231CM group (middle row) displayed larger cell size (visualized in the actin images) and greater FN assembly. When Y-27632 was added to the media, cells appeared rounded and minimally spread (bottom row). Y-27632 also decreased FN assembly. All images were taken on a Zeiss Axio Observer microscope using a 63x magnification oil objective. Scale bar represents 50 μ M.

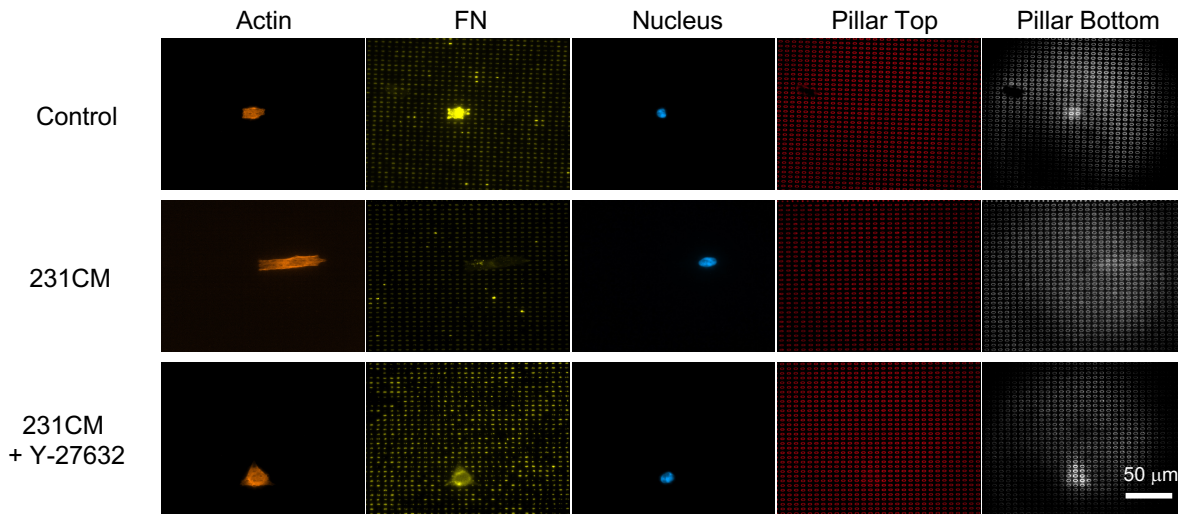


Figure 28: MCF10As on oval micropillars

Representative images of MCF10A cells seeded on oval cross section (anisotropic) micropillars for 24 hours. Cells were stained for actin (orange), fibronectin (yellow), nucleus (blue), micropillar tops (red), and micropillar bottoms (white). Cells were cultured with 231CM for 48 hours prior to seeding on micropillars with 231CM, for 24 hours. In the 231CM + Y-27632 group, Y-27632 was added 90 minutes after seeding. 10As in the control condition (top row) displayed small cell bodies and bright intracellular FN staining. When compared to the control condition, cells in the 231CM group (middle row) displayed larger cell size (visualized in the actin images) but decreased intracellular and assembled FN staining. When Y-27632 was added to the media, cells appeared more rounded and minimally spread. Cells treated with 231CM and Y-27632 (bottom row) also displayed greater intracellular FN staining than the 231CM group, but less than the control group. All images were taken on a Zeiss Axio Observer microscope using a 63x magnification oil objective. Scale bar represents 50 μ M.

4.3.2 10A MATLAB analysis of cell area, fibril area, and force:

Immunofluorescence images of MCF10As were analyzed in MATLAB. Quantification of cell area revealed that 231CM treatment significantly increased average cell area compared to the control on oval micropillars. Treatment with 231CM + Y-27632 resulted in smaller sizes than both control and 231CM conditions on circular micropillars (Figure 29A). On oval micropillars, 23CM + Y-27632 treatment significantly decreased cell area comparable to the control group (Figure 29B). However, when comparing between circular and oval micropillar groups, cells in all treatment conditions demonstrated no significant change in cell area, indicating that the chemotactic treatments are responsible for these changes, not the mechanical cues provided by oval micropillars (Figure 29C).

Next, we quantified FN assembly. On circular micropillars, 10As treated with either 231CM or 231CM + Y-27632 did not show any differences in FN assembly (Figure 30A). On oval micropillars, treatment with 231CM showed no increase in FN assembly, but treatment with 231CM + Y-27632 decreased FN area significantly from the control and 231CM groups (Figure 30B). Comparing between circular and oval micropillars (Figure 30C), 10As express no difference in fibril assembly in the control and 231CM conditions, however, 10As on oval micropillars assemble significantly less FN than those on circular micropillars in the 231CM + Y-27632 group.

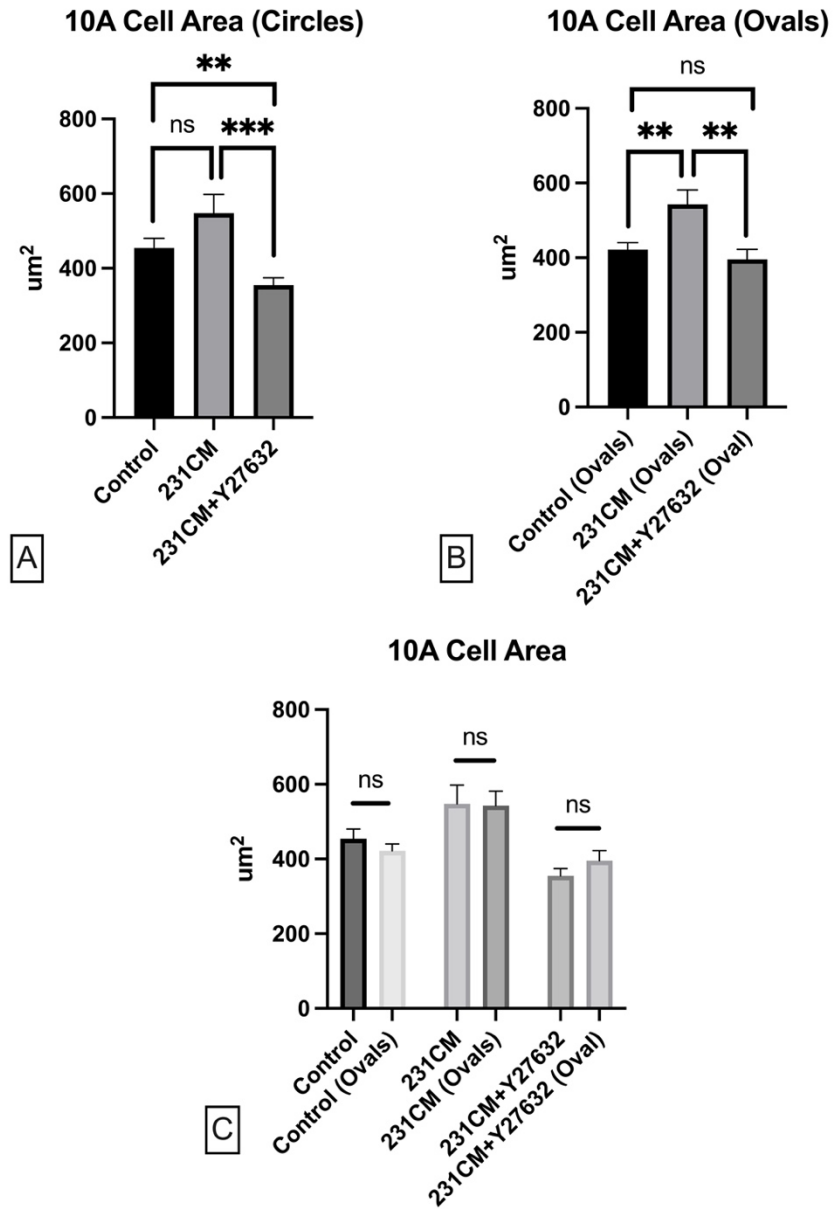


Figure 29: MCF-10A cell area

We quantified 10A cell area on circular (A) and oval (B) micropillars in control, 231CM, and 231CM + Y-27632 treatment conditions. On circular micropillars, treatment with 231CM resulted in no significant change from the control group. When treated with both 231CM and Y-27632, cells exhibited significantly lower cell area than both control and 231CM groups. On oval

micropillars, cells treated with 231CM showed significantly larger cell area than control and 231CM + Y-27632 groups. When comparing between circular and oval micropillar groups, 10As showed no significant difference in cell size across all treatment conditions.

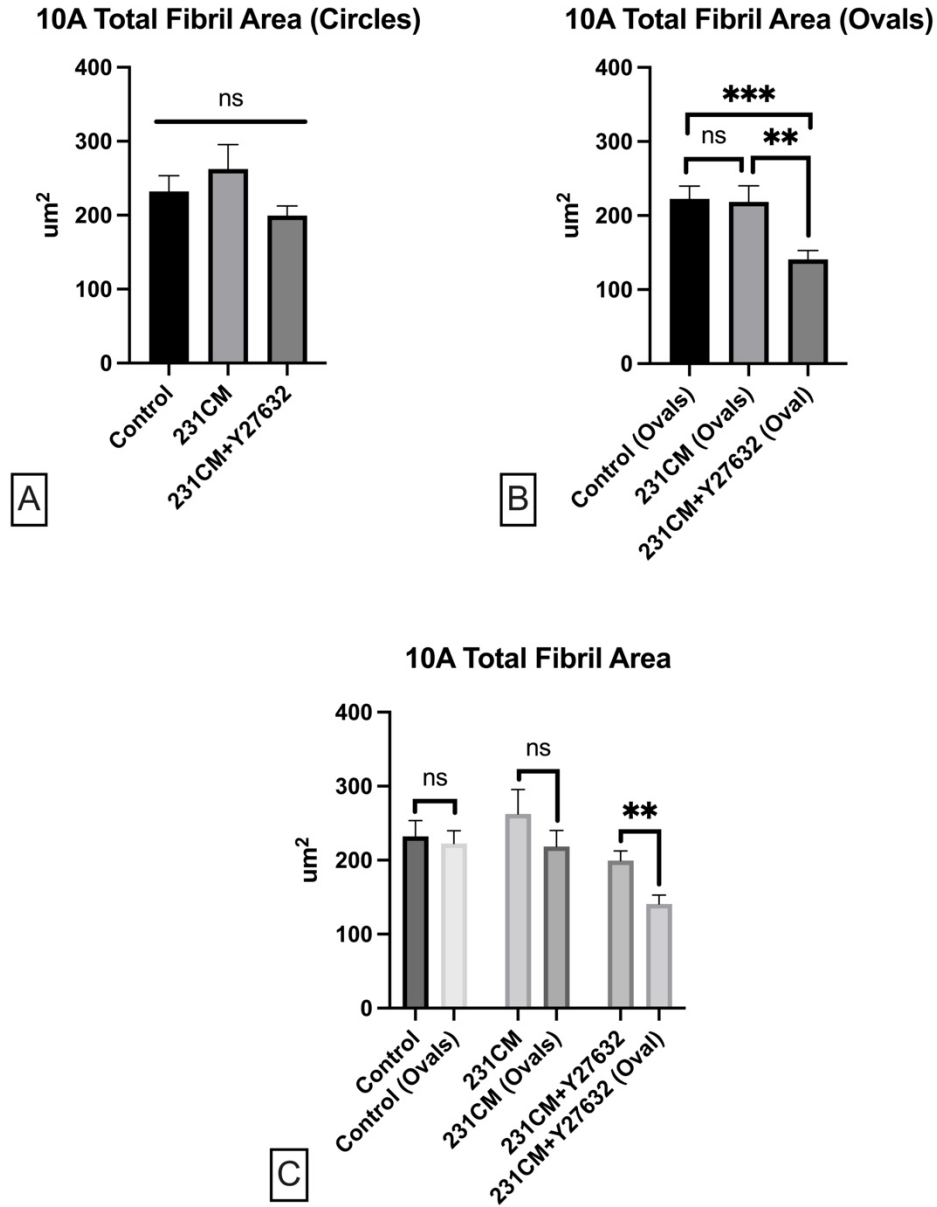


Figure 30: 10A Total fibril area quantification

Total FN assembly on circular and oval micropillars. 10A samples across control, 231CM, and 231MC + Y-27632 groups were analyzed. A) 10As on circular micropillars showed no significant difference in FN assembly when treated with 231CM or 231CM + Y-27632. B) Treatment with 231CM + Y-27632 resulted in significantly lower FN assembly compared to the control and

231CM conditions. C) Comparing between circular and oval substrates, the data show that cells in the 231CM + Y-27632 group assemble less FN on oval micropillars.

Analysis of 10A forces on circular micropillars (Figure 31) revealed cells in the control and 231CM conditions generate similar amounts of force, while treatment with Y-27632 reduces force significantly from both other groups. When averaged by the number of occupied pillars, cells in the 231CM + Y-27632 group generated significantly less force per pillar than the control group. Next, we normalized total force against cell area and found that cells display similar force per μm^2 across all conditions. These data indicate that some of the significant differences may be related to cell area, and none of the treatments change 10A force generation.

We then assessed 10A forces on oval micropillars (Figure 32) and found that, similar to the forces on circular micropillars, 10As in the 231CM + Y27632 group generated less force in all metrics. Notably, force per cell area was significantly less in the 231CM + Y27632 condition, indicating that 10As may be more responsive to Y-27632 treatment on the stiffer oval micropillars.

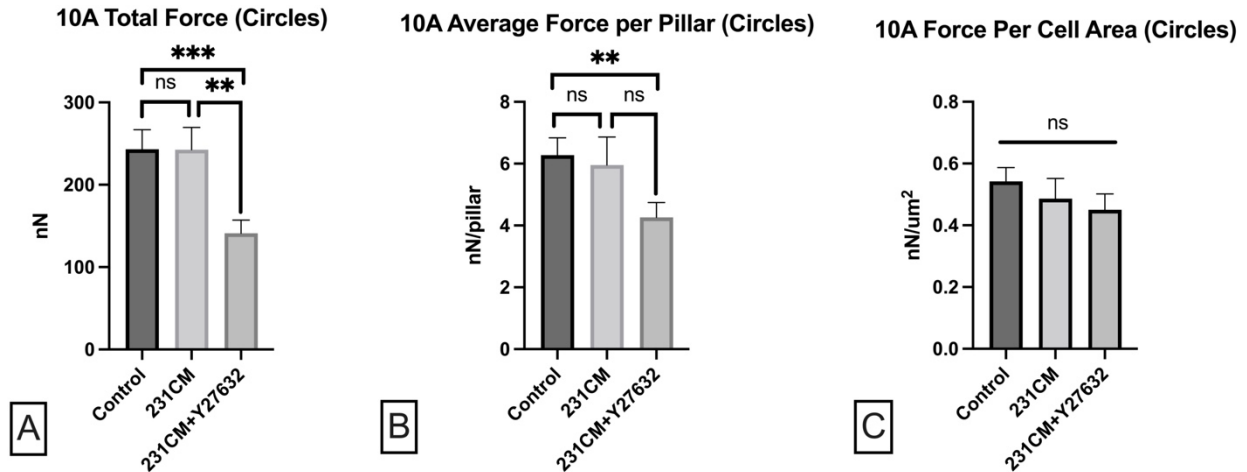


Figure 31: Quantification of 10A traction forces on circular micropillar substrates

We analyzed forces generated by 10As on circular micropillars and the resulting data is presented as total force, average force per pillar, and average force per square micron. A) While treatment with 231CM failed to show an increase in traction force, 231CM + Y-27632 treatment significantly decreased cell force on circular micropillars. B) Total force normalized against number of occupied micropillars. When normalized against micropillar count, the data once again shows that 231CM treatment did not increase force, but 231CM + Y27632 treatment significantly decreased force per pillar. C) When total force was normalized by cell area, the data show that there are no significant differences across all groups. These data tell us that force generation is correlated with cell size.

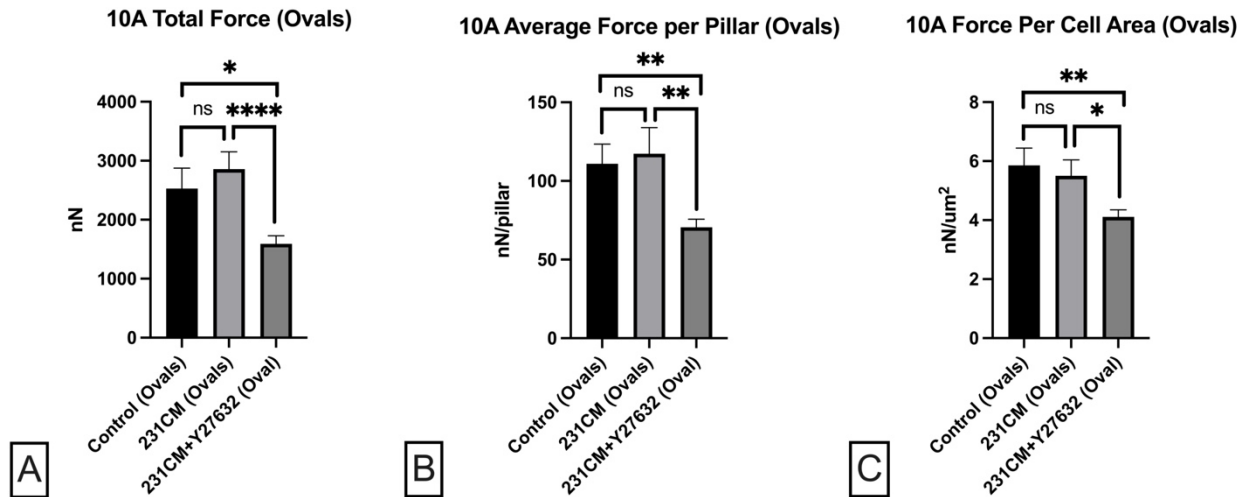


Figure 32: Quantification of 10A traction forces on oval micropillar substrates

10A forces quantified on oval micropillars in the following conditions: control, 231CM, and 231CM + Y-27632. In panel A, the data show that cells treated with 231CM + Y27632 display significantly less force when compared to control and 231CM groups. In panel B, the data was normalized by pillar count and yielded the same result. We then normalized total force against cell size and were able to demonstrate that treatment with 231CM + Y-27632 significantly decreased cell forces.

4.3.3 MCF10A alignment on circular and oval micropillars:

Finally, we assessed the alignment potential of MCF10As. Rose plots of 10A alignment on circular and oval micropillars are displayed in Figure 33 A & D. 10As in the control condition display randomized alignment on both circular and oval micropillar substrates. In Figure 33 B & E, 10As treated with 231CM show increased alignment on oval micropillars. In Figure 33 C & F, cells in the 231CM + Y-27632 group display a slight increase in alignment. Statistical analysis of average orientation is presented in Figure 34. In panel A, 10As on circular micropillars display randomized alignment across all groups. When seeded on oval micropillars (panel B), we see a marked increase in alignment when treated with 231CM, and this response is attenuated by the addition of Y-27632. Panel C shows a comparison of the three oval groups to the control group on circular micropillars. It supports the data in panel B and demonstrates that 231CM treatment increases 10A mechanoresponse and alignment ability, while treatment with Y-27632 restores random cell alignment.

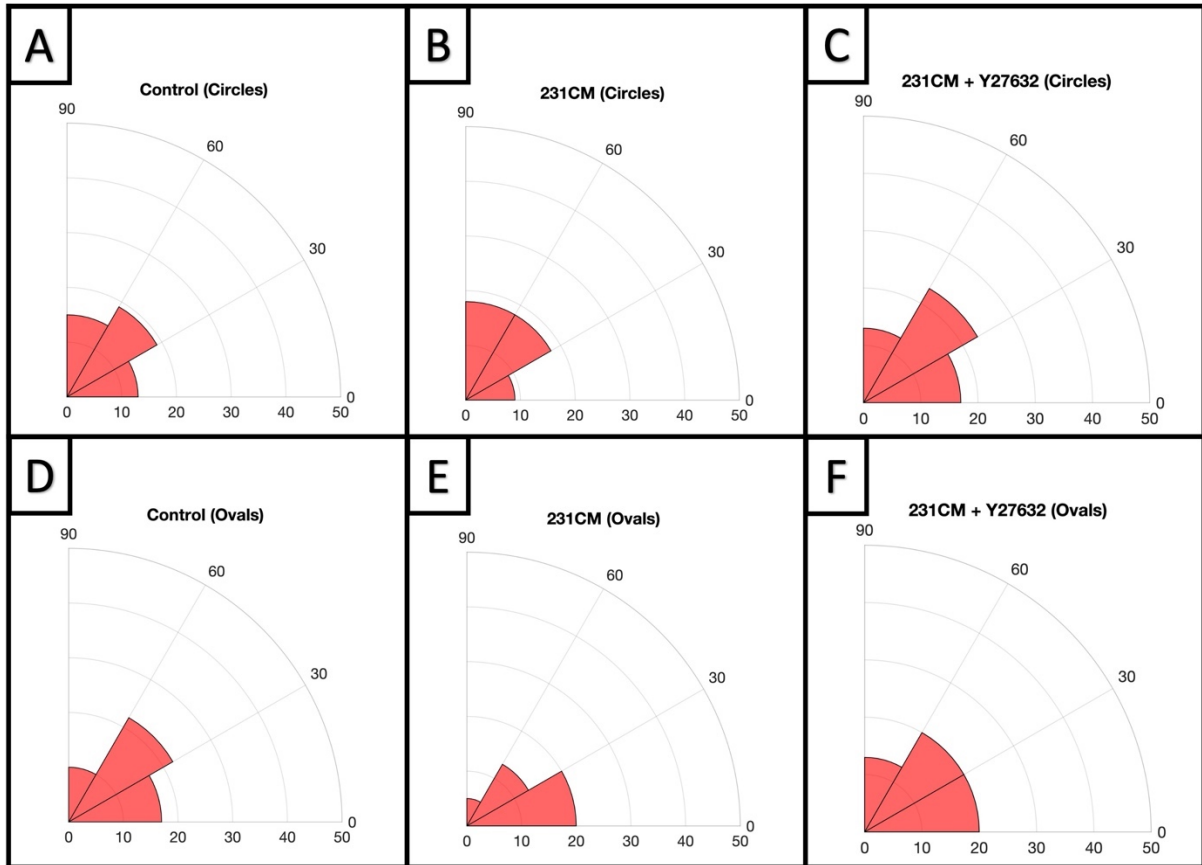


Figure 33: Rose plots of 10A alignment

We collected data on 10A orientations on circular (top row) and oval (bottom row) micropillars and assessed the effect of treatment with 231CM and 231CM + Y-27632. Rose plots of the control condition (A & D) show random cell alignment on both circular and oval micropillars. Treatment with 231CM resulted in improved cell alignment (E) and treatment with 231CM + Y-27632 (F) mitigates this response.

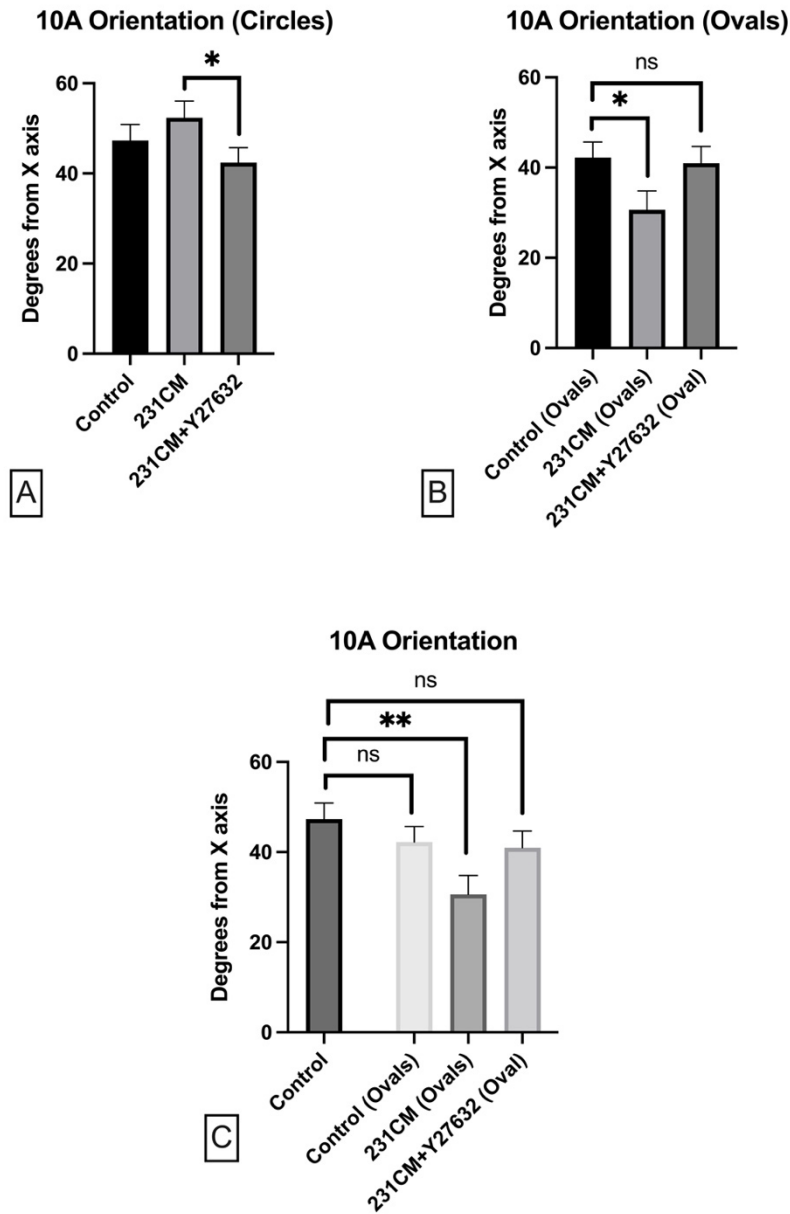


Figure 34: Quantification of 10A orientation on circular and oval micropillar substrates

Average cell orientation angle quantified on circular and oval micropillars across control, 231CM, and 231CM + Y-27632 treatment conditions. A) 10As display randomized alignment on circular micropillars signified by high orientation angles in all three groups. B) 10As on oval micropillars show a marked decrease in orientation angle (enhanced alignment) when treated with 231CM. This enhanced response is abrogated with the addition of Y-27632. C) Compared to the random

alignment displayed by control 10As on circular micropillars, the data show once again that only cells in the 231CM treatment group display a significant increase in alignment capability.

MCF10AT1 DATA

4.3.4 MCF10AT1 Immunofluorescence analysis:

Similar to the assessment of the MCF10As, we began with visual analysis of the immunofluorescence images of MCF10AT1s, our premalignant epithelial cell line, seeded on circular micropillars for 24 hours. AT1 experiments were conducted using the same preparation and treatment protocols as 10A experiments. Representative images of AT1s on circular micropillars in control, 231CM, and 231CM + Y-27632 treatment groups are shown in Figure 35. AT1s show similar changes in morphology and behavior to 10As in response to 231CM and 231CM + Y-27632 treatments. When treated with 231CM, AT1s significantly increase in cell size and adopt a spindle like morphology. Treatment with Y-27632 leads to a disruption of this response, and cells return to a rounded morphology. AT1s in the control group assemble minimal FN fibrils but show some intracellular FN staining. When treated with 231CM, cells display increased FN assembly. Conversely, cells in the 231CM + Y-27632 group exhibit no fibril assembly and less intracellular FN staining than cells in the control group. On oval micropillars (Figure 36), AT1s spread to a larger cell area when treated with 231CM, but still show minimal FN assembly. The addition of Y-27632 reverses the increase in cell size and results in morphology similar to the control. AT1s in all groups display limited FN assembly. These images were next processed in MATLAB to assess these observations quantitatively.

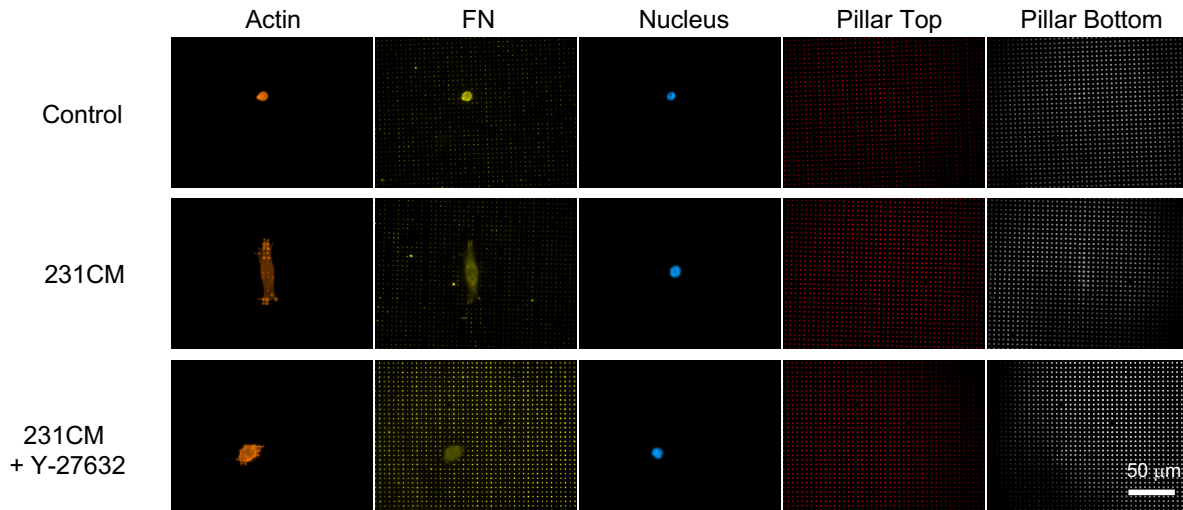


Figure 35: MCF10AT1s on circular micropillars

Representative images of MCF10AT1 cells seeded on circular cross section (isotropic) micropillars for 24 hours. Cells were stained for Actin (orange), fibronectin (yellow), nucleus (blue), micropillar tops (red), and micropillar bottoms (white). In the control condition (top row), AT1s displayed small cell bodies and minimal FN assembly, but bright intracellular FN staining. Compared to the control condition, cells in the 231CM group (middle row) displayed larger cell size (visualized in the actin images) and greater FN assembly. When Y-27632 was added to the media, cells appeared smaller, slightly rounded and minimally spread (bottom row). Treatment with Y-27632 also decreased FN assembly. All images were taken on a Zeiss Axio Observer microscope using a 63x magnification oil objective. Scale bar represents 50 μM .

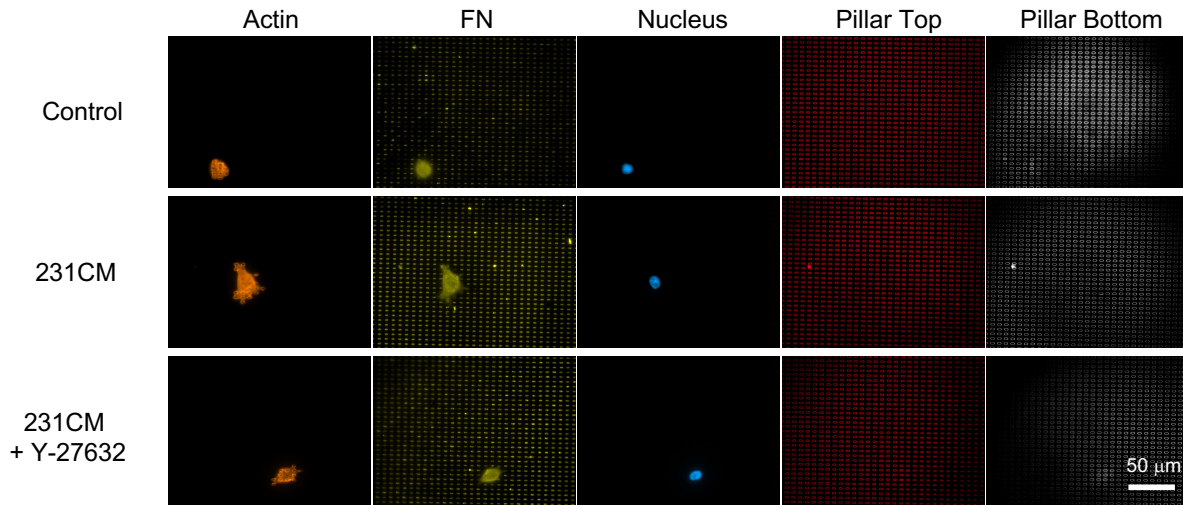


Figure 36: MCF10AT1s on oval micropillars

Representative images of MCF10AT1 cells seeded on oval cross section (anisotropic) micropillars for 24 hours. Cells were stained for Actin (orange), fibronectin (yellow), nucleus (blue), micropillar tops (red), and micropillar bottoms (white). In the control condition (top row), AT1s displayed small cell bodies and minimal FN assembly, but bright intracellular FN staining. Compared to the control condition, cells in the 231CM group (middle row) displayed larger cell size and minimal FN assembly. When Y-27632 was added to the media, cells appeared smaller, slightly rounded, and minimally spread (bottom row). Treatment with Y-27632 also decreased FN assembly. All images were taken on a Zeiss Axio Observer microscope using a 63x magnification oil objective. Scale bar represents 50 μ M.

4.3.5 MCF10AT1 MATLAB analysis of cell area, fibril area, force, and orientation:

Immunofluorescence images of MCF10AT1s were analyzed in MATLAB. Quantification of cell area revealed that cells in both 231CM and 231CM + Y-27632 treatment groups displayed significantly larger average cell area compared to the control on both circular and oval micropillars. This indicates that 231CM treatment stimulates AT1s to spread more, and that Y-27632 is unable to block this response (Figure 37 A & B). Comparison between circular and oval micropillar groups reveal no significant differences in cell size across all conditions (Figure 37C), indicating that AT1s may not sense and respond to mechanical cues provided by oval micropillars. This response is conserved between 10As and AT1s.

Next, we quantified FN assembly. AT1s displayed no significant changes in FN assembly between control, 231CM, and 231CM + Y-27632 groups on both circular and oval micropillars. AT1s display similar FN assembly characteristics on both circular and oval micropillars. With respect to FN assembly, neither chemotactic treatment nor varied mechanical cues perturbed response (Figure 38).

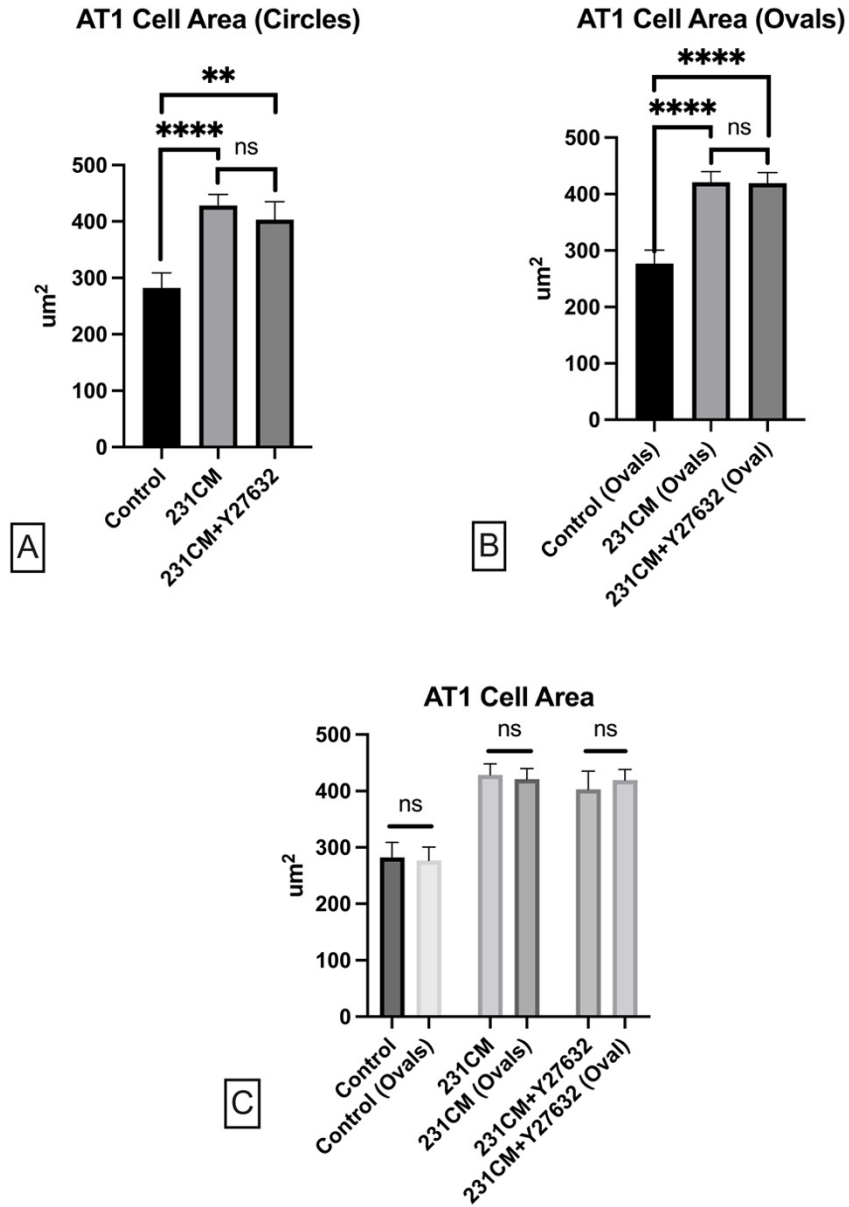


Figure 37: MCF10AT1 cell area

We quantified AT1 cell area on circular (A) and oval (B) micropillars in control, 231CM, and 231CM + Y-27632 treatment conditions. On circular micropillars, treatment with 231CM significantly increased cell area, but the addition of Y-27632 caused no significant change. On oval micropillars, the data present similar results. Treatment with 231CM significantly increased cell area and the addition of Y-27632 showed no change from the 231CM group. When comparing

between circular and oval micropillar groups, AT1s showed no significant difference in cell size across all treatment conditions. This indicates that AT1s respond similarly to 231CM and 231CM + Y-27632 treatments regardless of the underlying substrate.

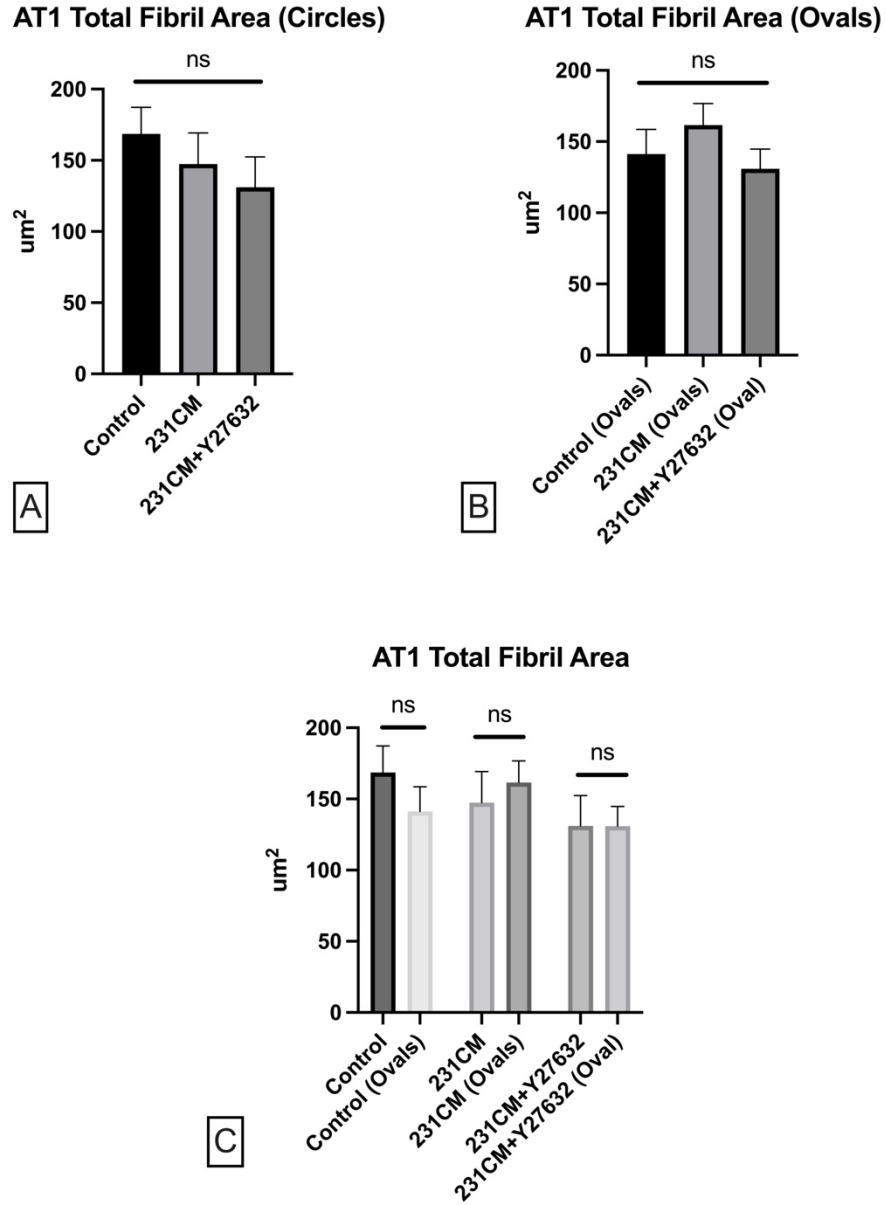


Figure 38: MCF10AT1 Total fibril area quantification

We quantified total FN assembly on circular and oval micropillars. AT1 samples across the control, 231CM, and 231MC + Y-27632 groups were analyzed. A) 10As on circular micropillars showed no significant difference in FN assembly when treated with either 231CM or 231CM + Y-27632. B) AT1s on oval micropillars showed no significant changes in FN assembly across all

treatments. C) Comparing between circular and oval substrates the data show that AT1s assemble a similar amount of FN on both substrates.

We proceeded to analyze AT1 forces on circular and oval micropillars. On circular micropillars (Figure 39), AT1s display larger total force when treated with 231CM and 231CM + Y-27632. Normalizing this data against number of occupied micropillars and cell area reveal no significant difference between the treatment groups. From this, we conclude that AT1 total force is dependent on cell size, but actual force generation ability is unchanged by treatment with 231CM or 231CM + Y-27632. On oval micropillars, AT1s show no significant differences in total force, force per pillar, and force per μm^2 (Figure 40).

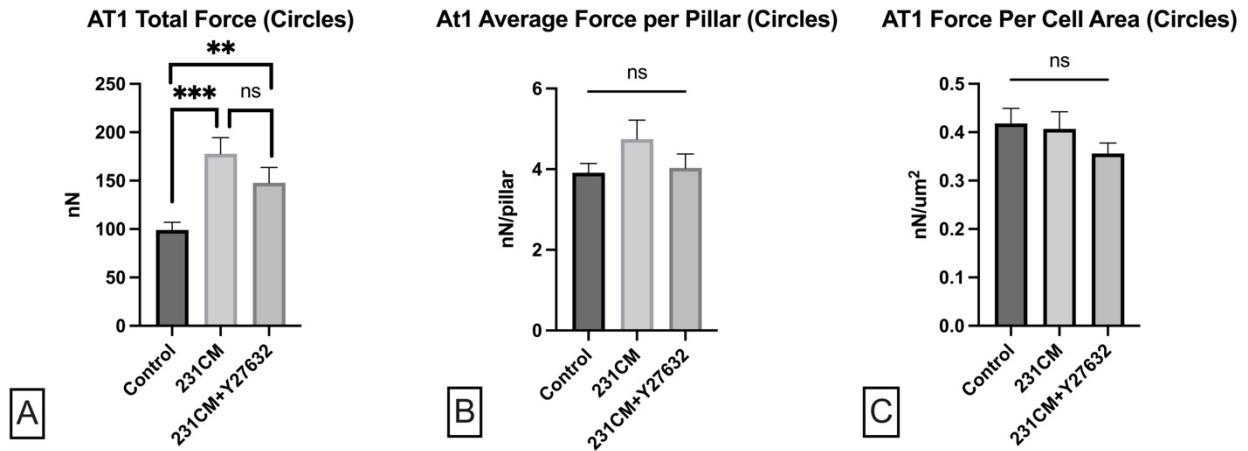


Figure 39: Quantification of AT1 traction forces on circular micropillar substrates

We analyzed traction forces from AT1s on circular micropillars and quantified the following metrics: total force (A), average force per pillar (B), and average force per μm^2 (C). Treatment with 231CM and 231CM + Y-27632 groups showed a significant increase in total force, indicating that Y-27632 treatment failed to decrease force. When normalized by number of occupied micropillars (B), AT1s showed no significant differences across all conditions. C) We normalized total force by average cell area. The data show no significant difference across all treatment groups. In summary, the increases in total force are a result of the larger cell areas in the 231CM and 231CM + Y-27632 groups, and not due to an actual increase in the cells capacity to generate larger forces.

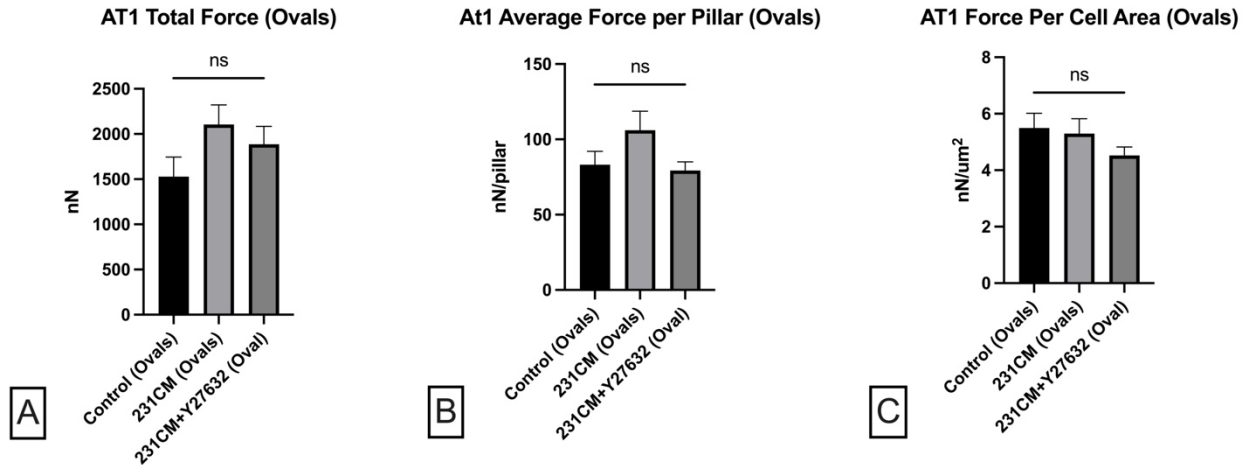


Figure 40: Quantification of AT1 traction forces on oval micropillar substrates

AT1 traction forces on oval micropillars were analyzed for total force (A), average force per pillar (B), and average force per μm^2 (C). A) AT1s showed no significant changes in total cell force when treated with 231CM or 231CM + Y-27632. Total force normalized against number of occupied pillars (B) and cell area (C) also did not show any significant differences between all treatment conditions. Overall, both 231CM and 231CM + Y-27632 treatments did not upregulate or downregulate force in AT1s on oval micropillars.

4.3.6 MCF10AT1 alignment on circular and oval micropillars:

Lastly, we assessed MCF10AT1 alignment on circular and oval micropillars. Rose plots of AT1 alignment on circular and oval micropillars are displayed in (Figure 41). A & D) AT1s demonstrate no significant alignment on oval micropillars across control (A & D), 231CM (B & E), and 231CM + Y-27632 (C & F) conditions. Statistical analysis of average orientation is presented in (Figure 42). All of the data indicate random cell orientation on both circular and oval micropillar substrates from this we can conclude that AT1s do not align along anisotropic stiffness substrates (oval micropillars) and upregulation or downregulation changes this response.

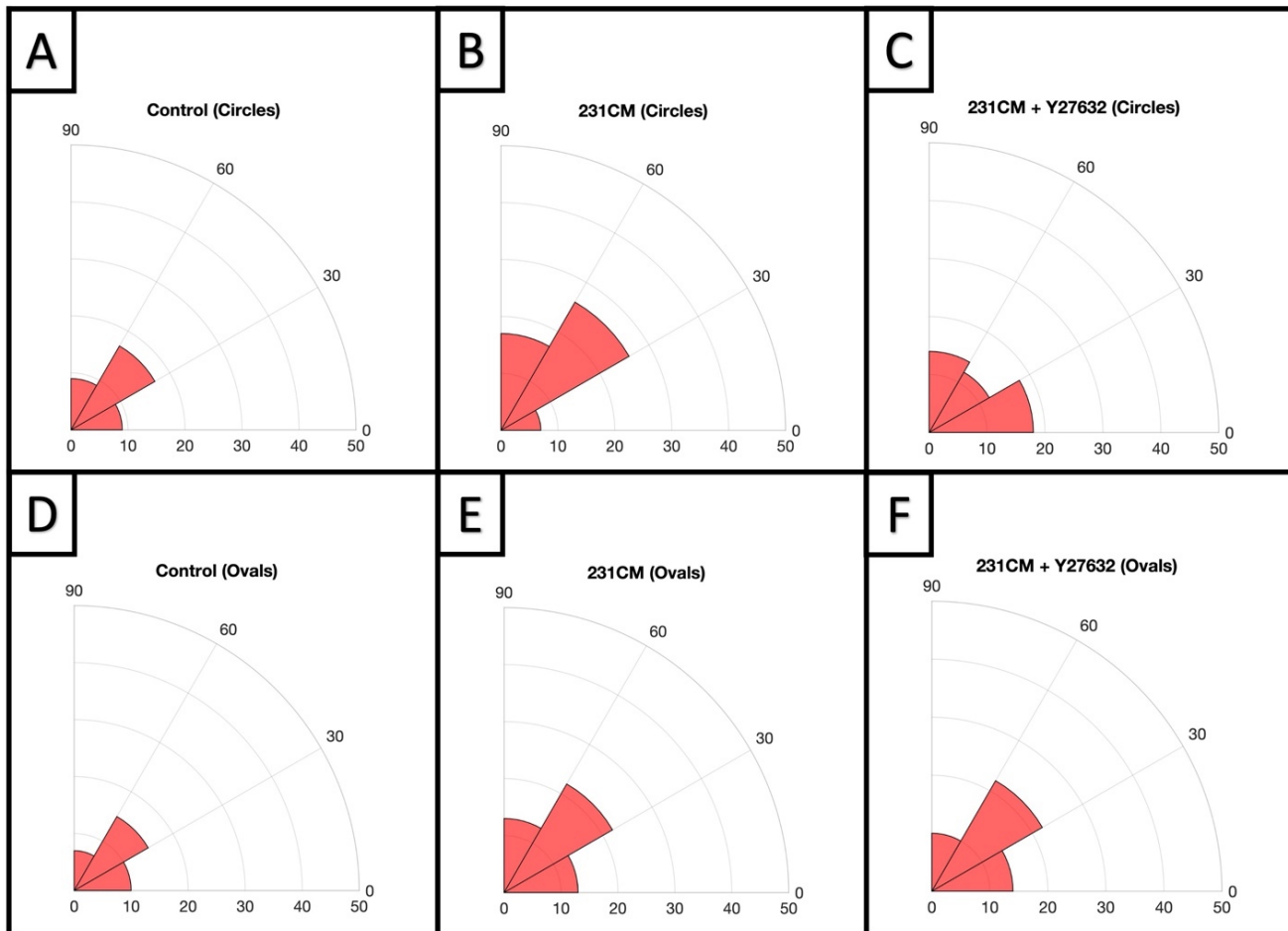


Figure 41: Rose plots of AT1 alignment

Quantification of AT1 orientation on circular (top row) and oval (bottom row) micropillars. AT1s in the control group (A & D) showed no difference in alignment between circular and oval micropillar substrates. Treatment with either 231CM (E) or 231CM + Y-27632 (F) did not influence AT1 alignment on oval micropillars.

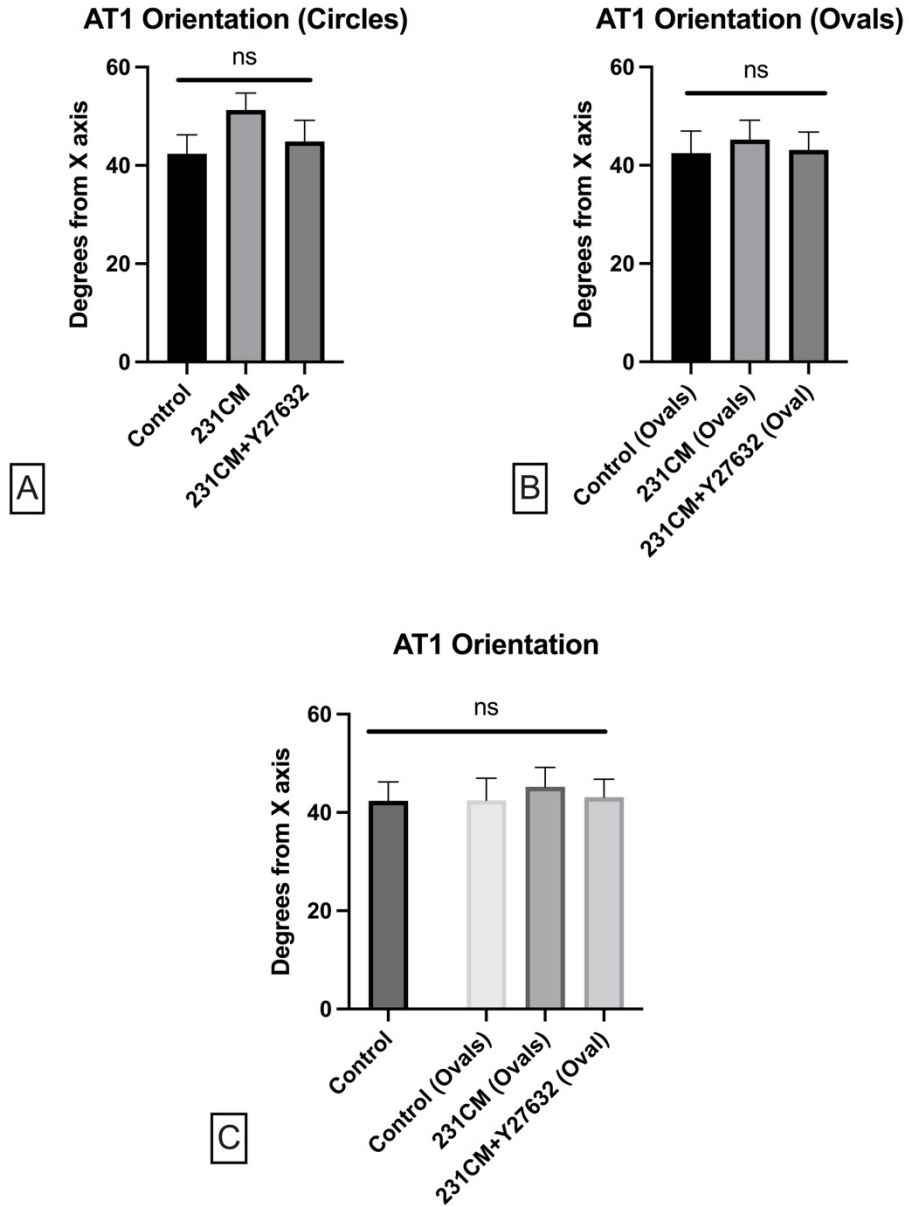


Figure 42: AT1 alignment quantified on circular and oval micropillars

Orientation was analyzed on circular (A) and oval (B) micropillars. AT1s on circular micropillars (A) demonstrated random alignment in all conditions. B) On oval micropillars, neither 231CM nor 231CM + Y-27632 treatment induced a change in alignment. When comparing oval micropillars to the control on circular micropillars, the data show no significant increase in

alignment in any of the conditions. The data indicate that AT1s do not align to the major axis of oval micropillars in response to anisotropic stiffness and contact guidance.

MDA-MB-231 DATA

4.3.7 MDA-MB-231 immunofluorescence image analysis:

Once again, we began by visually examining morphology and FN fibril assembly of 231s, our metastatic cell line. 231 samples were stained for actin (orange), fibronectin (yellow), nucleus (blue), micropillar tops (red), and micropillar bottoms (white). Representative images are presented in Figure 43 and Figure 44. 231s in the control condition, on circular micropillars, display small, rounded cell bodies with small filopodial extensions to peripheral micropillars. When treated with Y-27632, 231s display larger and more elongated cell bodies. Both groups display minimal FN fibril assembly and some intracellular FN expression. In the control condition, 231s on oval micropillars have small cell bodies and minimal FN assembly. When treated with Y-27632, 231s display much larger cell size, elongated morphology, and maintain minimal FN assembly.

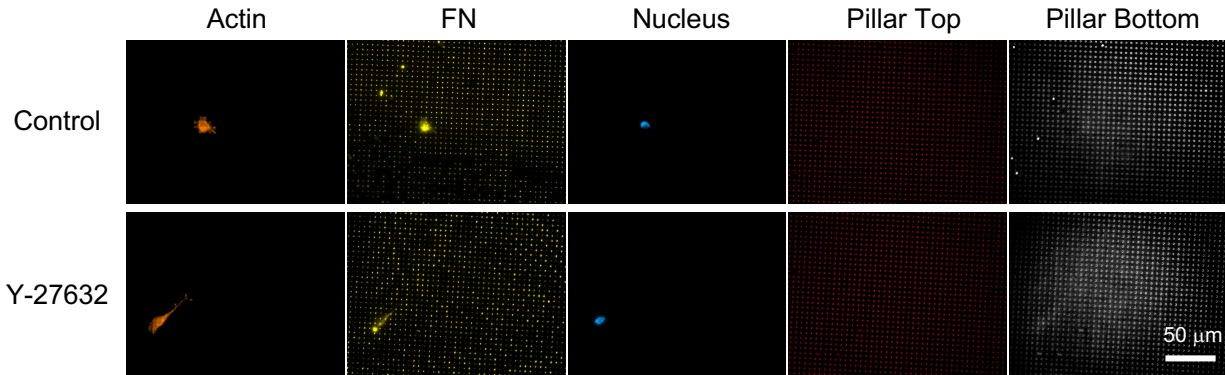


Figure 43: MDA-MB-231s on circular micropillars

Representative images of MDA-MB-231 cells seeded on circular cross section (isotropic) micropillars for 24 hours. Cells were stained for Actin (orange), fibronectin (yellow), nucleus (blue), micropillar tops (red), and micropillar bottoms (white). In the control condition (top row), 231s displayed small cell bodies with small filopodial extensions, minimal FN assembly and bright intracellular FN expression. When treated with Y-27632, cells appeared larger, more elongated, and displayed minimal FN assembly (bottom row). All images were taken on a Zeiss Axio Observer microscope using a 63x magnification oil objective. Scale bar represents 50 μM .

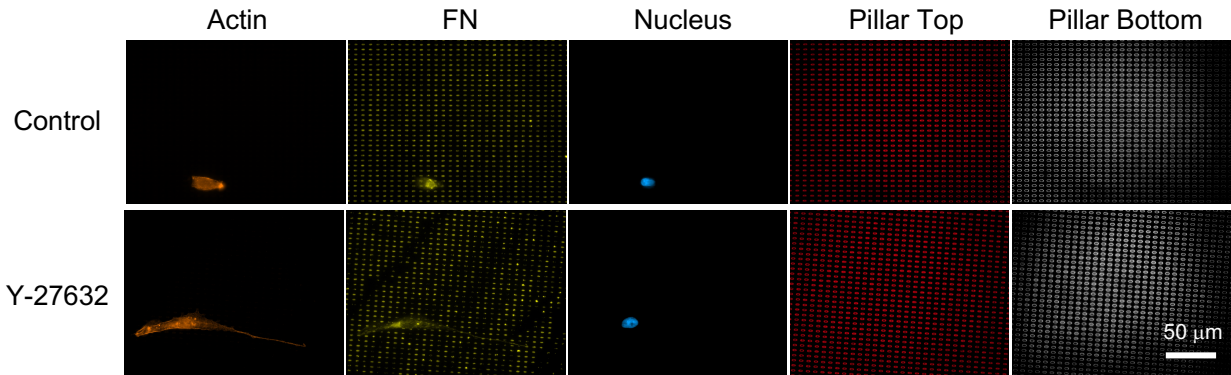


Figure 44: MDA-MB-231s on oval micropillars

Representative images of MDA-MB-231 cells seeded on oval cross section (isotropic) micropillars for 24 hours. Cells were stained for Actin (orange), fibronectin (yellow), nucleus (blue), micropillar tops (red), and micropillar bottoms (white). In the control condition (top row), 231s displayed small cell bodies and minimal FN assembly. When treated with Y-27632, cells appeared much larger, more elongated, and still displayed minimal FN assembly (bottom row). Cells in both control and Y-27632 groups exhibited alignment along the major axis of oval micropillars. All images were taken on a Zeiss Axio Observer microscope using a 63x magnification oil objective. Scale bar represents 50 μ M.

4.3.8 MATLAB analysis of MDA-MB-231 cell area, fibril area, and force:

As with previous cell lines, for 231s, we initially assessed the differences in cell area on circular and oval micropillars. Cell areas were quantified and are presented in Figure 45. In panel A, we see that there is no significant difference in cell size between control and Y-27632 conditions on circular micropillars. On oval micropillars (panel B), contrary to our initial presumptions, the data show that 231s have a significantly larger cell area when treated with Y-27632. Comparing between circular and oval micropillar substrates (panel C), we see that there is no significant difference in cell size in the control condition. However, when treated with Y-27632, cells on oval micropillars are significantly larger than Y-27632 treated cells on circular micropillars.

Next, we assessed total fibril area (Figure 46) and are able to see that while Y-27632 does not alter FN assembly on circular micropillars, it significantly downregulates FN assembly on oval micropillars. We also note significantly less FN assembly by 231s treated with Y-27632 on oval micropillars compared to their counterparts on circular micropillars. This indicates that Y-27632 has a greater effect on 231 FN assembly on the stiffer, oval micropillars.

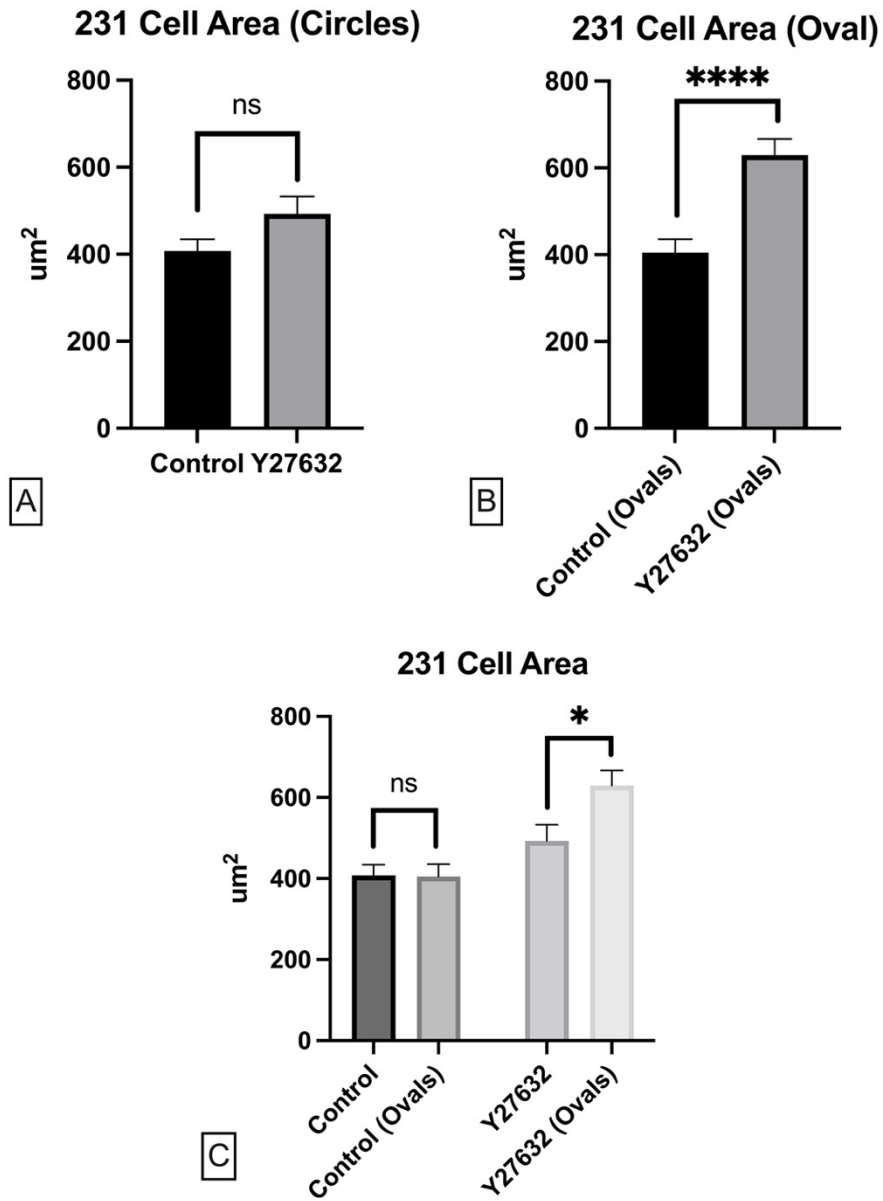


Figure 45: 231 Cell area on circular and oval micropillars

Average cell area of 231s on circular and oval micropillars when not treated (control) or treated with Y-27632. A) 231s on circular micropillars showed no significant change in cell area when treated with Y-27632. B) On oval micropillars, treatment with Y-27632 significantly increased cell area. C) Comparison of cell area between circular and oval micropillars. 231s showed no difference in size in the control condition but showed a significant increase in cell size when

treated with Y-27632 on oval micropillars. The data demonstrate that 231s are more responsive to Y-27632 treatment on oval micropillars.

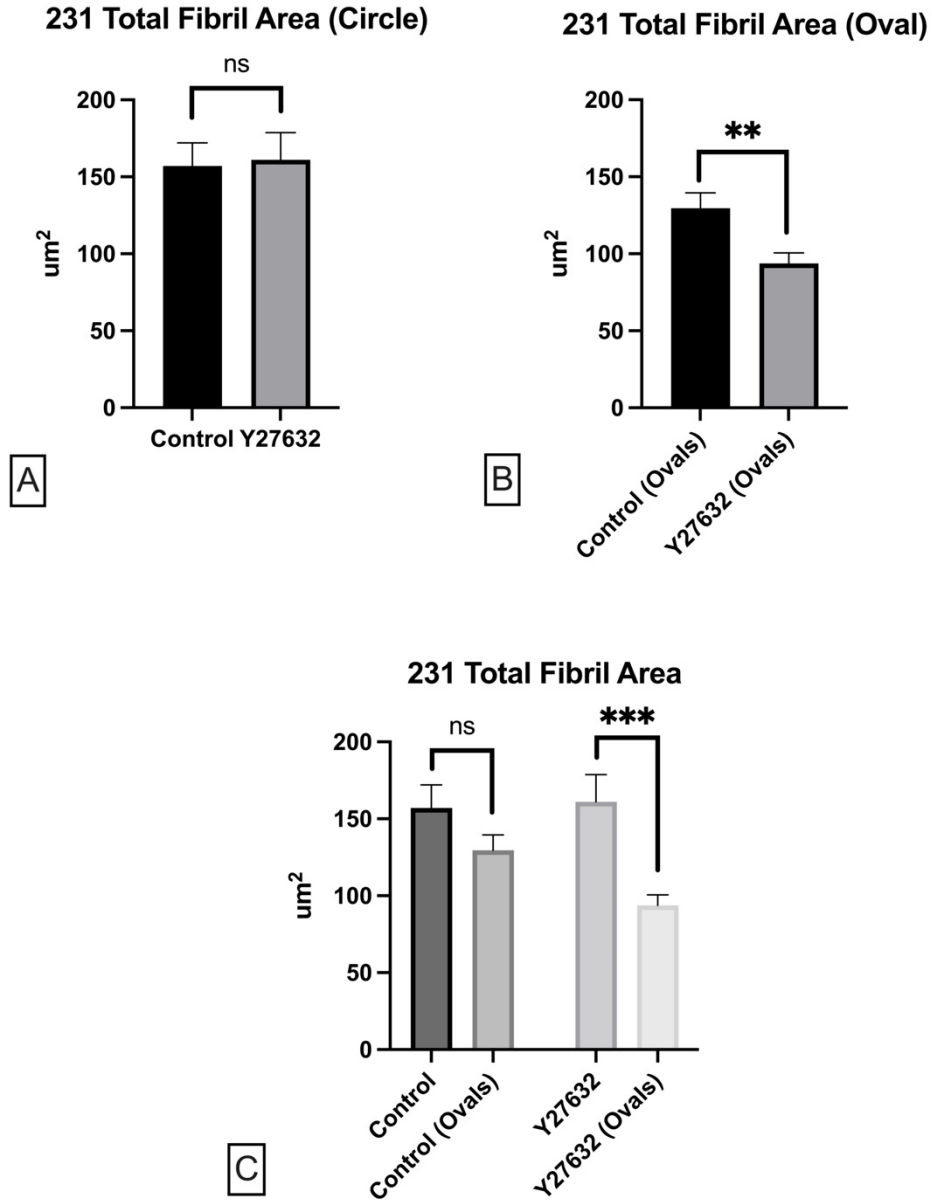


Figure 46: Quantification of 231 FN assembly on circular and oval micropillars

Total FN fibril area was assessed in 231s on circular and oval micropillars. A) 231s on circular micropillars showed no change in FN assembly when treated with Y-27632. B) On oval micropillars, inhibiting force with Y-27632 resulted in decreased FN assembly. C) Comparison

between circular and oval micropillar data revealed no statistical difference in the control groups but, shows significant decrease in fibril area between the Y-27632 groups.

Next, we analyzed MDA-MB-231 forces on circular and oval micropillars. On circular micropillars, 231s treated with Y-27632 generate higher total force. When the data was normalized against number of occupied pillars, it yielded no significant differences, indicating no true changes in force production capability. On oval micropillars, we see the same result. Cells treated with Y-27632 demonstrate higher total force but, once again, this difference isn't conserved when total force is normalized against occupied pillars or cell area.

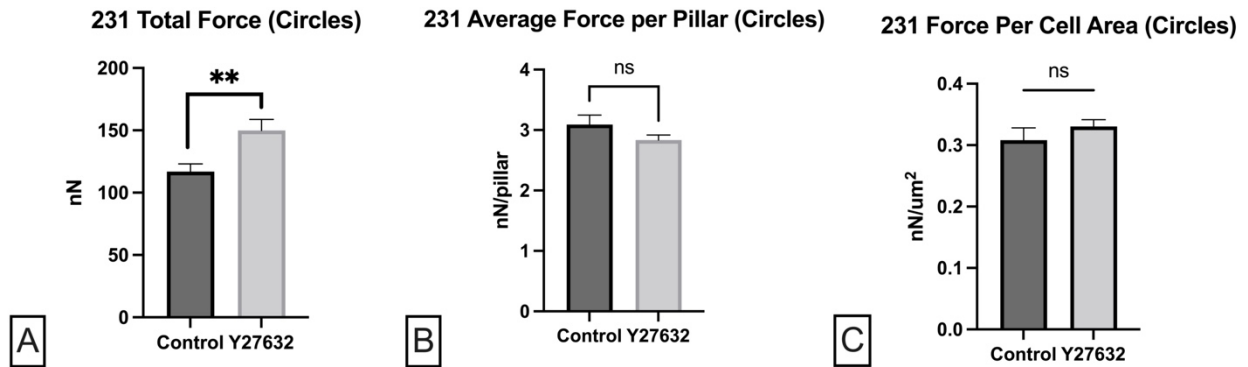


Figure 47: Analysis of 231 forces on circular micropillars

Force characteristics were assessed on circular micropillars when 231s were left untreated (control) or treated with Y-27632. A) 231s treated with 231CM display increased total force compared to the control. B) When normalized by the number of occupied pillars, there is no significant difference in force. C) Normalization by cell area similarly shows no difference in force between control and Y-27632 groups. The data indicate that the increase in total force is correlated with increased cell area.

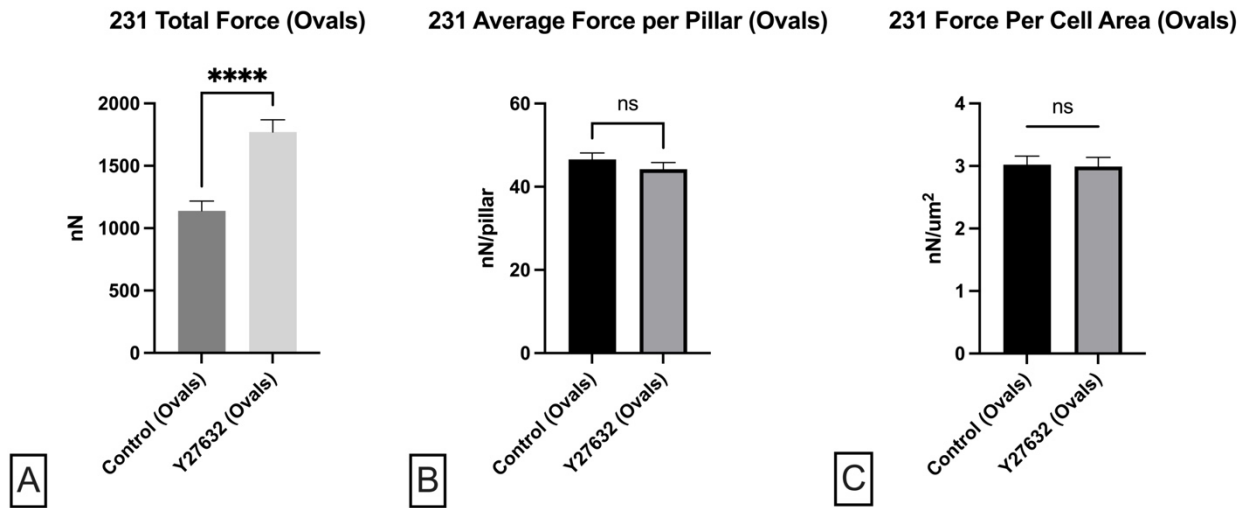


Figure 48: Analysis of 231 forces on oval micropillars

Force characteristics were assessed on oval micropillars when 231s were left untreated (control) or treated with Y-27632. A) 231s treated with 231CM display increased total force compared to the control. B) When normalized by the number of occupied pillars there is no significant difference in force. C) Normalization by cell area similarly shows no difference in force between control and Y-27632 groups. The data indicate that the increase in total force is correlated with increased overall cell area.

4.3.9 MDA-MB-231 alignment on circular and oval micropillars:

Finally, we assessed 231 alignment on circular and oval micropillars. The rose plots in figure 49 indicate a slight increase in cell alignment on oval micropillars in both control (A & C) and Y-27632 (B & D) groups. This observation was not supported when the data was analyzed for statistical significance. The plots in Figure 50 clearly show that 231s do not exhibit significant alignment on oval micropillars.

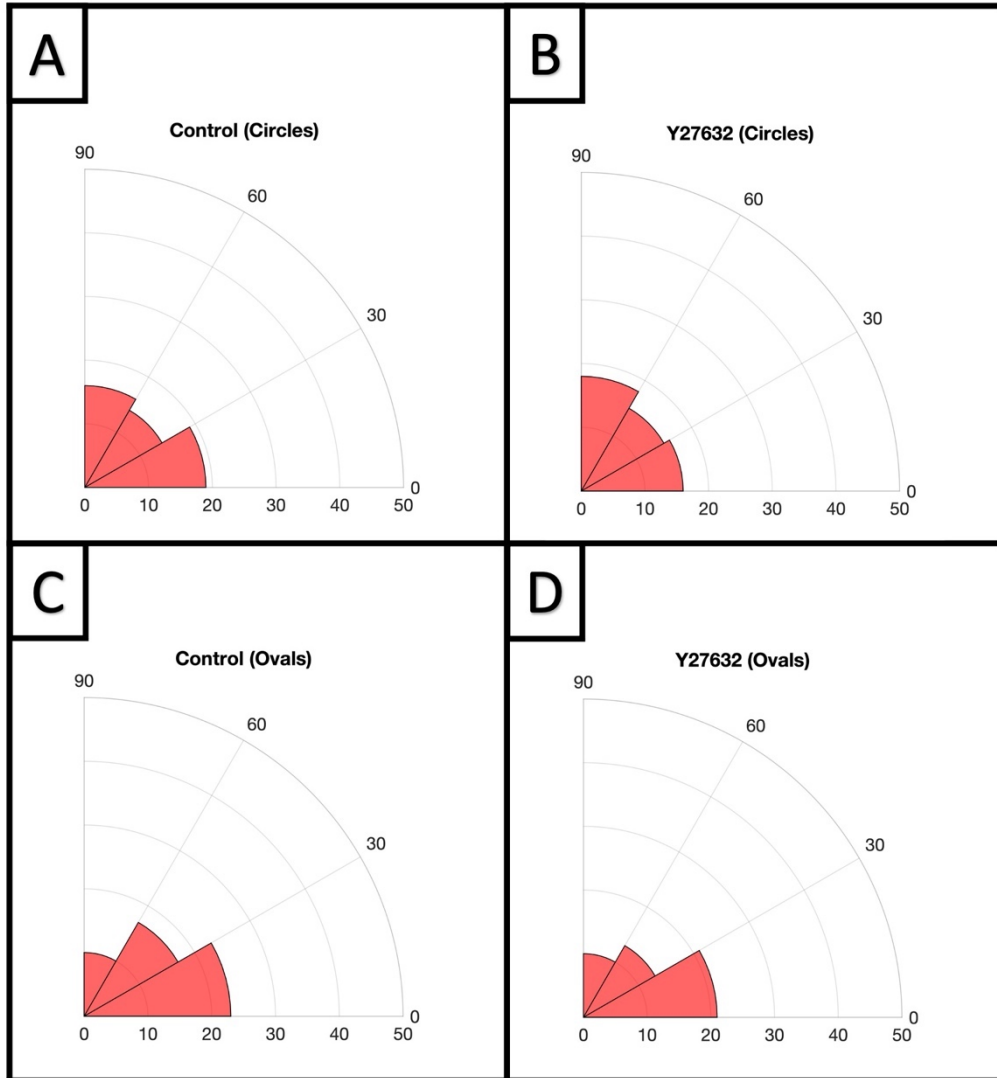


Figure 49: Rose plots of 231 orientation on circular and oval micropillars

Cell orientation was assessed between 231s on circular and oval micropillars. Visual analysis of rose plots of the control groups (A & C) indicate a slight increase in alignment on oval micropillars.

231s treated with Y-27632 on oval micropillars (D) also display a slight increase in alignment.

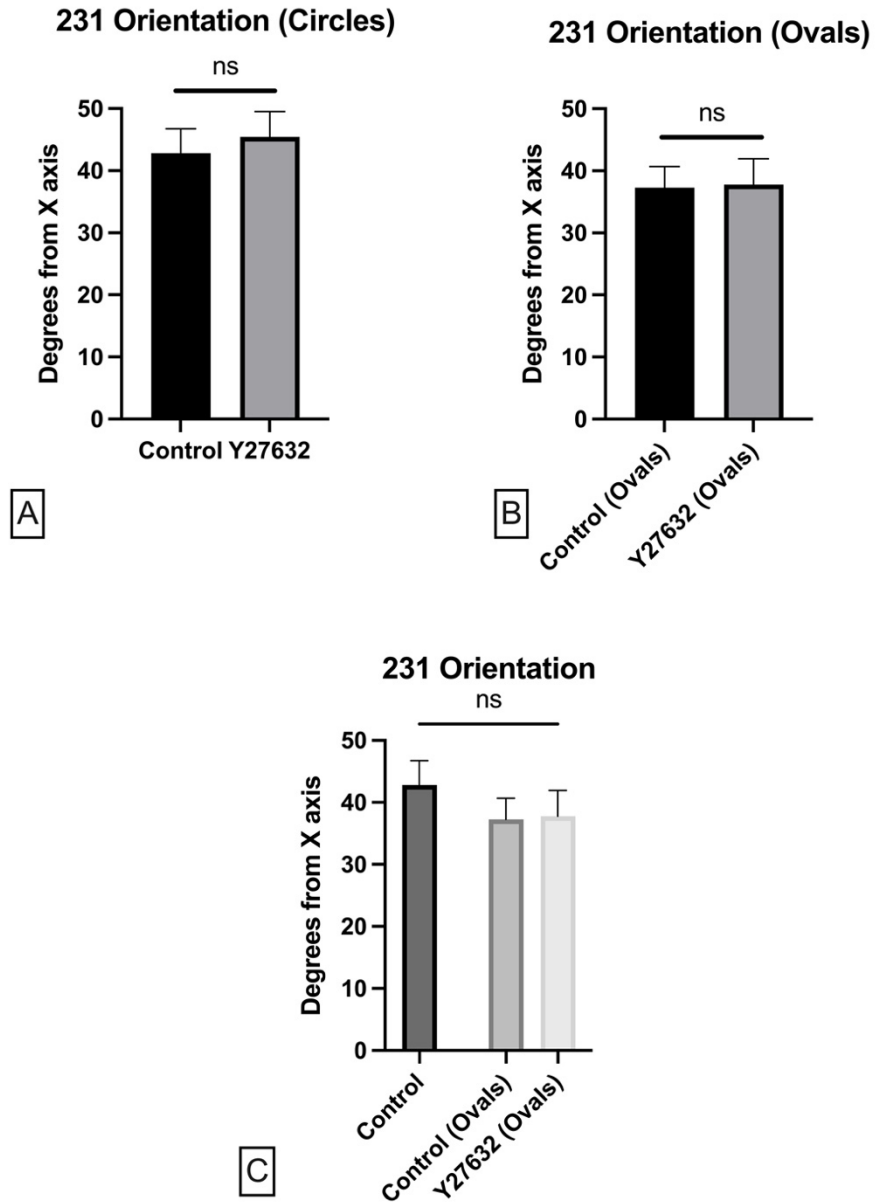


Figure 50: 231 orientation quantification analysis on between circular and oval micropillars

Statistical analysis of 231 orientation data. A) 231s on circular micropillars showed randomized alignment signified by high average degree of orientation across control and Y-27632 conditions. B) On oval micropillars, 231s showed no difference in alignment between control and Y-27632 groups. C) Comparing alignment between circular and oval micropillar substrates, 231s show no significant alignment. The data indicate that 231s do not align to oval micropillars.

10A-AT1-231 Comparison

After analyzing each cell line individually, we graphed the data side by side to elucidate variances in our quantified attributes as a function of malignancy. We began by looking at cell area across the three epithelial cell lines. From the data presented in Figure 51, we can see that although 10As and AT1s both show significant increases in cell area between control and 231CM conditions, AT1s are significantly smaller than 10As. 231s display similar size to 10As and are larger than AT1s in the control condition. Interestingly, treatment with Y-27632 reduces cell size in 10As but not in AT1s, and unexpectedly, cell size increases in 231 cell area when treated with Y27632. On oval micropillars, we see similar trends in each treatment group. AT1s are smaller than 10As and 231s in the control group and are also smaller than 10As treated with 231CM.

Next, we compared total fibril area between cell lines and found that, on circular micropillars, 10As assemble more FN than both AT1s and 231s, in the control group. 10As also assemble more FN than AT1s in both 231CM and 231CM + Y27632 treatment conditions (Figure 52). On oval micropillars, 10As assemble more FN than 10As and 231s in the control and 231CM conditions.

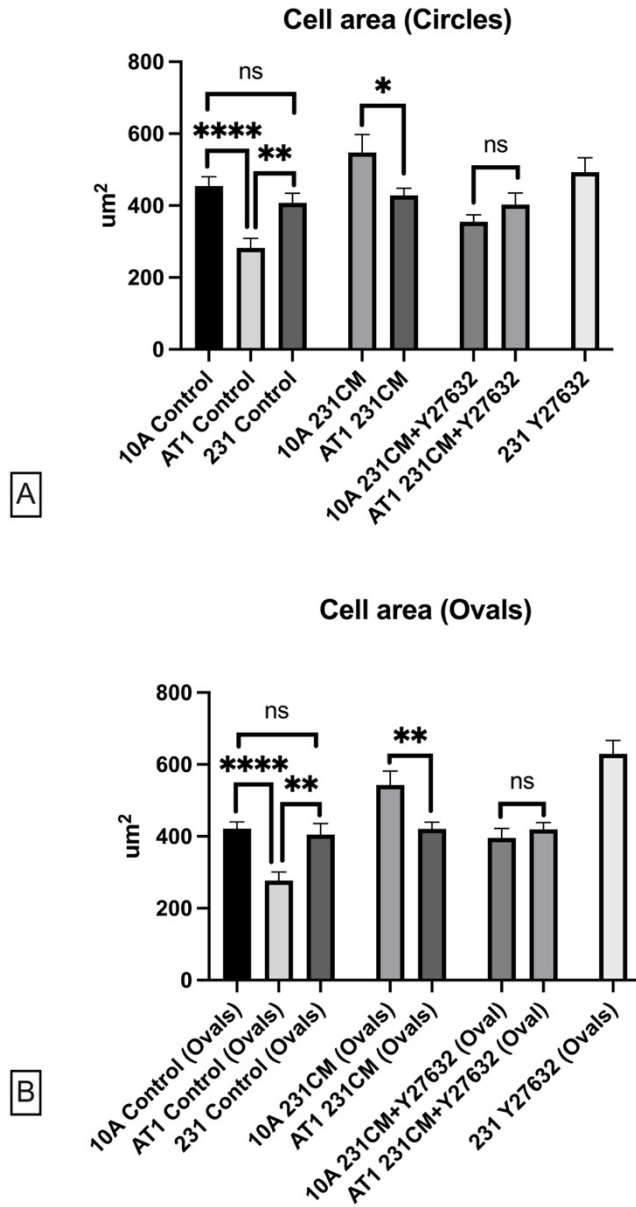


Figure 51: Comparison of MCF10A, MCF10AT1, and MDA-MB-231 cell area on circular and oval micropillars

Cell areas were compared across cell lines on circular micropillars (A) in control, 231CM, and 231CM + Y-27632 treatment groups. On circular micropillars, AT1s displayed significantly lower cell areas than both 10As and 231s in the control group. When treated with 231CM, AT1s and 10As both display larger cell areas, but maintain the relationship that 10As are significantly larger

than AT1s. In the 231CM + Y-27632 treatment group, 10A area was decreased, resulting in sizes similar to AT1s. 231s treated with Y-27632 are shown for reference. B) Cell areas were compared across cell lines on oval micropillars in control, 231CM, and 231CM + Y-27632 treatment groups. On oval micropillars, the trends remain comparable to those on circular micropillars. AT1s in the control group are significantly smaller than 10As and 231s. AT1s are significantly smaller when treated with 231CM and are similar in size to 10As in the 231CM + Y-27632 group. 231s, on oval micropillars, treated with Y-27632 shown for reference.

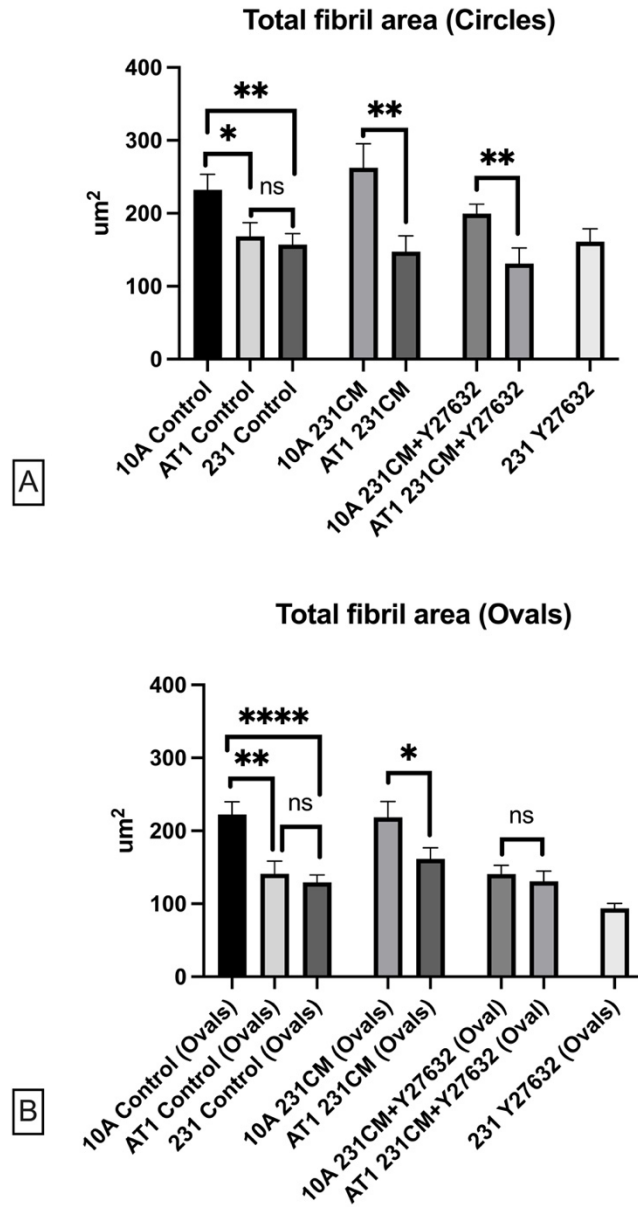


Figure 52: Total fibril area compared across MCF10A, MCF10AT1, and MDA-MB-231 on circular and oval micropillars

On circular pillars, (A), we found that 10As assembled a significantly greater amount of FN than AT1s and 231s in control, 231CM, and 231CM+Y27632 conditions. B) On oval micropillars, 10As assembled more FN than AT1s and 231s in the control and 231CM treatment groups. Inhibition

of force using Y-27632 resulted in decreased 10A fibril assembly to levels comparable to FN assembly by AT1s.

Comparison of total force between cell lines (Figure 53) revealed that 10As generate greater total force than AT1s and 231s in control and 231CM treatment groups, on both circular and oval micropillars. This is consistent with data presented in other works that correlate increasing malignancy with decreased traction forces. Treatment with Y-27632 reduces 10A total force to similar levels as AT1s. In Figure 54, we normalize total force against cell area and find that in the circular micropillar control group, 10As generate greater force per μm^2 than both AT1s and 231s, while AT1s generate a significantly higher force per μm^2 than 231s. On oval micropillars, 10As and AT1s generate similar force per μm^2 , and both are significantly greater than 231 force per μm^2 .

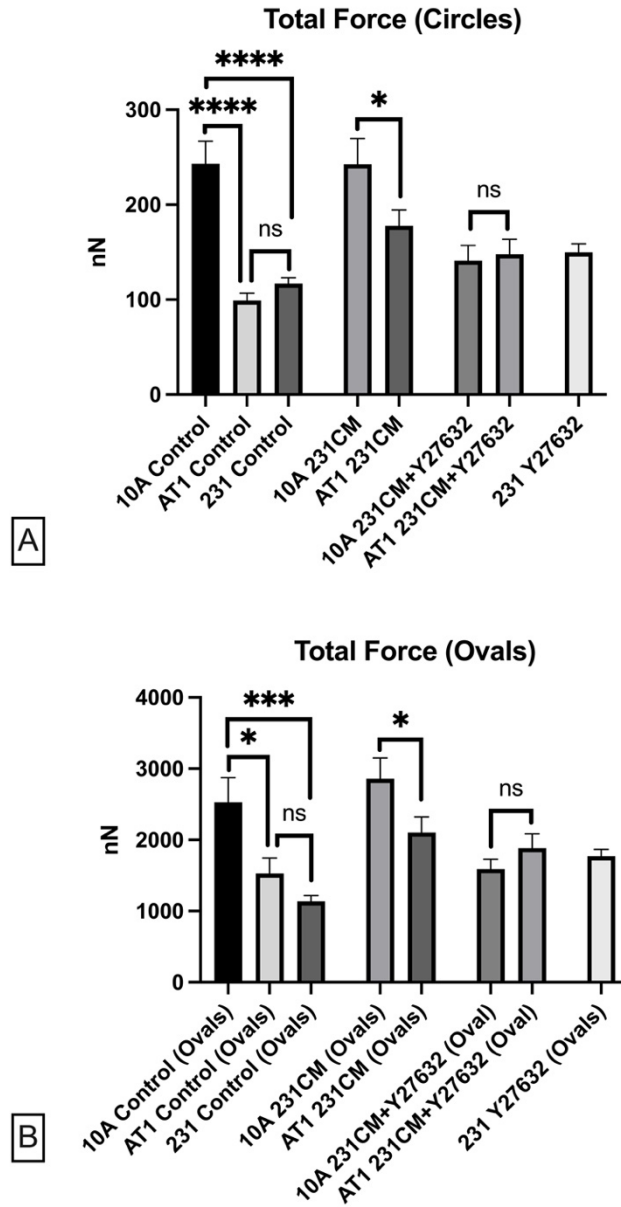


Figure 53: Epithelial cell traction forces on circular and oval micropillars

MCF10A, MCF10AT1, and MDA-MB-231 forces quantified on circular and oval micropillars.

Cells were treated with either 231CM or 231CM + Y-27632 to determine their effects on force.

A) On circular micropillars, 10As displayed significantly higher total force than both AT1s and 231s in control and 231CM conditions. When stimulated with 231CM and Y-27632, 10As and AT1s generated a similar amount of force. B) Similar to the results on circular micropillars, 10As

on oval micropillars generated significantly higher forces than AT1s and 231s in the control and 231CM conditions.

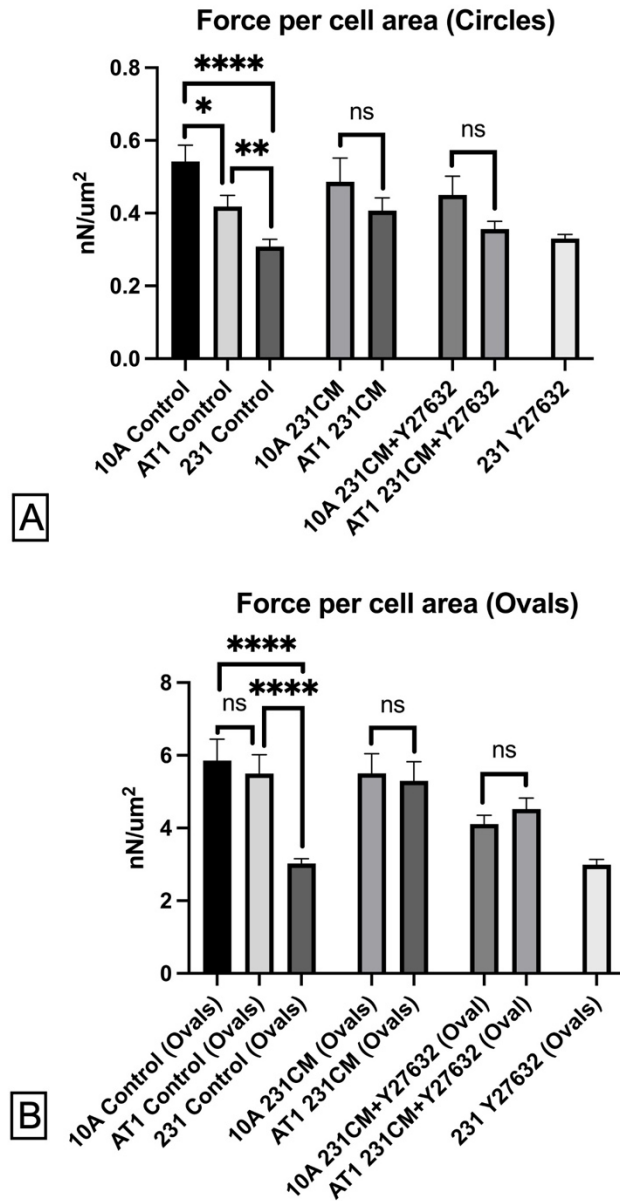


Figure 54: Epithelial cell total force normalized against cell area

10A, AT1 and 231 total force normalized against cell area. A) On circular micropillars, the data show that 10As generate higher force per cell area than AT1s and 231s in the control condition only. B) On oval micropillars, AT1s generate forces comparable to 10As in the control condition. Both 10As and AT1s display larger force per cell area than 231s.

Lastly, we compare cell orientation, or alignment, between 10As, AT1s and 231s on oval micropillars. Across all cell lines and treatment conditions, only one combination displayed significantly increased alignment. Only 10As which were treated with 231CM displayed alignment to the major axis of oval micropillars (Figure 55).

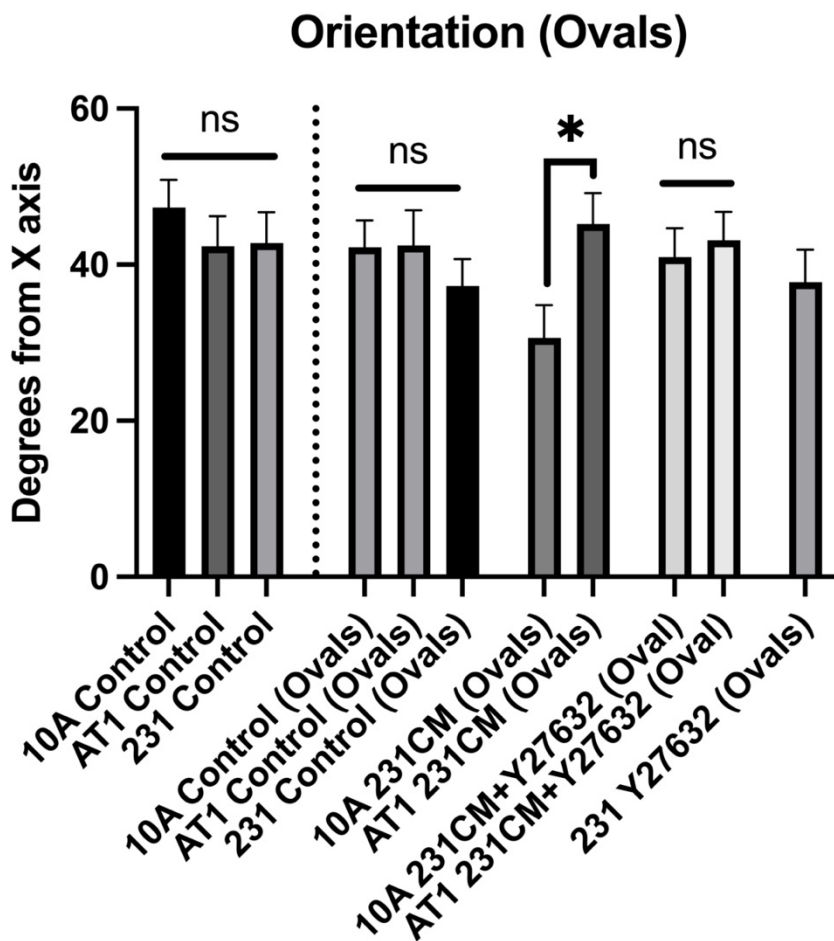


Figure 55: 10A, AT1, and 231 cell orientations on oval micropillars

Average cell orientations were quantified in 10As, AT1s, and 231s on circular and oval micropillar substrates. From left to right: we began by displaying random alignment of 10As, AT1s, and 231s on circular micropillars, which serves as our control. On oval micropillars, 10As treated with 231CM exhibit increased alignment which is rescued to normal levels with the addition of Y-27632. Across all conditions, only 10As treated with 231CM display alignment to oval micropillars.

4.4 Discussion

To recap, in this chapter we seeded progressively malignant mammary epithelial lines (MCF10As, MCF10AT1s, and MDA-MB-231s) on circular and oval micropillars to elucidate their response on substrates with different mechanical properties. Cells were treated with 231CM, 231CM + Y27632, or Y27632 alone to study the effects of upregulating and downregulating force on epithelial cell mechanoresponse. Overall, our findings show that 10As are the most responsive to chemotactic stimulation with 231CM and Y-27632. 10As generally have the largest cell area, assemble the most FN, display the largest forces and were the only cell line to display increased alignment on oval micropillars. AT1s responded to 231CM by displaying larger cell area and increased FN fibril assembly but did not downregulate these responses in the 231CM + Y-27632 group.

One interesting point to note is that our data indicate unique cell area responses to Y-27632 treatment as a function of malignancy. First, 10As in the 231CM + Y-27632 group displayed decreased cell area compared to the 231CM group. AT1s showed no change in cell area or FN assembly in response to Y-27632 and 231s showed larger cell areas when treated with Y-27632. These data indicate that there could be an inverse relationship between cell area and malignancy when force is inhibited with Y-27632. Comparing force per μm^2 , the data show that 10As and AT1s generate higher forces than 231s on both circular and oval micropillar substrates. Finally, it is worth reiterating that significant alignment to oval micropillars was only demonstrated by 10As treated with 231CM.

Overall, the data suggest that epithelial cell line characteristics are not greatly altered when presented with anisotropic mechanical cues; epithelial cell lines seem more responsive to

chemotactic stimuli. We postulate that cells become less mechanoresponsive as they get more malignant. This downregulation of mechanoresponse may be what allows metastatic cells to ignore the mechanical cues, presented by circumferentially aligned collagen fibers in TACS 2, to break through the collagen layer and invade into stromal tissue. In the next chapter, we develop a novel migration assay to mimic the mechanical cues presented by the 3 TACS architectures and recapitulate chemotactic gradients present in the TME to investigate the effect of anisotropic mechanical cues on malignant cell invasion.

Chapter 5

Migratory response of cells to *in vitro* mimetics of Tumor-Associated Collagen Signature (TACS) biomechanics

5.1 Rationale

It is well known that mechanical and chemotactic stimuli can guide cell alignment and migration. Previous works have demonstrated that cells will migrate to the stiffest region of substrates with stiffness gradients^{58,67}. This is known as durotaxis. Another phenomenon known to influence cell migration is contact guidance, in which cells align to and migrate along linear, aligned structures^{12,38,46}. In addition to these works, in Chapter 3, we demonstrate that fibroblasts respond to oval micropillars by aligning to them. Other works have demonstrated that cells exhibit

a strong migratory response to chemotactic gradients^{4,6}. To our knowledge, no studies have been able to recreate a multi-cue migration environment that includes the anisotropic stiffness, aligned contact guidance, and chemotactic gradients which define the TME. Although many previous studies have developed unique assays which mimic the linearly aligned ECM found in TACS 3 and have tried to justify that, when set up in perpendicular orientation relative to cell migration, these can be used to represent TACS 2, few, if none, have developed assays to accurately mimic circumferentially aligned fibers (TACS 2). In addition to only being partially representative of the mechanical conditions in the TME, none to date have been able to capture all the above characteristics within one device.

In this chapter, we developed a novel microfluidic migration assay which is capable of mimicking the various collagen architectures (TACS) and chemotactic gradients in the TME. With this new tool we can develop and test new methods to decrease the probability of malignant cells invading surrounding tissue. If we can prevent or downregulate metastasis, we could greatly increase survival rates. The data shown demonstrates that the unique mechanical cues presented by each TACS has a profound impact on cell migration. We also attempted to elucidate the effect of chemotactic gradients on cell migration but found results to be inconclusive. Further development and experimentation are needed to draw conclusions on this matter.

5.2 Radial Microfluidic Design

We began by assessing how circumferentially and radially aligned fibers could be replicated *in vitro* using oval micropillars (Figure 56). We designed four new micropillar array designs to mimic TACS 1-3 in a radial pattern (Figure 57). The images in Figure 57 show sections, similar to the red boxed regions in Figure 56, of the interface between the circular central seeding area and the surrounding micropillars. Utilizing the mask generator (μ PG 101) under its minimum resolution required creative strategies such as patterning undersized squares and rectangles to produce circles and ovals. To mimic TACS 1, we used circular micropillars in both seeding and migration areas, thus providing a mechanically isotropic surface (Figure 57A). To mimic TACS 2, we used oval micropillars aligned circumferentially around the central seeding area (Figure 57B). Next, we developed a mixed design to mimic the transition phase between TACS 2 and TACS 3 where a few cells may have invaded the stroma, leaving behind radial tracks within the circumferential collagen layer (Figure 57C). Finally, to mimic TACS 3, we used oval micropillars exclusively aligned radially outward from the central seeding area (Figure 57D).

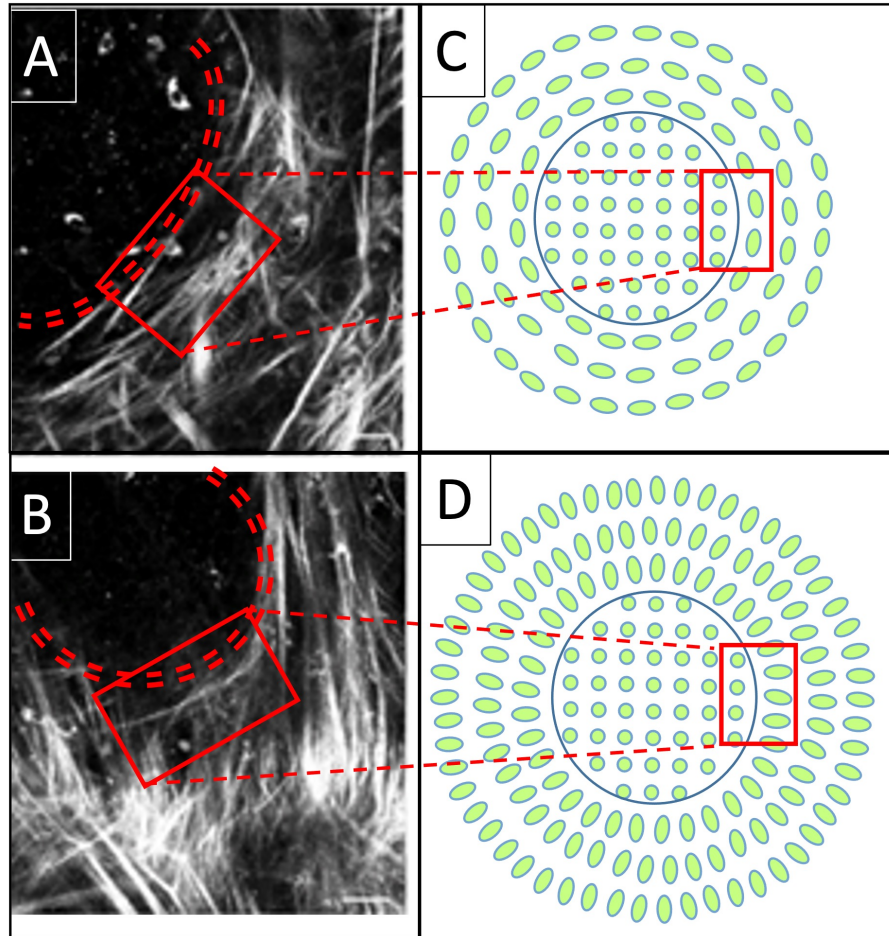


Figure 56: Translating TACS mechanics to a micropillar/microfluidic approach

The images above demonstrate the relationship between ECM organizations TACS 2 and TACS 3 and their micropillar counterparts. A) Multiphoton laser scanning image of collagen fibers aligned circumferentially around the tumor boundary (TACS 2). B) Multiphoton laser scanning image of collagen fibers aligned radially or perpendicular to the tumor boundary (TACS 3). Double dashed red lines indicate the tumor boundary. C & D) Theoretical representations of micropillar arrangements which mimic anisotropic stiffness and contact guidance cues provided by collagen fibers. Images in 56A and 57B reproduced with permission from Provenzano et al.⁹

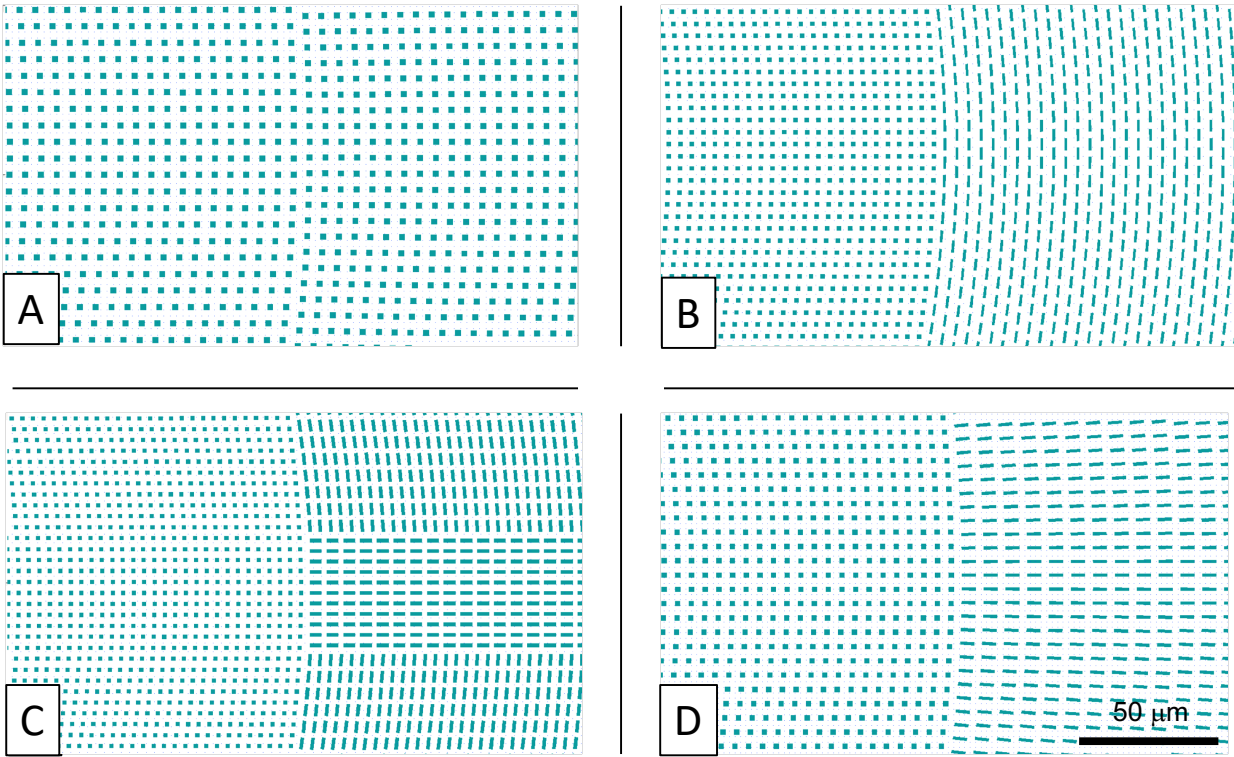


Figure 57: TACS Mimicking Micropillar Arrangements

Micropillar patterns generated in CleWin to mimic each possible TACS arrangement. The Heidelberg Instruments uPG 101 used to write these patterns onto the masks has a minimum resolution of 3 μm . Due to this, a new process utilizing undersized squares (1.25 μm x 1.25 μm) and rectangles (1 μm x 4 μm) was needed to generate 2.25 μm circles and 2.25 μm x 4.5 μm ovals. A) Isotropic design at the interface displaying no specific anisotropic stiffness or contact guidance by utilizing all circular micropillars. This arrangement mimics the non-specific collagen organization in TACS 1. B) Oval micropillars aligned circumferentially around a central isotropic seeding area mimic circumferential collagen organization in TACS 2. C) Radial tracks of oval micropillars distributed throughout a circumferential arrangement of oval micropillars. This mimics the transitional phase between TACS 2 and TACS 3 where few initial cells have invaded into the stroma leaving behind narrow and sparsely located tracks across the tumor-stroma interface. D)

Oval micropillars aligned radially mimic the aligned fibers of collagen leading away from the tumor boundary seen in TACS 3. Scale bar represents 50 μm .

We then developed a novel microfluidic design, shown in Figures 58-63, which limits cell seeding only to the central seeding area and allows us to generate a chemotactic gradient across the migration area. There are two distinct reservoirs, inner and outer, which allow for the formation of a chemotactic gradient across the migration area. In order to prevent pressure driven fluid flow across the migration area, which would destabilize any chemotactic gradients, two pressure equilibration tubes were utilized to connect the inner and outer reservoirs. Although these prevent flow across the migration area, they also introduce the potential for chemokine diffusion into the inner reservoir. To prevent chemokine buildup in the inner reservoir, a syringe pump system was used to continuously refresh the media. A second syringe pump was used to refresh the outer reservoir to maintain a stable chemokine concentration. We demonstrated the efficacy of our dual syringe pump system at maintaining gradient through the addition of fluorescein isothiocyanate (FITC), a green, fluorescent molecule, to the outer reservoir. Gradient formation was visualized with fluorescent imaging and shown in Figure 65 with and without continuous media refresh of the inner reservoir.

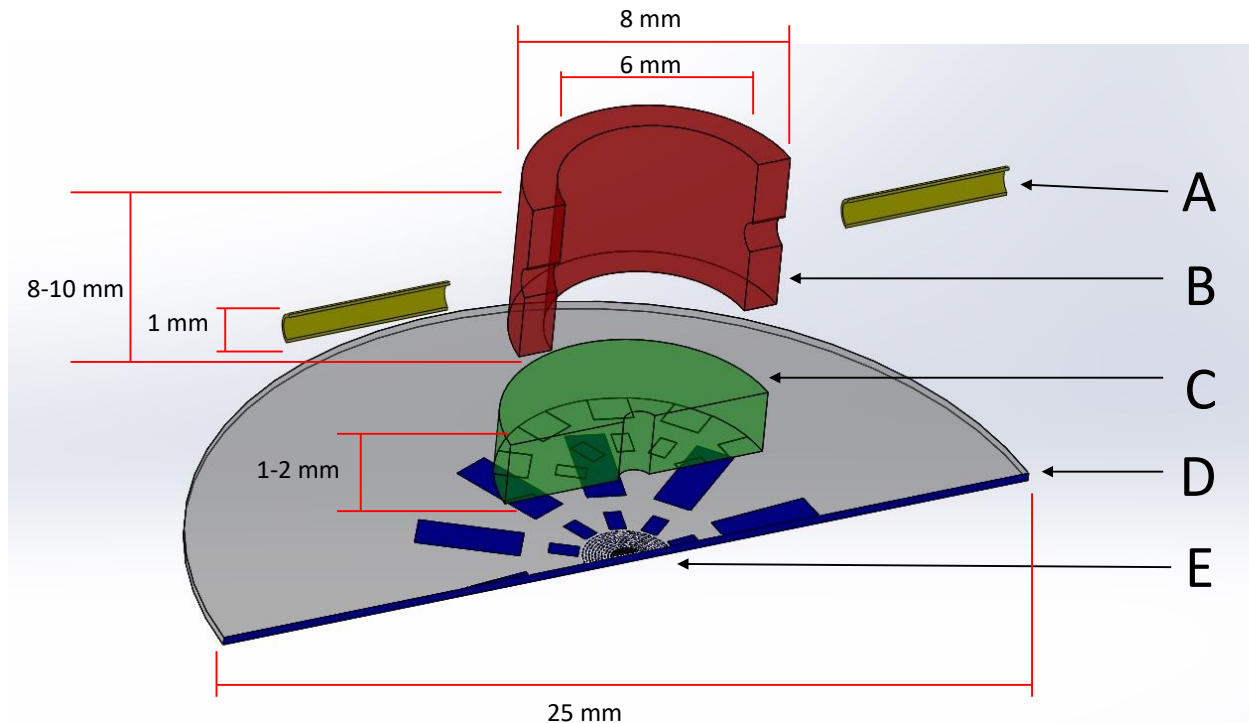


Figure 58: Radial Microfluidic Assembly

SolidWorks model of the radial microfluidic assembly. The base of the radial microfluidic is a 25mm coverslip (D) with micropillars and support structures (E) (blue) fabricated directly on the coverslip. The next layer is a PDMS cylinder (C), of 8mm outer diameter, with support structures on the bottom surface that correspond to support structures on the coverslip. When bonded together, these support structures determine the height of the migration area. Part C has a 1mm diameter section removed from the center to create a cylindrical cell seeding well. This limits cell seeding to the central region of the assay. Part B is a PDMS cylinder, 8mm outer diameter and 6mm inner diameter, which is bonded to the top of part C to form the inner media reservoir. Part B has two 1mm diameter holes cut into the side walls where two PDMS tubes (A) are inserted. These tubes connect the inner media reservoir to the outer media reservoir to equalize any pressure differences which would create unwanted fluid flow across the migration area. The inner media reservoir is filled with serum free media, and the outer media reservoir is filled with full serum

media to generate a radial (outside to inside) chemotactic gradient. The gradient stimulates outward cell migration from the central seeding area. Parts E, C, and B are permanently bonded together through surface activation by plasma.

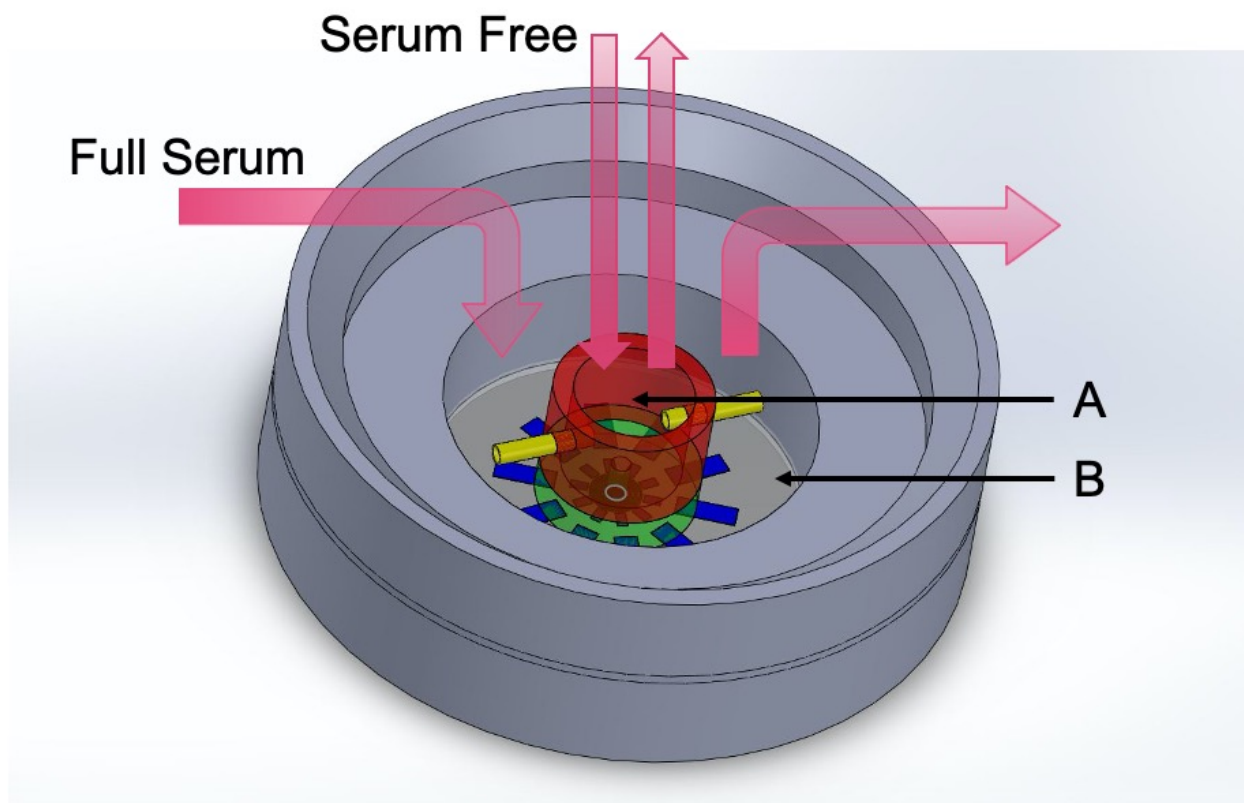


Figure 59: Radial Microfluidic Assembly Within Specimen Holder

The parts in Figure 58 are assembled and placed into a metal specimen holder. The specimen holder is a two-piece design which sandwiches the coverslip between the top and bottom rings creating a leak-proof seal. This forms two distinct volumes, one inside the PDMS structure and one outside. These are the inner (A) and outer (B) media reservoirs. The inner reservoir is used for cell seeding and filled with serum free media. The outer reservoir is filled with full serum media to generate a chemotactic gradient across the migration area. Two syringe pumps are used to continuously refresh both volumes to maintain a constant gradient.

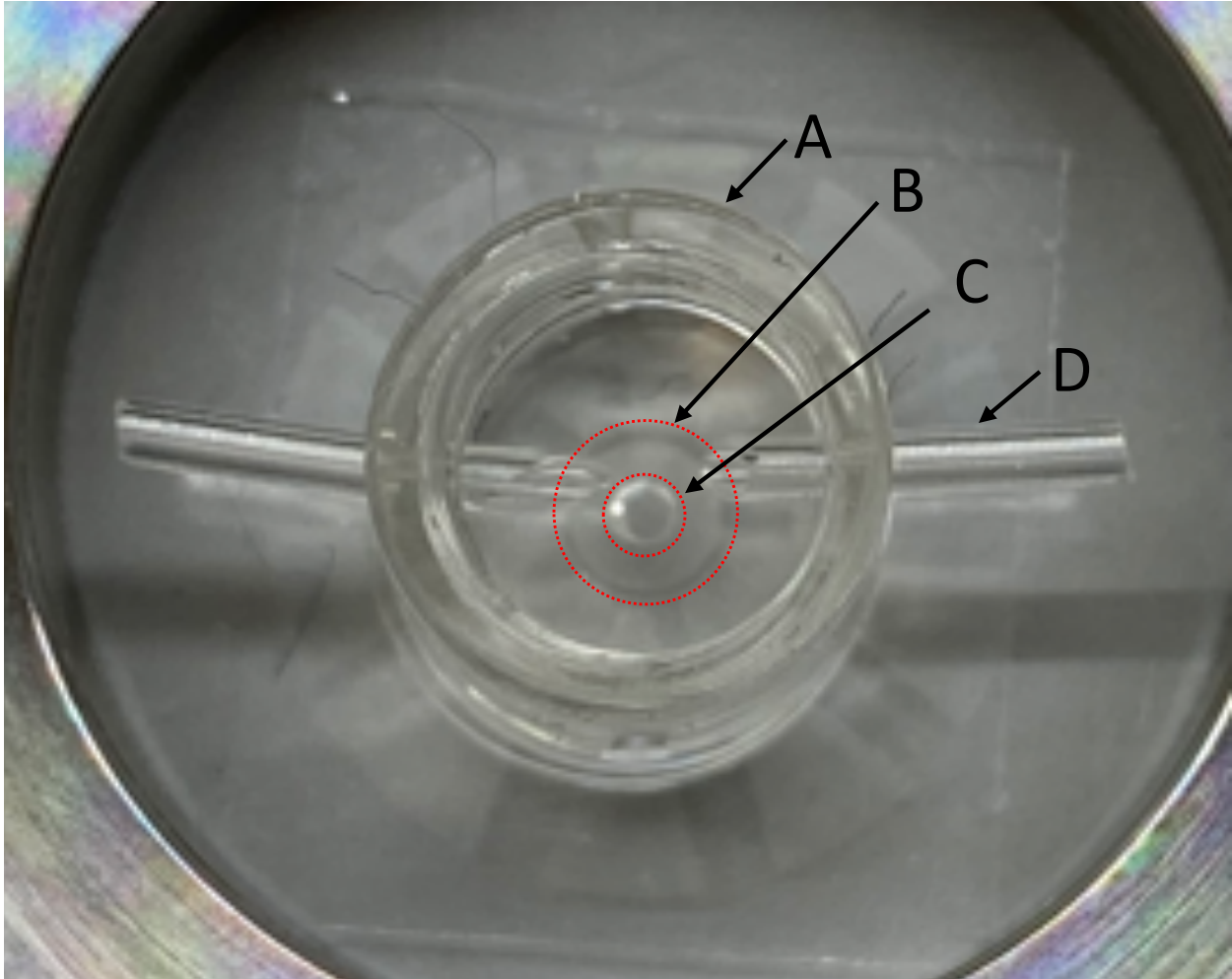


Figure 60: Top-down view Radial Microfluidic Assembly Within Specimen Holder

A close-up view of the inner reservoir once the microfluidic assembly is seated within the specimen holder. In this panel we are able to clearly visualize the A) upper structure of the inner reservoir, B) outer circumference of the migration area, C) seeding well, D) and pressure equilibration tubes. The migration area is the cylindrical region in between the two red dotted outlines. This area is where our different micropillar arrangements (isotropic (circles only), circumferential, tracks, or radial) are located.



Figure 61: Inner reservoir tube setup

Image of assembled microfluidic in specimen holder. Short tubes (top and bottom) are 1 mm diameter pressure equilibration tubes and longer tubes (left and right), also 1 mm diameter, serve to refresh the inner volume of the microfluidic.

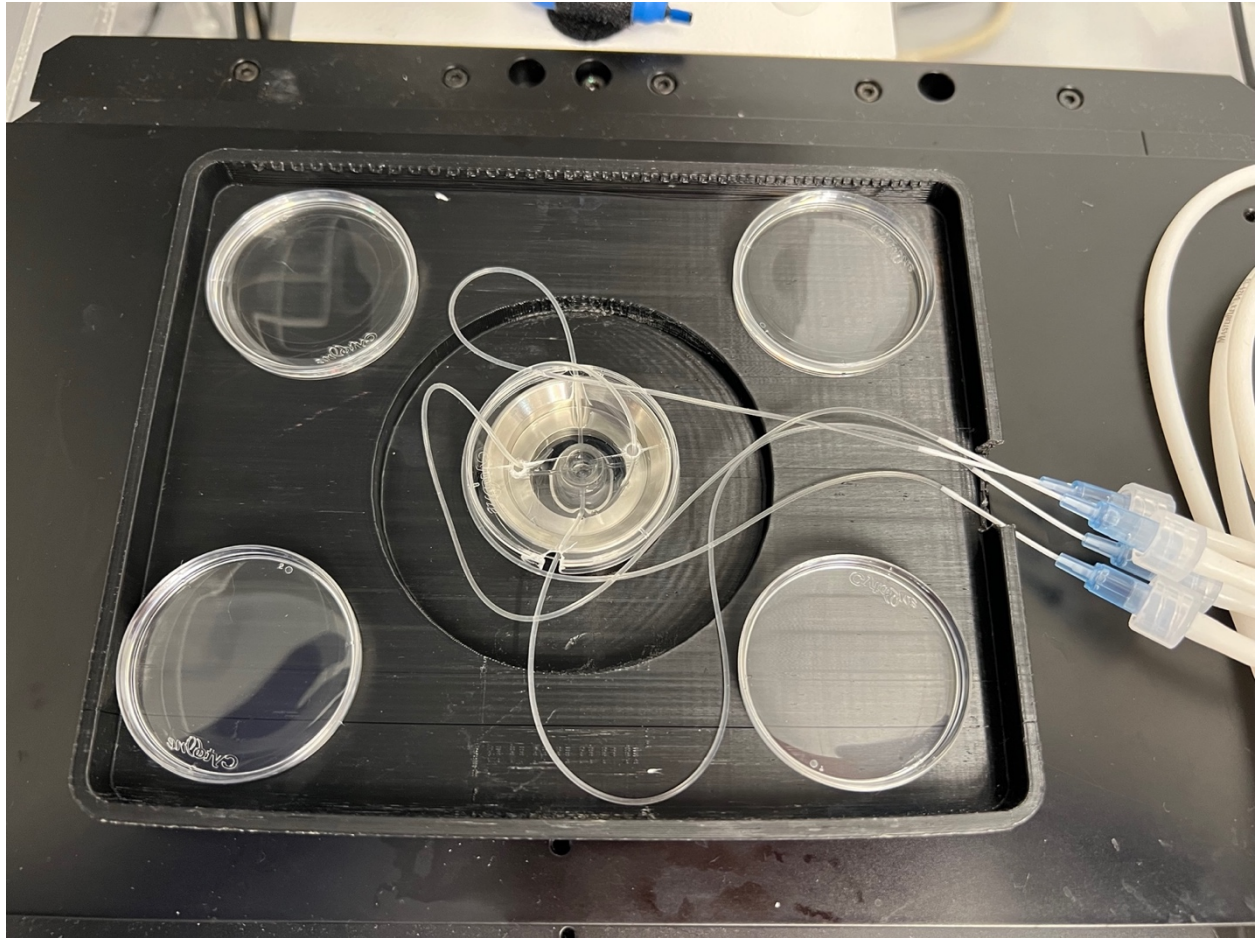


Figure 62: Radial Microfluidic on Custom Stage Insert

Microfluidic assembly setup on microscope stage in preparation for imaging. Stage insert was custom designed, and 3D printed to provide an enclosed volume to maintain at 5% CO₂. Tubes from syringe pumps are routed through a cutout on the right side of the stage insert and through a 35mm petri dish (p35) lid to access the inner and outer reservoirs of the microfluidic. Four p35 lids are arranged in the corners of the stage insert and filled with deionized water to humidify the chamber.



Figure 63: Microfluidic tube routing

Close up image of tubing arrangement. A p35 lid with two side cutouts and two pass-through holes on the top is used to guide the tubes. The tubes (top and bottom) are routed through the side cutouts in the p35 and then through the wall of the inner media reservoir to refresh the inner volume. Two tubes (left and right) are routed through the two pass-through holes in the top of the p35 lid to access the outer media reservoir. This p35 lid also serves to minimize media evaporation from the specimen holder.

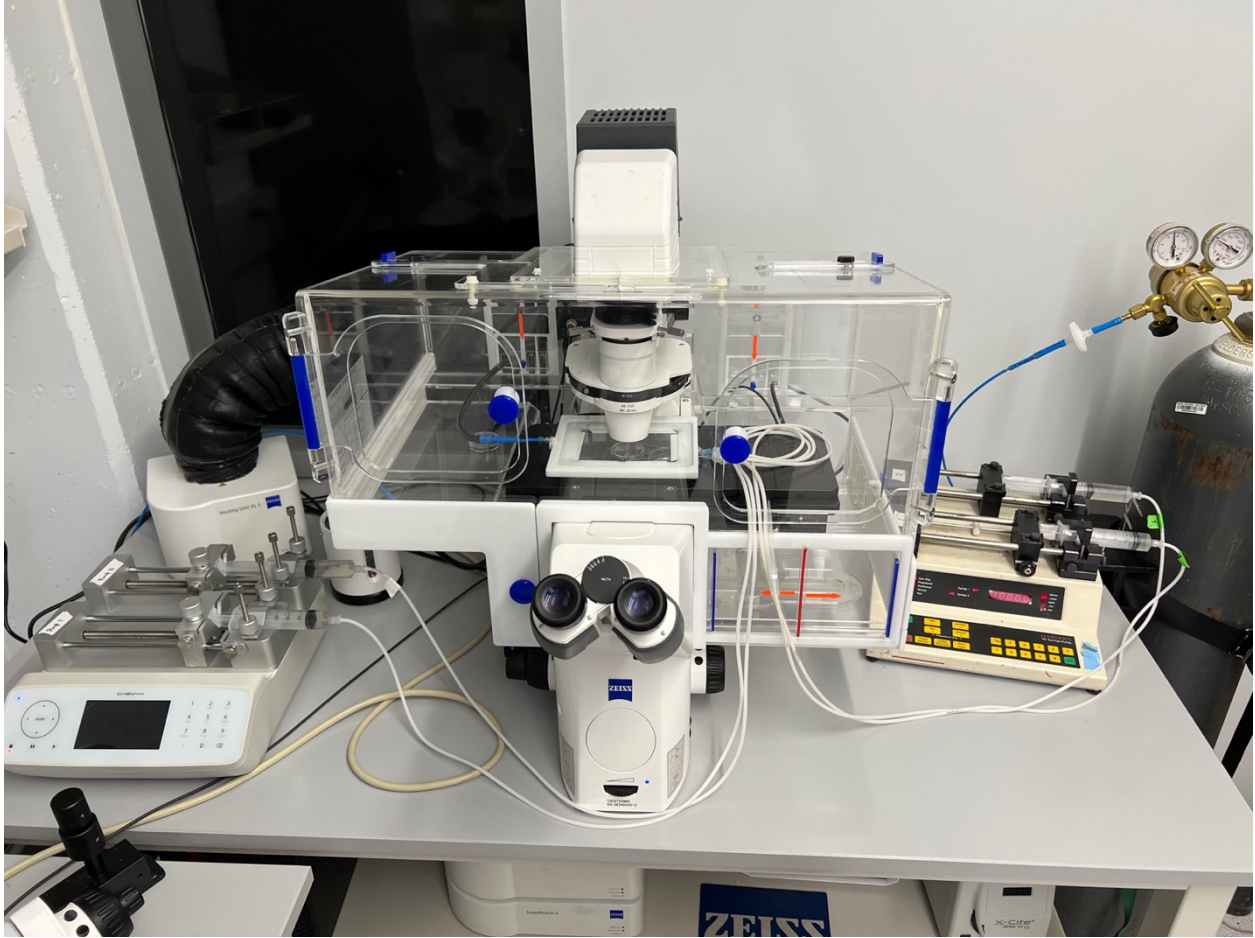
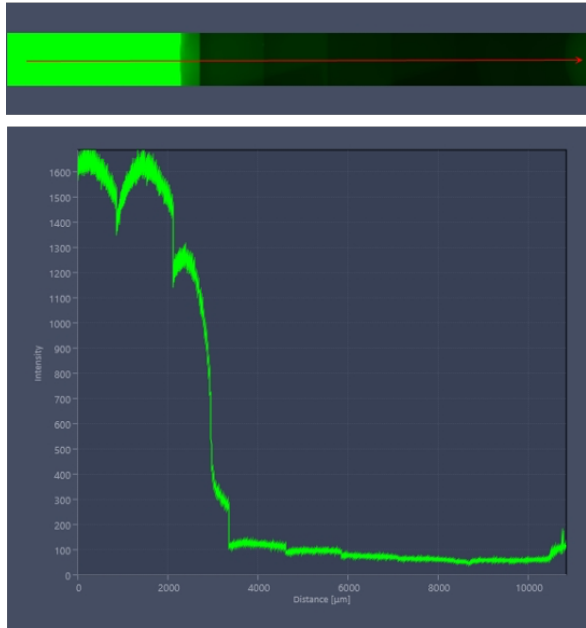


Figure 64: Syringe pump and microscope arrangement

We use two dual-channel syringe pumps set up on the left and right side of the Zeiss Axio Observer microscope to refresh the inner and outer media reservoirs. Within each syringe pump system, one syringe serves as the input and the other withdraws volume. They are run at the same flow rate (10 $\mu\text{L}/\text{min}$) to maintain the fluid level in the reservoir. Tubes are routed through the right-side door on the incubation chamber. Extra length of the tube is coiled and placed on the stage to act as a heating element for the media.

With Media Refresh



Without Media Refresh

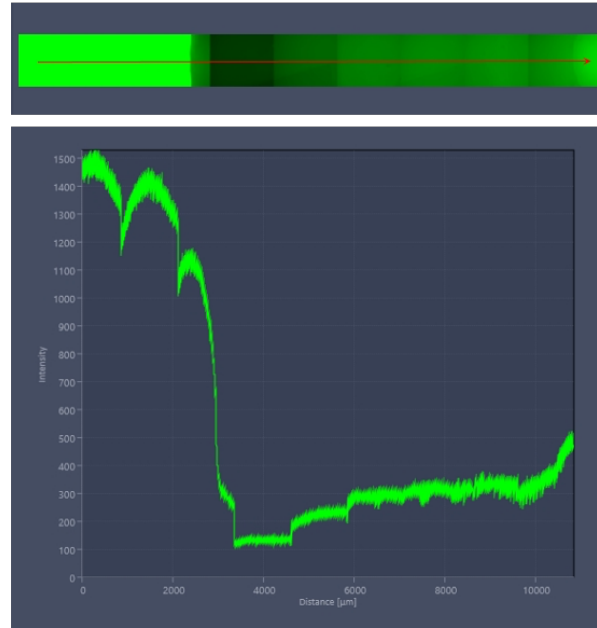


Figure 65: FITC Visualization of Chemoattractant Gradient Profiles

Fluorescence intensity profile of a stabilized FITC gradient between the outer and inner media reservoirs, with and without media refresh. Outer reservoir is located at the left of each profile and inner seeding well is located at the right. The images on the left show the intensity profile while syringe pumps are continuously refreshing both volumes. The images on the right show the increase in intensity in the inner reservoir after the pumps have been shut down. The gradient is no longer maintained and FITC is allowed to build up, predicting an increased concentration of chemokine and degradation of the chemotactic gradient.

5.3 Methods

5.3.1 Fabrication of TACS mimicking substrates and upper support structure layer

TACS mimicking micropillar substrates and upper support layer were fabricated as described in 3.2.1. Pillars and lower support structures were fabricated at a height of 5 μm and the upper support structures were fabricated at a height of 15 μm .

5.3.2 Microcontact printing, microfluidic assembly, and imaging setup

Micropillars were functionalized with fibronectin (FN) (Sigma-Aldrich Fibronectin from human plasma, F0895) using the following process: Flat PDMS (30:1 blend) “stamps” were cut out of bulk PDMS with a 3 mm tissue biopsy punch. They were coated with 20 μL of 200ng/mL FN and allowed to incubate at room temperature for 1 hour. During this 1 hour wait period, the upper structures were prepared. An 8 mm tissue biopsy punch was used to cut out the upper support layer from the PDMS mold taken from the wafer. Then, a 1 mm tissue biopsy punch was used to remove a cylindrical section from the center to create the seeding well. The upper structure was formed by removing a 8mm cylinder out of bulk 10:1 PDMS with a biopsy punch. A 6 mm biopsy punch was then used to remove the inner section of the 8mm cylinder, leaving behind a thin-walled cylinder. Next, we created four 1mm holes in the side of the thin-walled cylinder, two for the pressure equilibration tubes and two for the media refresh tubes. For the time being, these four holes were plugged with 1 mm PDMS cylinders.

When 10 minutes of the 1 hour FN coating wait step remained, the micropillar coverslip was exposed to UV (Novascan PSD pro series digital UV ozone system) for 10min to activate the

top surfaces of the pillars to facilitate protein transfer. Concurrently, the upper support layer and inner reservoir wall (thin wall cylinder) were bonded together by surface activation through plasma exposure (Harrick plasma HP plasma cleaner) at medium power for 35 seconds. Next, excess FN solution was removed from stamps by gently submerging them in DI water and drying with sterile nitrogen. Stamps were then inverted and placed in contact with the micropillar tops to transfer FN. The upper PDMS structure was then aligned and bonded to the 25mm coverslip with the micropillars, and then placed in an incubator at 37°C for 5 minutes to strengthen the bonds. The assembly was removed from the incubator and placed into a metal specimen holder and, to prevent micropillar collapse, fluids of increasing surface tension (100% Ethanol, 70% Ethanol, and PBS) were flowed through the system. Fluorescent BSA was then flowed through the system for 1 hour to stain surfaces not coated with FN. Next, 1% F-127 was flowed through the assay to block cell adhesion to areas not coated with FN. Finally, fresh media was flowed through the system for 30 minutes to wash out any remaining F-127. Cells were seeded in the inner reservoir and allowed to attach overnight for a total of ~21 hours.

The next day, syringe pumps were set up in advance with either both 1% serum (chemotactic control condition), or one with 1% serum and 10% serum in the other (chemotactic gradient condition). At 21 hours post seeding, a solution of 2 drops NucBlue Live (Thermo Fisher Scientific R37605) in 1 mL 1% serum media was prepared and exchanged with the media that the cells were seeded in. The sample was then placed into the incubator, at 37C, for 30 minutes before adding 2 mL of 1% serum and incubating for a minimum of 30 minutes. The specimen holder was then removed from the incubator, pressure equilibration and media refresh tubes were attached, and the sample was placed onto the microscope (pre-heated to 37C). Refer to Figures 60-64 for details. The sample was incubated on the microscope stage for two hours to allow the incubator

temperature to restabilize. Imaging was started at 24 hours post seeding, and images of fluorescently labeled cell nuclei were collected every 20 minutes to track cell migration. Migration data was collected over 24 hours and analyzed using the Trackmate plugin in ImageJ. Please refer to the supplemental documents for a more detailed setup protocol.

5.3.3 Cell culture

NIH-3T3s were selected to investigate cell mechanoresponse to TACS mechanics. This cell line was chosen because it is well known to respond to mechanical cues^{68,69}, as we demonstrated in chapter 3. NIH-3T3s were cultured in high glucose DMEM (Thermo Fisher Scientific 11995065) with 10% bovine calf serum (Sigma Aldirch C8056-500mL) and 1% antibiotic – antimycotic (Gemini Bio-Products 400-101). DMEM without phenol red (Thermo Fisher Scientific 21-063-029) with 1% sodium pyruvate (Cassion Labs PYL01-100mL) was used during live cell imaging. Either 1% or 10% bovine calf serum was added to the media depending on experimental condition.

5.3.4 FIJI - Trackmate Analysis

CZI files were stitched in ZEN and exported as TIFFs. Video files were opened in FIJI and annotated with a black circle, seen in Figures 66-68, to prevent Trackmate from tracking cells inside the seeding well. Videos were processed through Trackmate to generate raw data⁷⁰.

5.3.5 MATLAB and Statistical analysis

The data was then analyzed in MATLAB, using an original author written program, to calculate R, S, R/S, track displacement, cell displacement, persistence, and velocity. This data was transferred into GraphPad Prism for statistical analysis. Statistically different significances were

determined by a One-way ANOVA followed by a student's t-test. A total of 3 samples per condition were analyzed and the total cell counts are as follows. 3T3s in the 1% serum condition on TACS 1 n = 86, TACS 2 n = 103, TACS 3 n = 43. 3T3s in the serum gradient condition on TACS 1 n = 75, TACS 2 n = 82, TACS 3 n = 122.

5.4 Results

NIH-3T3s were seeded on micropillar designs representing TACS 1, TACS 2, and TACS 3, and migration characteristics were assessed over a 24-hour period. We began by visually analyzing Trackmate output of cell tracks overlaid over our radial microfluidic images. In Figure 66, cells on our TACS 1 (isotropic) design travel in tracks that lead radially outward, but also meander and travel in the circumferential direction. When subject to TACS 2 (circumferentially aligned ovals) mimicking mechanical cues, cells travel radially outward from the central seeding well and quickly turn perpendicularly and travel in the circumferential direction (Figure 67). In Figure 68, cells on the TACS 3 (radial ovals) substrate migrate radially outward with a high level of persistence. These figures illustrate the strong capability of oval micropillars to guide 3T3 migration.

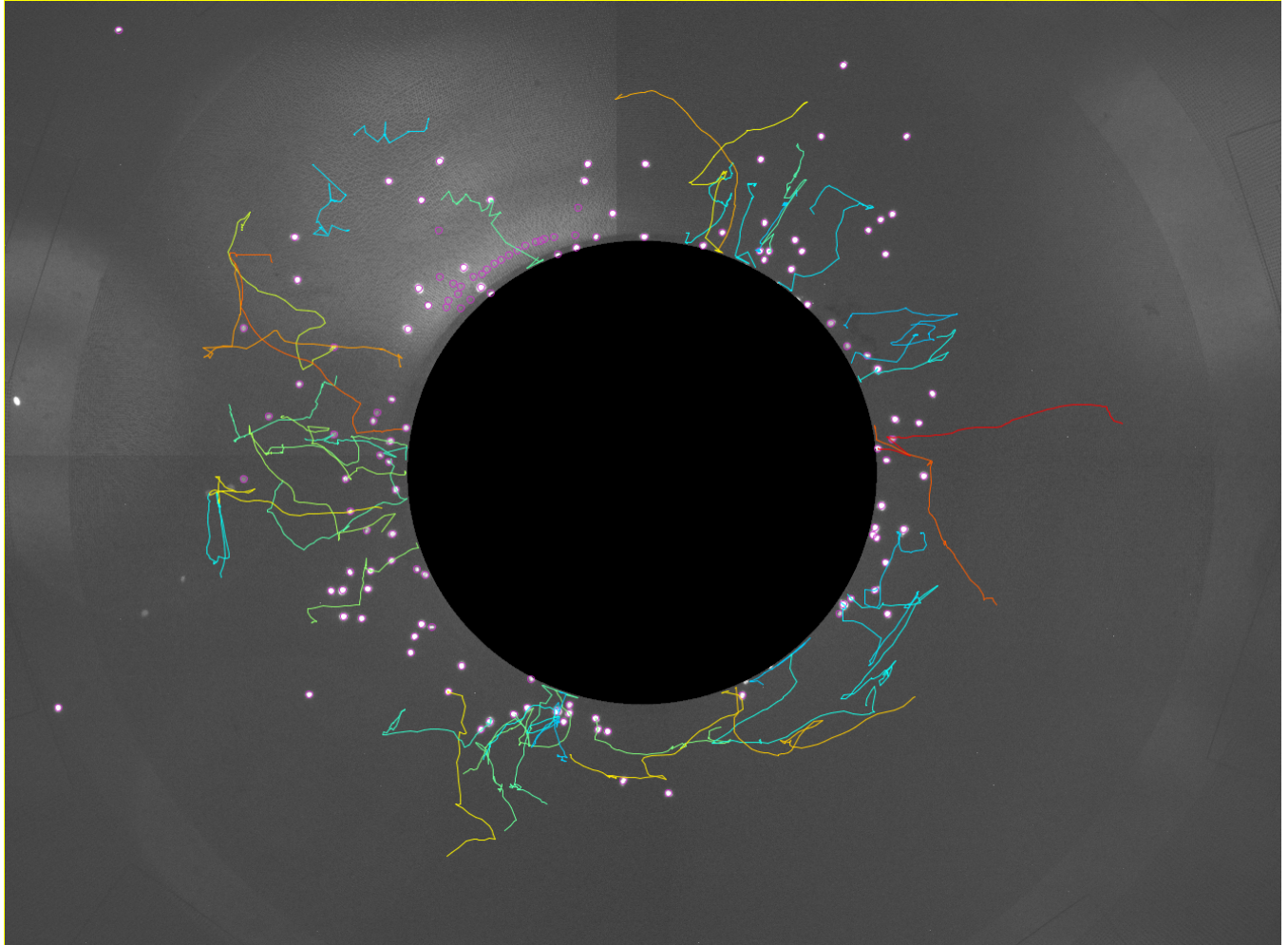


Figure 66: NIH-3T3 Migration on TACS 1 Design

NIH-3T3 cells migrating radially outward on TACS 1 micropillar arrangement (Figure 57A). Through visual inspection, cells seem to take paths that generally lead radially outward, but many meander or zig-zag along the way. Many cells in the lower right quadrant display circumferential travel. This image was taken from a serum gradient sample but displays similar characteristics to the 1% serum samples. Pink circles identify individual cell nuclei. Colored lines indicate individual cell paths. Lines are color coded to indicate distance traveled; blue being the shortest and red indicating the longest.

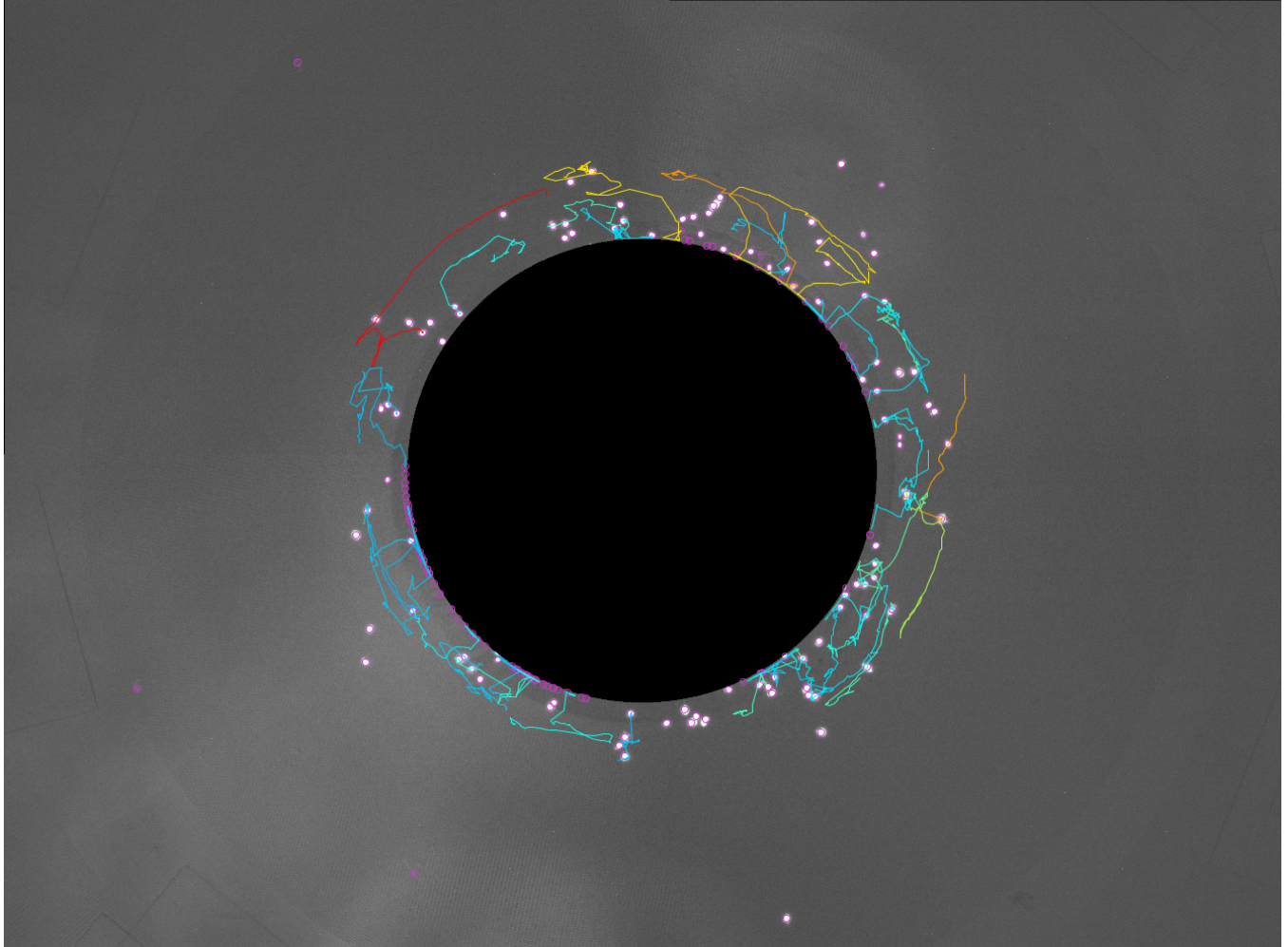


Figure 67: NIH-3T3 Migration on Circumferential Design (TACS 2)

NIH-3T3 migration on TACS 2 micropillar design (Figure 57B). Through visual inspection, most cells travel outward from the central seeding wells and abruptly turn perpendicularly to travel in a circumferential manner when they meet the circumferentially aligned oval micropillars. This image was taken from a serum gradient sample but displays similar characteristics to the 1% serum samples. Pink circles identify individual cell nuclei. Colored lines indicate individual cell paths. Lines are color coded to indicate distance traveled; blue being the shortest and red indicating the longest.

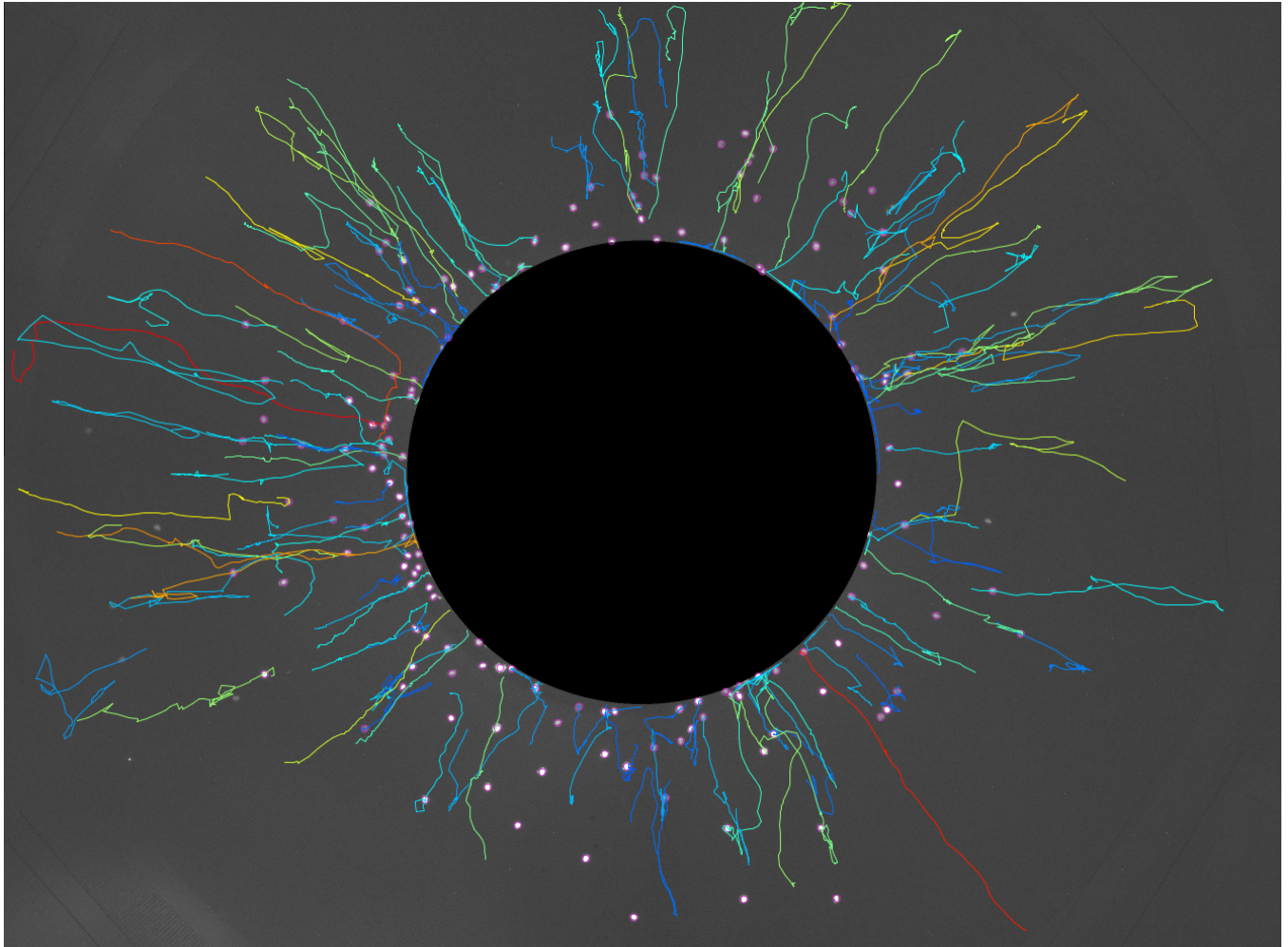


Figure 68: NIH-3T3 Migration On Radial Design (TACS 3)

NIH-3T3 migration on TACS 3 micropillar design (Figure 57D). Most cells travel outward from the central seeding wells and show strong persistent migration radially outward. This image was taken from a serum gradient sample but displays similar characteristics to the 1% serum samples. Pink circles identify individual cell nuclei. Colored lines indicate individual cell paths. Lines are color coded to indicate distance traveled; blue being the shortest and red indicating the longest.

1% Serum Results

3T3s were exposed to two different chemotactic profiles: 1) no gradient, in which 1% serum was supplied to both the inner and outer reservoirs, and 2) a serum gradient, in which 1% serum was supplied to the inner reservoir while 10% serum was supplied to the outer reservoir. We begin by describing the migration characteristics of cells on the TACS 1, TACS 2 and TACS 3 designs in the chemotactic control condition (1% serum). From our Trackmate images shown in the figures above, we can clearly see that there are significant directional differences in migration across the 3 TACS scenarios, so we start by analyzing those. Cell tracks were converted from cartesian to polar coordinates and subsequently broken down into theta and radius components. The change in radius (ΔR) indicates how far a cell has traveled radially outward from center of the design. The change in theta, or angle, indicates how far a cell has traveled circumferentially and is quantified in degrees or radians. In order to make this easier to compare to our change in radius, we multiply theta by R to yield S , or the distance traveled circumferentially. From here forward we use ΔR and ΔS to describe the differences in migration direction. We then take the ratio between these two by dividing S by R to provide a descriptive characteristic, the S/R ratio. An S/R value of 1 indicates that a cell traveled an equal distance in both S and R directions and ideally indicates fully random migration. A large S/R value indicates that a cell traveled much further circumferentially than radially, and a small S/R value indicates that a cell traveled further radially rather than circumferentially.

In Figure 69, we analyze ΔR , ΔS , and S/R ratio for the 1% serum condition set of experiments. In panel A, we see significant differences in radial travel. In comparison to the control (TACS 1), cells on the TACS 2 design display significantly reduced radial migration while cells

on the TACS 3 substrate display increased radial migration. In Figure 69 panel B, the opposite trend is shown: cells on TACS 2 travel significantly further circumferentially, while cells on TACS 3 travel significantly less. In C, we display our calculated S/R ratio. Cells in the TACS 1 group display an S/R ratio of approximately 1, confirming that cells display random migration on isotropic substrates. In the TACS 2 group, cells display a high S/R ratio of about 2.5, indicating that on circumferential ovals, cells traveled approximately 2.5 times the distance circumferentially than radially. In TACS 3, we calculated a low S/R ratio of approximately 0.5, indicating that cells traveled half as far circumferentially than radially. These summarize and confirm that anisotropic stiffness and contact guidance, provided by oval micropillars, strongly influence 3T3 migration.

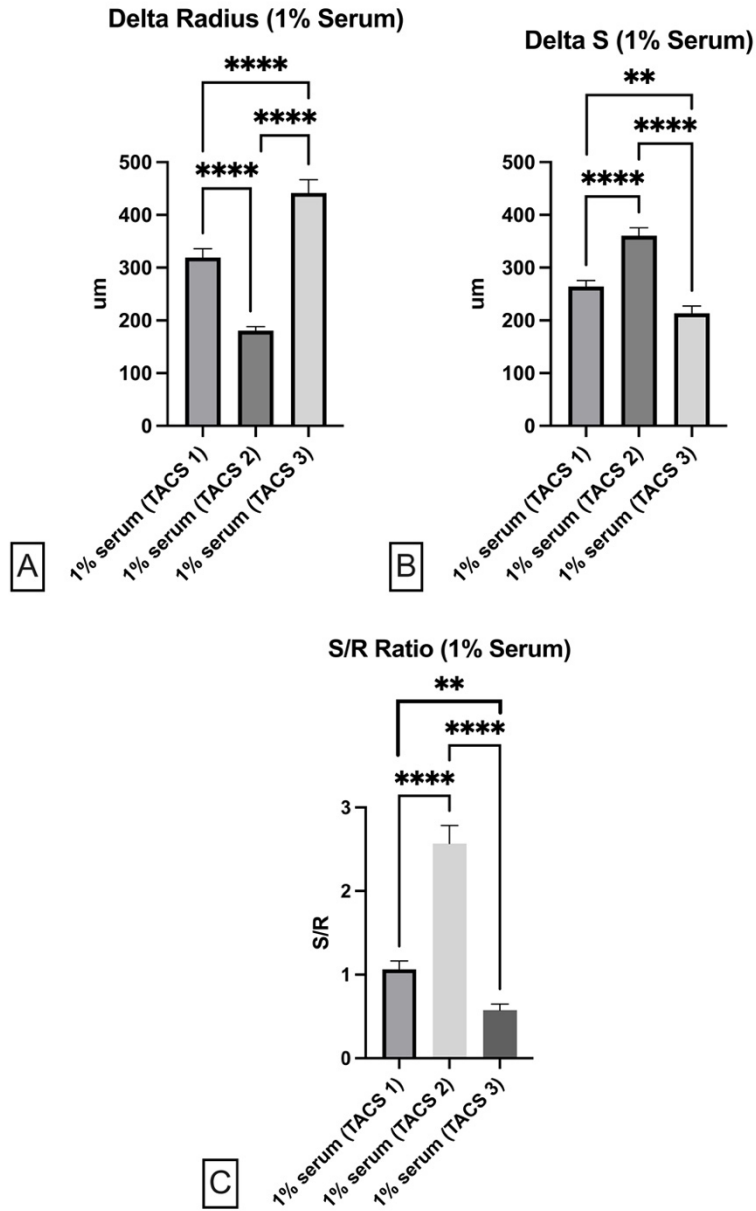


Figure 69: 1% serum 3T3 migration analysis

3T3 migration was analyzed on the TACS 1, TACS 2, and TACS 3-mimicking mechanical scenarios. 1% serum was supplied in the inner and outer media reservoirs. Cell migration tracks were broken down into radial and S (circumferential) components and analyzed. A) Delta radius (distance traveled radially) quantified on TACS 1, 2 and 3 mechanical scenarios. The data clearly show that cells on the TACS 2 design migrate radially outward significantly less than cells on the

TACS 1 design while cells on the TACS 3 design migrate significantly more. B) Delta S (distance traveled circumferentially) on TACS 1, 2, and 3 designs. The data confirm that cells on the TACS 2 design travel circumferentially significantly further than the TACS 1 group and cells in the TACS 3 group travel circumferentially less than both TACS 1 and TACS 2 groups. We then divided S by R to give us the S/R ratio (panel C). Cells in the TACS 1 group (isotropic design) display an S/R ratio of approximately 1, which indicates that they traveled randomly (approximately an equal distance in both directions). Cells in the TACS 2 group display a high S/R ratio (~ 2.5) indicating that they travel much further circumferentially than they do radially. Lastly, cells in the TACS 3 group show a low S/R ratio (~ 0.5) indicating that they travel further in the radial direction than circumferentially.

Next, we assessed track displacement, cell displacement, persistence, and velocity (Figure 70). Track displacement was quantified as the linear distance between start and end points of each track. The data in panel A show that, compared to the control, cells on the TACS 2 design display a lower track displacement, and cells on the TACS 3 design display higher track displacement. We then compared cell displacement, which was quantified as the total distance traveled by the cell; and we once again see that cells on the TACS 3 design travel a longer distance than those on TACS 1 or TACS 2. Persistence was calculated by taking the ratio between track displacement and cell displacement. A persistence value of 1 would indicate that a cell traveled in a perfectly straight line since track displacement would equal cell displacement. As the persistence value decreases, it indicates that a cell meandered more on its path from start to end. In panel C, we see that cells on the TACS 1 substrate display a persistence of approximately 0.5. Using this as our control, we notice that cells in the TACS 2 design show significantly decreased persistence. This is validated by the track outlines in Figure 67, in which we see that cells travel radially outward first and then turn and travel circumferentially. If the start and end points were connected on the plots, we would notice that many would look like a triangle, indicating a large deviation from the linear start to end path. Cells on TACS 3 display a significantly higher persistence which is, once again, validated by the plot above (Figure 68), which displays relatively linear cell tracks leading radially outward. Finally, we analyzed velocity and the data show that cells on the TACS 3 design travel significantly faster than those on TACS 1 or TACS 2. To summarize, 3T3s are extremely mechanoresponsive to the mechanical cues provided by oval micropillars and strongly prefer to migrate along the major axis of oval micropillars with high efficiency. The data show that 3T3s on the TACS 3 substrate travel the furthest, the fastest, with the greatest persistence.

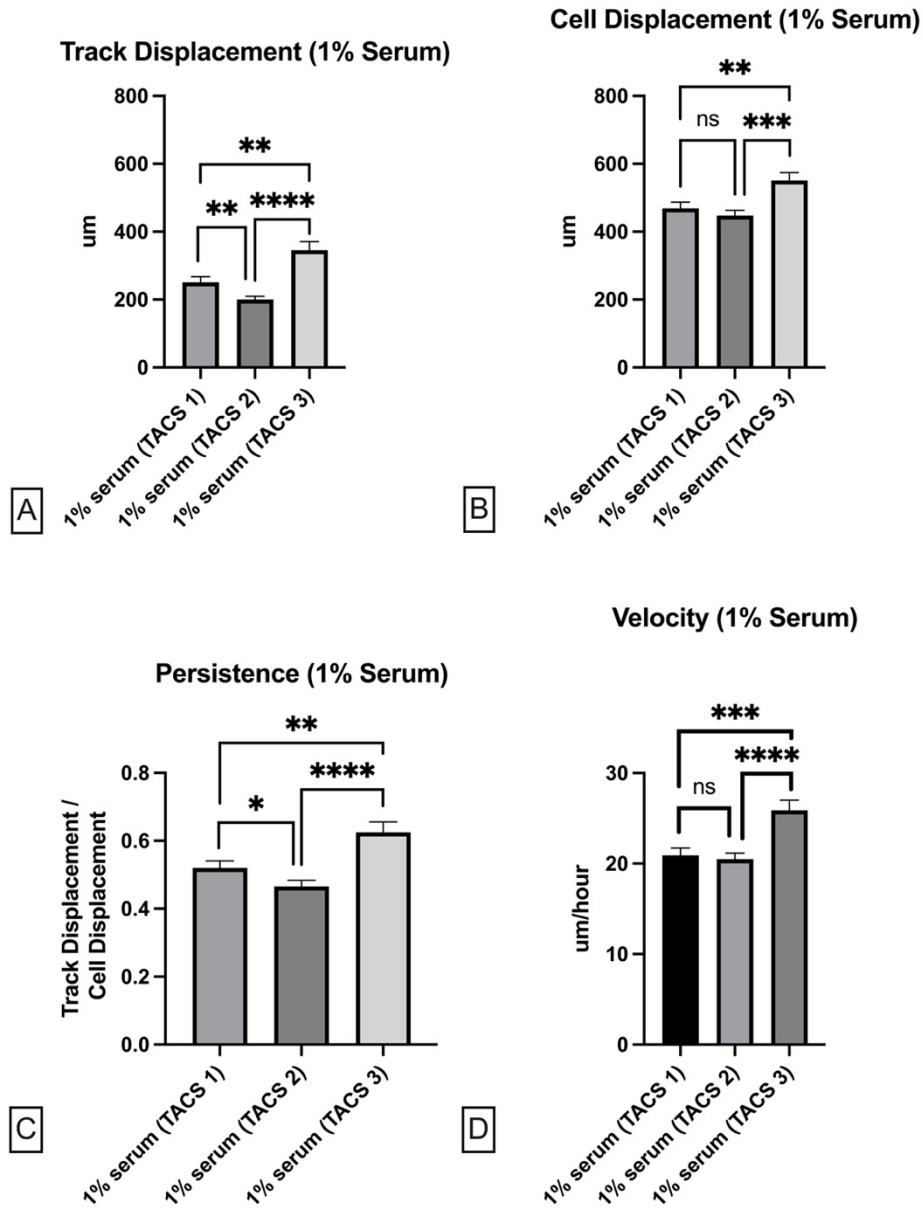


Figure 70: 1% serum 3T3 displacement, persistence, and velocity analysis

We quantified track displacement (A), which is the direct distance between start and end points of each cell track. The data show that cells in the TACS 2 scenario display significantly shorter track displacement. Conversely, cells in the TACS 3 scenario display longer track displacements. Cell displacement (B) is the total distance traveled by the cell. The results show that cells in the TACS 3 group travel a further total distance than cells in the TACS 1 and TACS 2 groups. C)

Persistence was calculated by dividing track displacement with cell displacement. A persistence value of 1 (track displacement = cell displacement) would indicate that a cell traveled in a perfectly straight line. A lower value indicates that a cell meandered more along its path from start to finish. Cells in the TACS 2 group show decreased persistence, and cells in the TACS 3 group show increased persistence when compared to the TACS 1 (control) group. D) Average velocity calculated for each of the three TACS conditions. Cells on the TACS 3 design traveled with significantly higher velocity than cells in TACS 1 and TACS 2 groups. Overall, the data demonstrate that cells in the TACS 3 group travel further, with greater persistence, at a higher velocity.

Serum Gradient Results

After establishing 3T3 migration characteristics in the migration assay based solely on varying mechanical properties, we introduced a chemotactic gradient and investigated how migration characteristics were altered. Just as in the 1% serum scenario, we began by analyzing S, R, and S/R. In Figure 71, we see that once again relative to the control (TACS 1), cells in TACS 2 travel significantly less radially and cells in TACS 3 travel significantly further. When we look at delta S, we see the same results as the 1% serum experiments. Cells on the TACS 2 design travel significantly further circumferentially than in the control and cells in the TACS 3 group travel circumferentially less than the control. When we look at S/R ratio (panel C), we notice that while cells in the TACS 2 scenario show a significant difference from TACS 1, cells in TACS 3 do not, indicating that cells in the TACS 1 and TACS 2 groups display similar directional migration characteristics.

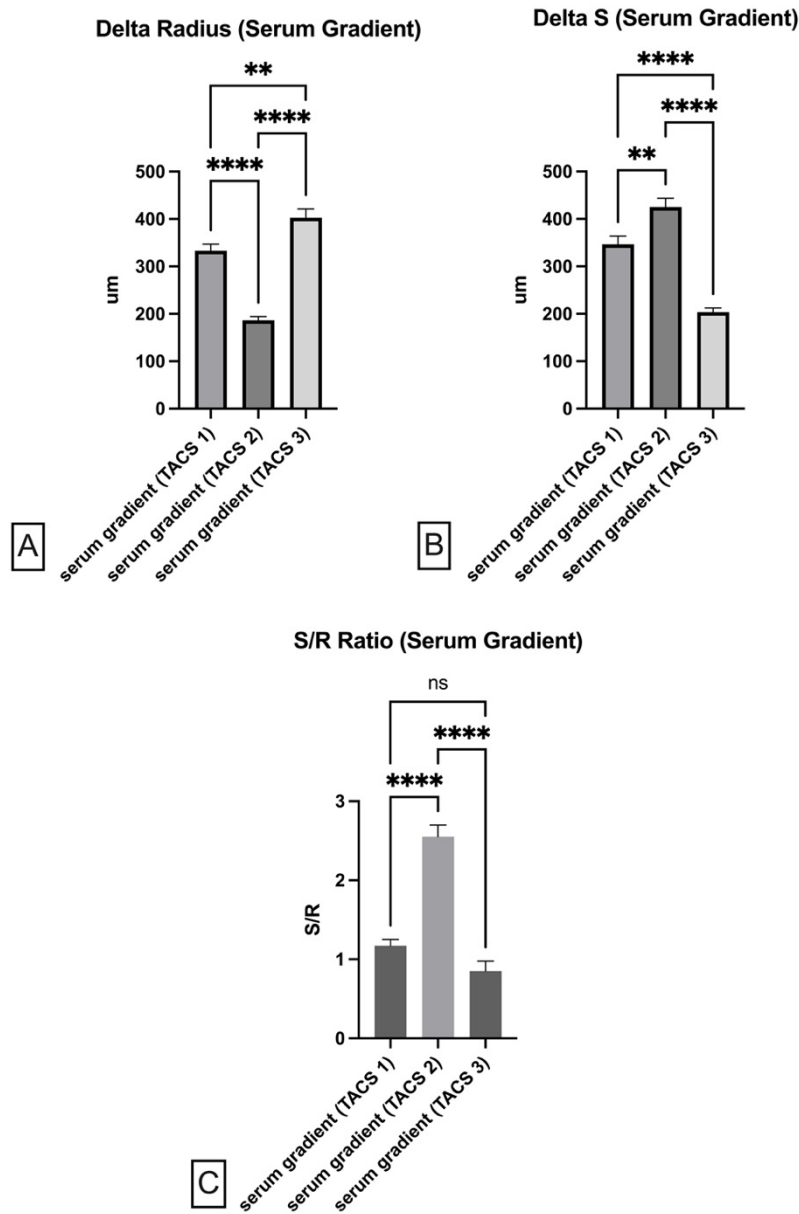


Figure 71: Serum gradient 3T3 migration analysis

Delta radius, delta S and S/R quantified for serum gradient experiments. Across these metrics, we see the same trends that were found in the 1% serum data above. A) When compared to the control cells, the TACS 2 group display decreased radial migration and the TACS 3 group display increased radial migration. B) Cells in TACS 2 display increased circumferential migration and

TACS 3 cells display decreased circumferential migration. C) Cells in the TACS 2 condition display significantly higher S/R ratio than both TACS 1 and TACS 3 groups.

Next, we assessed track displacement, cell displacement, persistence, and velocity. In Figure 72 panel A, we see that track displacement (end to end) is significantly different across all three conditions. Cells in TACS 3 show the greatest track displacement and cells in TACS 2 display the lowest. Comparison of cell displacement (panel B), unlike the results from the 1% experiment, show no significant differences. Persistence data (panel C) show similar results to the 1% scenario, where cells in TACS 3 travel with the greatest persistence, and cells in the TACS 2 condition travel with the least persistence. Finally, we see that cells on TACS 1 and TACS 2 substrates travel with similar velocity, but cells on TACS 3 substrate travel significantly faster.

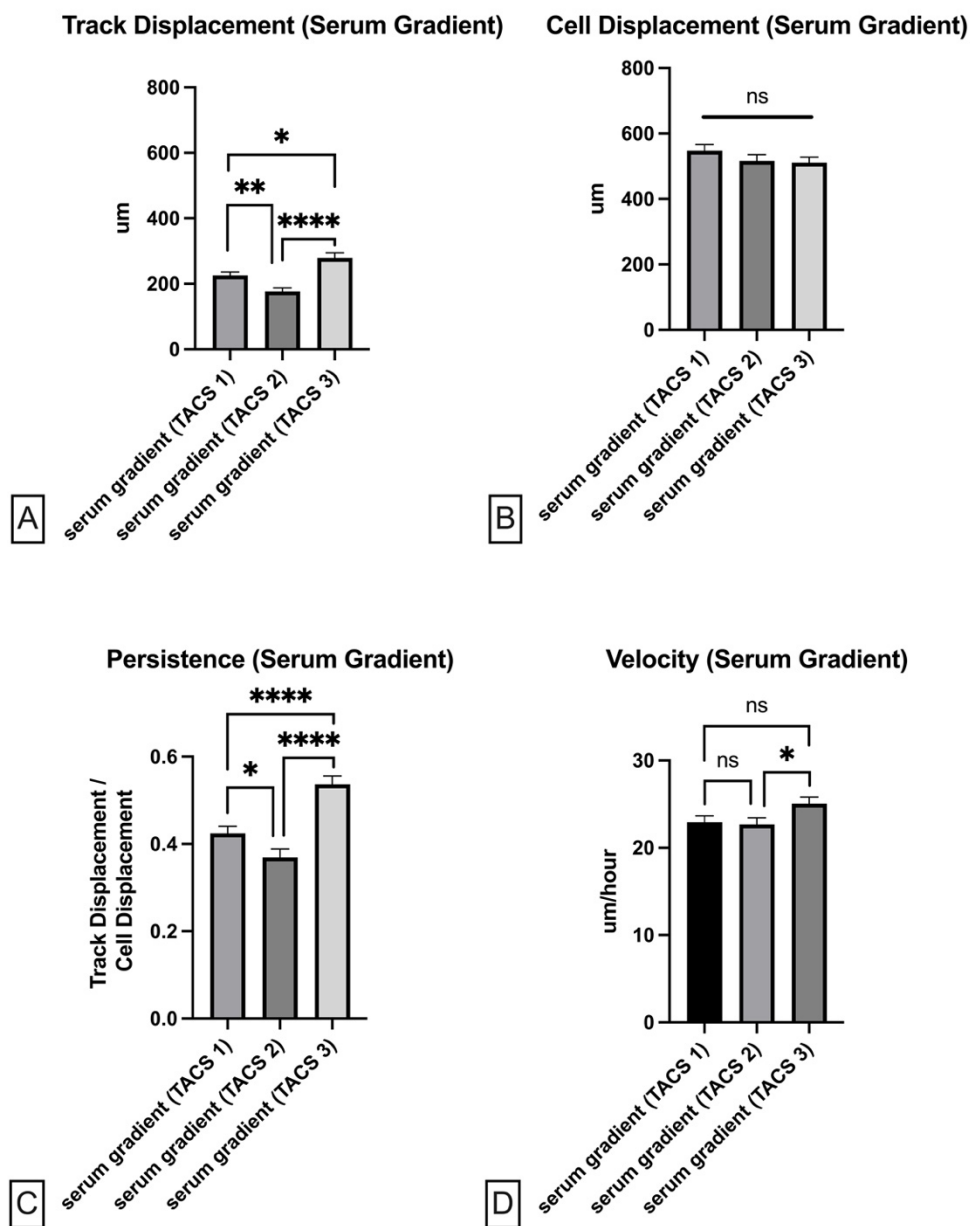


Figure 72: Serum gradient 3T3 displacement, persistence, and velocity analysis

Track displacement, cell displacement, persistence and velocity quantified for cells across TACS 1, 2, and 3 groups while exposed to a serum gradient. A) Cells in TACS 2 display lower track displacement and cells in TACS 3 display greater track displacement than the TACS 1 control. B) The data show no significant changes in cell displacement between TACS 1, 2, and 3. C) Cells on the TACS 2 substrate display decreased persistence while those on the TACS 3 substrate display

increased persistence. D) Cells on the TACS 3 substrate travel at a higher average velocity than those on TACS 2 or TACS 3.

1% serum vs serum gradient comparison

Comparing the data between 1% serum and serum gradient conditions, we do note some significant differences that contradict our expected outcomes. In addition to comparing the results between these two groups, we added in a full serum (10%) no gradient condition to mimic standard culture conditions. Across most metrics we do not see a significant difference between 10% serum and our chosen control of 1% serum. We only see that cells in the TACS 1 1% serum group display a higher velocity than the TACS 1 10% serum group, thus confirming that our choice to use 1% serum as our control was appropriate.

The data show no differences in delta radius between 1% serum and serum gradient groups (Figure 73). In panel B, the data show a significant increase in delta S in TACS 1 and TACS 2 groups. There were no significant differences in S/R ratios.

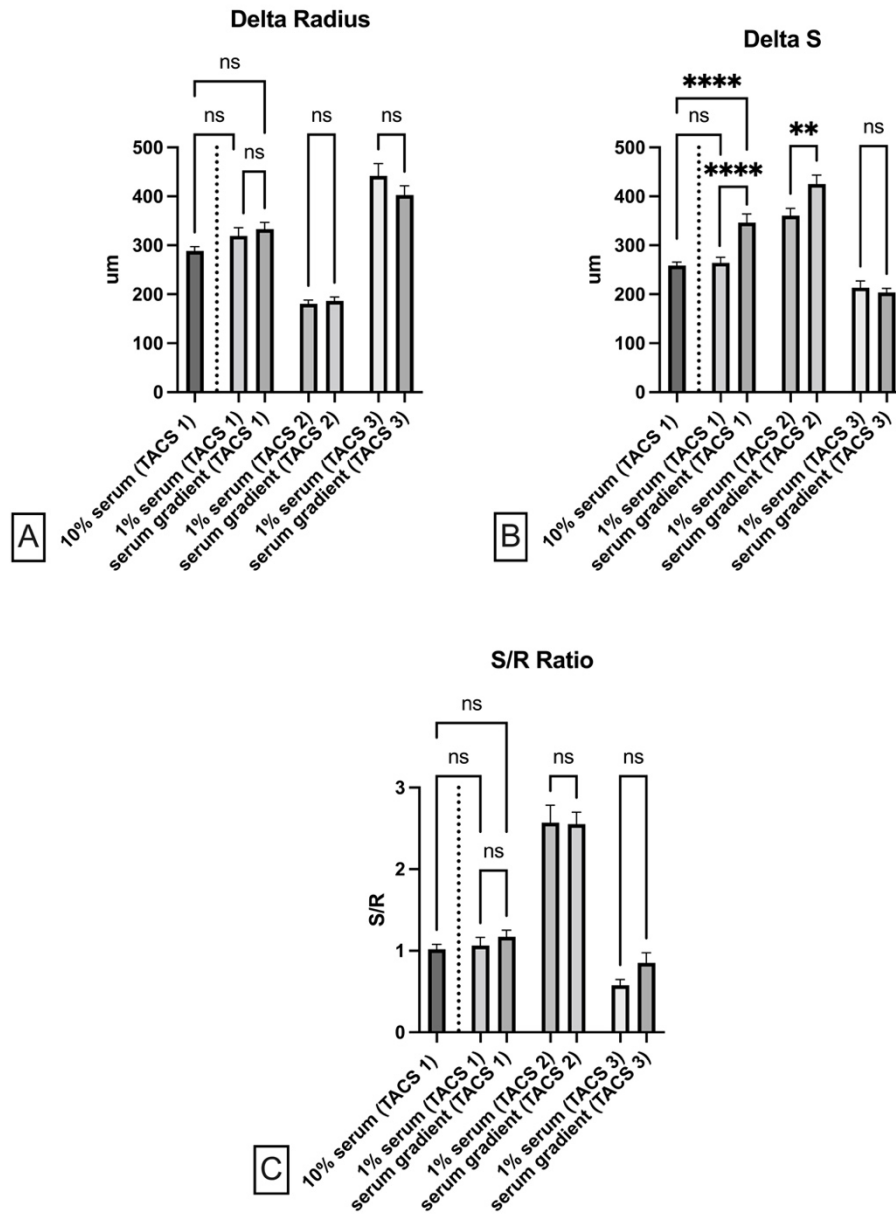


Figure 73: R, S, and S/R comparison between 1% serum and serum gradient

Delta radius, delta S and S/R quantified for and compared between 1% serum and serum gradient experiments. A) Cells display no change in radial migration across all TACS scenarios when comparing between 1% serum and serum gradient conditions B) Cells exposed to a serum gradient travel significantly further circumferentially in TACS 1 and TACS 2, but not TACS 3. C) Cells in all groups display no significant differences in S/R ratio between 1% serum and serum gradient experiments.

Next, we assessed track displacement, cell displacement, persistence, and velocity between 1% serum and serum gradient groups. In Figure 74 panel A, the data show that cells in the TACS 3 serum gradient group display a shorter average track displacement than the TACS 3 1% serum group. Panel B, 3T3s show an overall increase in cell displacement in TACS 1 and TACS 2 groups caused by the increase in delta S shown in Figure 73B. 3T3s display decreased persistence on all TACS conditions when exposed to a serum gradient (Figure 74C), and finally, 3T3s travel faster on the TACS 2 condition when exposed to a serum gradient. Although there are a few slight but significant differences in migration characteristics when comparing between 1% serum and serum gradient conditions, they are not consistent enough across all metrics to conclusively say that cell behavior is altered between the two groups. In fact, the effects of a serum gradient produce results inverse to our initial expectations.

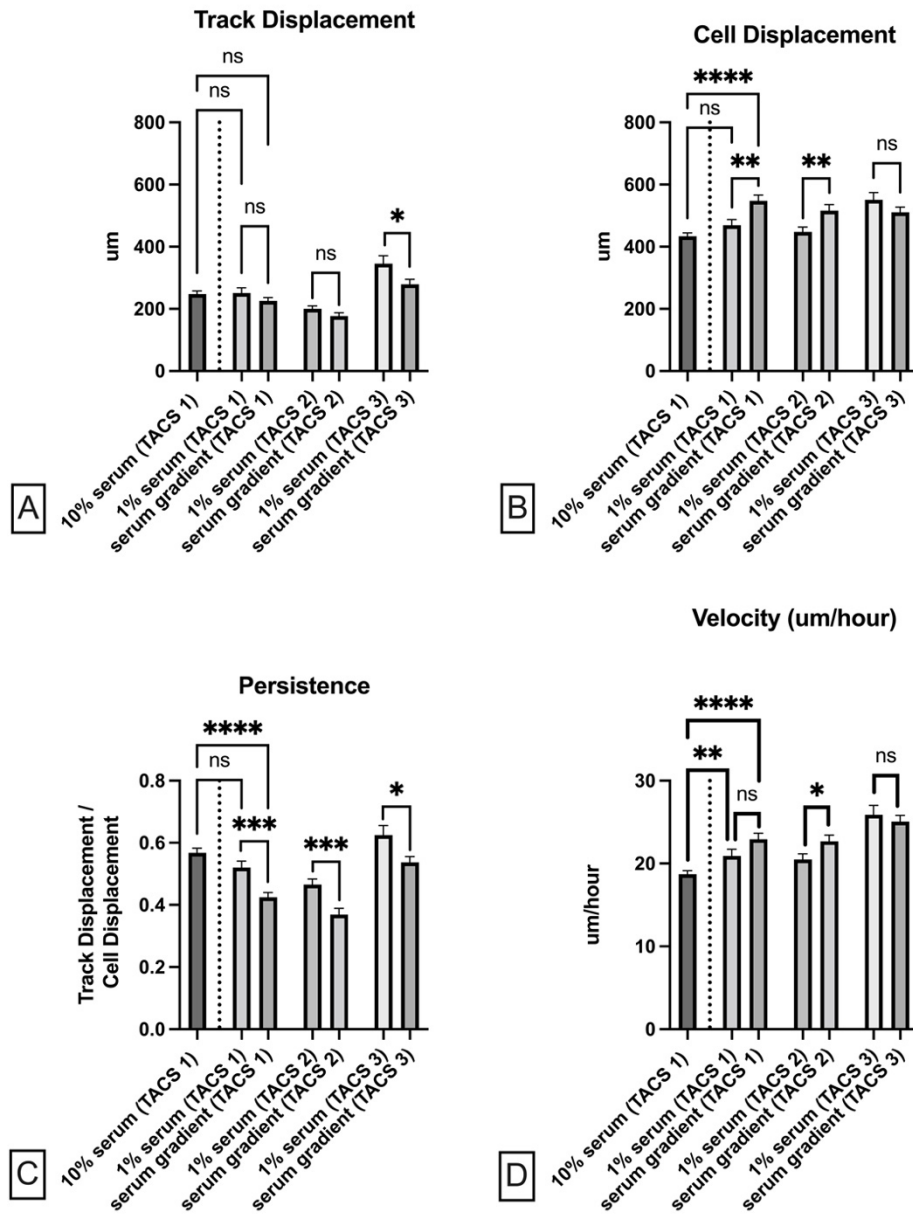


Figure 74: Displacement, persistence, and velocity comparison between 1% serum and serum gradient experiments

Track displacement, cell displacement, persistence and velocity quantified for cells across TACS 1, 2, and 3 groups between 1% serum and serum gradient conditions. A) Cells in TACS 3 display lower track displacement when exposed to a serum gradient. B) Cell displacement is notably higher

in serum gradient conditions on TACS 1 and TACS 2 substrates. C) Overall, cells display decreased persistence in TACS 1, 2, and 3 when exposed to a serum gradient. D) Cells on the TACS 2 display higher average velocity in TACS 2 when exposed to a serum gradient.

5.5 Discussion

To conclude, we developed a novel migration assay to mimic the mechanical cues presented by TACS organizations in tumor development. We utilized oval micropillars to mimic these TACS arrangements and integrated these substrates within a novel microfluidic device which allows chemotactic gradient generation across the migration area. We demonstrate that 3T3s are significantly responsive to the anisotropic stiffness and contact guidance cues presented by oval micropillars in TACS simulating designs even in a low serum environment. 3T3s exhibit random migration on our TACS 1 (isotropic/circular micropillars only) design, prefer migrating circumferentially on the TACS 2 (circumferential oval design), and travel, with high persistence and greater velocity, radially outward on the TACS 3 (radial ovals) substrate.

To build on our characterization of cell migratory response to TACS mimicking anisotropic micropillar arrangements, we next introduced chemotactic gradients. The data show inconclusive results when comparing between 1% serum and serum gradient conditions. In fact, the data collected display trends opposite to predicted outcomes by way of increasing circumferential migration (ΔS), rather than influencing cells to migrate outward radially. From this, we conclude that the chemotactic gradient is not influencing cells as expected. Further investigation is needed to elucidate this response. In this chapter, we have successfully created a migration assay that recapitulates the mechanical cues and chemotactic gradients present in TACS 1, TACS 2, and TACS 3 and demonstrate how these complex signals influence cell migration in the developing tumor microenvironment.

Chapter 6

Summary and Future Directions

To summarize, the goal of this work was to elucidate the role of anisotropic stiffness and contact guidance cues in the tumor microenvironment. We develop two novel assays to mimic the mechanical cues presented by various collagen arrangements (TACS) in the tumor microenvironment. We began by developing a novel substrate capable of simulating isotropic and anisotropic tissues. Circular cross section micropillars were utilized to present isotropic mechanical cues to cells and oval micropillars were used to present cells with anisotropic stiffness and contact guidance cues. These two micropillar designs were combined onto a single substrate to allow for a side-by-side comparison of how varied mechanical properties can influence key cellular characteristics such as cell size, alignment, traction forces, and ECM assembly. Using the knowledge we gained in early chapters, we wanted to build on our investigation of the effect of anisotropic stiffness on static cells by developing a unique migration assay using oval micropillars. We strived to investigate how anisotropic stiffness and collagen organization influence cell migration in early, mid, and late-stage tumors. Circular and oval micropillars were used, in combination to recreate the ECM mechanics of collagen architectures in TACS 1, TACS 2, and

TACS 3. Ultimately, our goal was to integrate these substrate designs into a microfluidic device to also simulate chemotactic gradients across the migration area. The studies were intended to elucidate the interplay between ECM mechanics and chemotactic gradients at various stages of tumor development.

Chapter 3

We began, in chapter 3, by simply assessing NIH-3T3 and ASC (fibroblast cell lines) response to anisotropic stiffness. NIH-3T3s and ASCs were seeded on our novel dual stiffness substrate to investigate differences in cell size, alignment, traction force, and ECM assembly. Our initial investigation demonstrated that anisotropic stiffness results in larger cells that self-align to the direction of greatest stiffness (major axis of oval micropillars), generate larger traction forces, and assemble significantly greater ECM. We then aimed to elucidate the mechanism behind these responses and logically decide to probe the role of traction forces in cellular mechanoresponse. We utilized the well-known force mediators, Y-27632 and blebbistatin, to downregulate traction forces, and MDA-MB-231 conditioned media to upregulate force and observed fibroblast response.

Generally, our findings show that cells on anisotropic stiffness substrates exhibit larger cell areas and increased alignment. Downregulating force resulted in decreased cell area, alignment, and ECM assembly, while upregulating force showed a marked increase in these characteristics. An important point to note, which is evidenced by the data, is that all fibroblast cell lines may not respond to anisotropic stiffness and modulation of traction force similarly. In our case, we notice that ASCs are much more responsive to anisotropic stiffness, indicated primarily by exceptional alignment, than 3T3s. We suspect that ASCs' larger size and ability to generate larger forces is

responsible for this difference. The larger size would provide a larger area to be in contact with anisotropic stiffness, essentially providing a stronger signal, and larger forces also support better sensing of the mechanical environment. ASCs were also much more responsive to the force modulation treatments than 3T3s. When treated with Y-27632 or blebbistatin, they showed greater decreases in force, ECM assembly and alignment than 3T3s, and greater increases in force and ECM assembly when treated with 231CM. In summary, we demonstrated that anisotropic stiffness can be used to induce cell alignment, and that downregulation of force inhibits this response.

Chapter 4

Next, as a real-world case, we strived to investigate how aligned collagen fibers in the tumor microenvironment influence malignant cell behavior. We have already demonstrated that our anisotropic stiffness substrate can be used to influence cell alignment and ECM assembly. To study the effects of anisotropic stiffness in the tumor microenvironment, mammary epithelial cell lines of increasing malignancy were seeded on oval micropillars. Cell lines of increasing malignancy were chosen to represent a model of progressive breast cancer and investigate the correlation between malignancy and mechanosensing. We seeded MCF10A (healthy), MCF10AT1 (malignant), and MDA-MB-231 (metastatic) cell lines on our novel dual substrate and assessed cell size, alignment, force and ECM assembly. In the tumor microenvironment, healthy epithelial cells are often activated by inflammatory cytokines and transform into a mesenchymal phenotype. This process is known as epithelial-mesenchymal transition (EMT). Cells that have undergone EMT display spindle like morphology, increased motility, and increased ECM assembly, and are key in mediating collagen reorganization in tumor growth. To simulate this transformation *in vitro*, we subjected the epithelial cell lines to treatment with MDA-MB-231 conditioned media. We previously demonstrated 231CM's ability upregulate mechanoresponse

and ECM assembly in fibroblast cell lines. Y-27632 was used to test whether the downregulation of force could be used to counteract the effects of 231CM treatment.

Our results show that epithelial cell lines are much less responsive than fibroblasts, to anisotropic stiffness. Beginning with MCF10As (healthy), 10As show minimal changes in response to 231CM treatment, however, when treated with both 231CM and Y-27632 (231CM + Y-27632 group), they display decreased cell size, decreased FN assembly, and decreased total force. In the control condition, 10As display randomized alignment on oval micropillars. Treatment with 231CM enhances alignment significantly, and the addition of Y-27632 disrupts this alignment.

Moving on to the premalignant cell line, AT1s display a similar lack of response to anisotropic stiffness, but a distinctly different response to chemotactic treatments. AT1s displayed increased cell area and total force when exposed to inflammatory cytokines (231 CM), but these changes were not ameliorated with the addition of Y-27632. AT1s failed to show any significant alignment on oval micropillars. Finally, we analyzed MDA-MB-231(metastatic) mechanoresponse and again noticed a lack of significant differences in the control condition between isotropic and anisotropic substrates. Treatment conditions were adjusted for MDA-MB-231s due to the presumption of autocrine and paracrine signaling of expressed inflammatory cytokines. 231 experiments were thereby conducted in control and Y-27632 conditions. The data show that Y-27632 seems to produce the opposite effect of what was observed in 10As, in 231s. Y-27632 treatment of 231s resulted in increased cell area, decreased FN assembly, increased total force, and no difference in alignment on oval micropillars. These odd results indicate a decrease in mechanoresponse is correlated with increasing malignancy. Overall, the data suggest that epithelial cell lines are minimally responsive to anisotropic stiffness, and while healthy epithelial cells

(10As) are responsive to chemotactic treatment with 231CM and Y-27632 in the expected fashion, malignant cells display increased cell area and total force in response to 231CM, and Y-27632 did not downregulate the response as it did in 10As. Metastatic cells (231s), to our surprise, displayed increased cell area and total force when treated with Y-27632. Unfortunately, our data does not allow us to report any conclusive response to anisotropic stiffness.

Chapter 5

The end goal of our work was to develop substrates to mimic TACS 1, TACS 2, and TACS 3 collagen architectures to investigate the role of anisotropic stiffness and contact guidance in metastasis. Our background investigation of the signals present in the tumor microenvironment led us to find that, in addition to mechanical cues, there are many chemotactic cues that also influence metastasis. To produce the most accurate representation of migratory signals in the tumor microenvironment, we strived to develop a system which would integrate TACS-mimicking substrates into a microfluidic device capable of generating a chemotactic gradient across the migration area. We designed three substrates with unique arrangements of isotropic (circular) and anisotropic (oval) micropillars to mimic TACS 1, 2, AND 3. TACS 1, or dense unorganized collagen fibers, was simulated by having isotropic micropillars in both the seeding and migration areas. TACS 2, circumferentially aligned collagen fibers encapsulating the central cell mass, was simulated using isotropic micropillars in the seeding area and anisotropic micropillars arranged with the major axis aligned circumferentially around the central seeding area. TACS 3, collagen fibers leading radially outward from the central cell mass, was recreated using anisotropic micropillars arranged in radial lines leading away from the seeding area. For proof of concept, fibroblasts, NIH-3T3s, were used to validate the designs due to their proven ability to respond to anisotropic mechanical cues. The data confirm significant differences in migration characteristics

on the different TACS-mimicking substrates. Cell tracks were analyzed for distance traveled radially (R), distance traveled circumferentially (S), S/R ratio, track displacement, cell displacement, persistence, and velocity. 3T3s on the TACS 1 substrate display randomized alignment confirmed by a S/R ratio of approximately 1. When seeded on the TACS 2 design, the cells display significantly greater migration in the circumferential direction, which was confirmed by a S/R ratio (~2.5) significantly greater than the TACS 1 control. On the TACS 3 design 3T3s migrate radially outward with high persistence and increased velocity, again confirmed by a low S/R ratio (~0.5). Comparison between no gradient and serum gradient conditions yielded minimal differences in migration characteristics, but the differences observed were opposite to our initial expectation that a chemotactic gradient would enhance radial migration. Further investigation is needed to shed light on the mechanisms behind this response. Ultimately, we demonstrate that our anisotropic micropillar designs are capable of mimicking the migration characteristics provided by collagen fibers in the tumor microenvironment.

In conclusion, we developed two novel tools to investigate the effects of anisotropic stiffness on cell behavior. We demonstrated that oval micropillars can be used to simulate anisotropic stiffness and contact guidance and can have profound effects, in fibroblast cell lines, on cell size, extracellular matrix assembly, traction force, alignment and cell migration. We hope that these tools will be used by future researchers to investigate other *in vivo* scenarios in which unique mechanical cues or ECM architectures may be found.

Future directions

The tools developed in this work provide many avenues for future development. In the tumor microenvironment, inflammatory cytokines expressed by malignant cells activate resident fibroblasts to reorganize and deposit new ECM. Our work in chapter 3 investigated the effects of downregulating and upregulating force on fibroblast mechanoresponse. The next logical step would be to investigate if downregulation of force, using Y-27632 or blebbistatin, can be used to normalize fibroblast response after activation with 231CM. As we went on to demonstrate in chapter 3, that there are significant differences in mechanoresponse between just two fibroblast cell lines. We hope future researchers will continue to characterize and catalog mechanoresponse in other cell lines to in attempt to establish a mechanoresponse database. The ability of our design to be easily modified to present different substrate stiffness and different arrangements of anisotropic oval micropillars lends itself to be used for a variety of mechanical scenarios.

Next, we hope others will continue to investigate the correlation between anisotropic stiffness, level of malignancy, and response to inflammatory cytokines. For our work in chapter 4, we chose 3 cell lines out of hundreds of different malignant cell lines. We believe, due to the infinite combinations of genetic mutations that can occur to create malignant cells, that there would be merit in investigating the mechanoresponse of other malignant cell lines. We also postulate that since epithelial and fibroblast cell lines coexist in healthy tissue and the tumor microenvironment that there would be some interesting findings in seeding a mixed cell population on our anisotropic substrate.

Lastly, we believe that our microfluidic migration assay sets up endless possibilities to investigate migration with respect to different tissue architectures and ECM organizations. Understandably, some work needs to be done to refine the chemotactic gradient formation in the assay, but we believe that this can be accomplished with a few simple design modifications. In

chapter 5, we utilize one fibroblast cell line to demonstrate that our mechanical designs produce the intended cellular response. The ultimate goal for this assay was to elucidate the mechanisms behind metastatic migration. Many works have indicated that inflammatory cytokines expressed by malignant cells influence fibroblasts in the surrounding tissue to assist in ECM turnover as a tumor grows. This scenario could be recapitulated by seeding a mixed cell population, for example NIH-3T3s and MDA-MB-231s and assessing migration characteristics. We also hope that our migration assay will serve as a platform to test new methods or treatments against metastasis.

References

- 1 Heron M. *National Vital Statistics Reports Volume 68, Number 6, June 24, 2019, Deaths: Leading Causes for 2017*. 2019.
- 2 Siegel RL, Miller KD, Jemal A. Cancer statistics, 2020. *CA Cancer J Clin* 2020;**70**:7–30. <https://doi.org/10.3322/caac.21590>.
- 3 Society AC. Cancer Facts & Figures 2020 2020.
- 4 Oudin MJ, Weaver VM. Physical and Chemical Gradients in the Tumor Microenvironment Regulate Tumor Cell Invasion, Migration, and Metastasis. *Cold Spring Harb Symp Quant Biol* n.d.;**LXXXI**:189. <https://doi.org/10.1101/sqb.2016.81.030817>.
- 5 Roussos ET, Condeelis JS, Patsialou A. Chemotaxis in cancer. *Nat Rev Cancer* 2011;**11**:573. <https://doi.org/10.1038/nrc3078>.
- 6 Wang S-J, Saadi W, Lin F, Nguyen CM-C, Jeon NL. Differential effects of EGF gradient profiles on MDA-MB-231 breast cancer cell chemotaxis. *Exp Cell Res* 2004;**300**:180–9. <https://doi.org/10.1016/j.yexcr.2004.06.030>.
- 7 Provenzano PP, Inman DR, Eliceiri KW, Knittel JG, Yan L, Rueden CT, *et al*. Collagen density promotes mammary tumor initiation and progression. *BMC Med* 2008;**6**:11. <https://doi.org/10.1186/1741-7015-6-11>.
- 8 Boyd NF, Guo H, Martin LJ, Sun L, Stone J, Fishell E, *et al*. Mammographic density and the risk and detection of breast cancer. *N Engl J Med* 2007;**356**:227–36. <https://doi.org/10.1056/NEJMoa062790>.
- 9 Provenzano PP, Eliceiri KW, Campbell JM, Inman DR, White JG, Keely PJ. Collagen reorganization at the tumor-stromal interface facilitates local invasion 2006.

- <https://doi.org/10.1186/1741-7015-4-38>.
- 10 Conklin MW, Eickhoff JC, Riching KM, Pehlke CA, Eliceiri KW, Provenzano PP, *et al*. Aligned collagen is a prognostic signature for survival in human breast carcinoma. *Am J Pathol* 2011;**178**:1221–32. <https://doi.org/10.1016/j.ajpath.2010.11.076>.
 - 11 Isenberg BC, Backman DE, Kinahan ME, Jesudason R, Suki B, Stone PJ, *et al*. Micropatterned cell sheets with defined cell and extracellular matrix orientation exhibit anisotropic mechanical properties. *J Biomech* 2012;**45**:756–61. <https://doi.org/10.1016/j.jbiomech.2011.11.015>.
 - 12 Provenzano PP, Eliceiri KW, Inman DR, Keely PJ. Engineering Three-Dimensional Collagen Matrices to Provide Contact Guidance during 3D Cell Migration. *Curr Protoc Cell Biol* 2010;**47**:10.17.1-10.17.11. <https://doi.org/10.1002/0471143030.cb1017s47>.
 - 13 Oliveira AL, Sun L, Kim HJ, Hu X, Rice W, Kluge J, *et al*. Aligned silk-based 3-D architectures for contact guidance in tissue engineering. *Acta Biomater* 2012;**8**:1530–42. <https://doi.org/10.1016/j.actbio.2011.12.015>.
 - 14 Sochol RD, Higa AT, Janairo RRR, Li S, Lin L. Unidirectional mechanical cellular stimuli via micropost array gradients. *Soft Matter* 2011;**7**:4606–9. <https://doi.org/10.1039/c1sm05163f>.
 - 15 Au FWF, Ghai S, Lu FI, Moshonov H, Crystal P. Quantitative shear wave elastography: Correlation with prognostic histologic features and immunohistochemical biomarkers of breast cancer. *Acad Radiol* 2015;**22**:269–77. <https://doi.org/10.1016/j.acra.2014.10.007>.
 - 16 Fenner J, Stacer AC, Winterroth F, Johnson TD, Luker KE, Luker GD. Macroscopic Stiffness of Breast Tumors Predicts Metastasis. *Sci Rep* 2015;**4**:5512. <https://doi.org/10.1038/srep05512>.

- 17 Acevedo-Acevedo S, Crone WC. Substrate stiffness effect and chromosome missegregation in hIPS cells. *J Negat Results Biomed* 2015;**14**:
<https://doi.org/10.1186/S12952-015-0042-8>.
- 18 Fu J, Wang Y-K, Yang MT, Desai RA, Yu X, Liu Z, *et al*. Mechanical regulation of cell function with geometrically modulated elastomeric substrates n.d.
<https://doi.org/10.1038/nmeth.1487>.
- 19 Engler AJ, Sen S, Sweeney HL, Discher DE. Matrix Elasticity Directs Stem Cell Lineage Specification. *Cell* 2006;**126**:677–89. <https://doi.org/10.1016/j.cell.2006.06.044>.
- 20 Leight JL, Wozniak MA, Chen S, Lynch ML, Chen CS. Matrix rigidity regulates a switch between TGF- β 1-induced apoptosis and epithelial–mesenchymal transition. *Mol Biol Cell* 2012;**23**:781–91. <https://doi.org/10.1091/mbc.e11-06-0537>.
- 21 Griggs LA, Hassan NT, Malik RS, Griffin BP, Martinez BA, Elmore LW, *et al*. Fibronectin fibrils regulate TGF- β 1-induced Epithelial-Mesenchymal Transition. *Matrix Biol* 2017;**60–61**:157–75. <https://doi.org/10.1016/j.matbio.2017.01.001>.
- 22 Saxena M, Christofori G. Rebuilding cancer metastasis in the mouse. *Mol Oncol* 2013:283–96. <https://doi.org/10.1016/j.molonc.2013.02.009>.
- 23 Friedl P, Wolf K. Tumour-cell invasion and migration: Diversity and escape mechanisms. *Nat Rev Cancer* 2003;**3**:362–74. <https://doi.org/10.1038/nrc1075>.
- 24 Wang S-J, Saadi W, Lin F, Connie M-C, Nguyen N, Li J. Differential effects of EGF gradient profiles on MDA-MB-231 breast cancer cell chemotaxis 2004.
<https://doi.org/10.1016/j.yexcr.2004.06.030>.
- 25 Zhang H, Lin F, Huang J, Xiong C. Anisotropic stiffness gradient-regulated mechanical guidance drives directional migration of cancer cells. *Acta Biomater* 2020;**106**:181–92.

- <https://doi.org/10.1016/j.actbio.2020.02.004>.
- 26 Breckenridge MT, Desai RA, Yang MT, Fu J, Chen CS. Substrates with Engineered Step Changes in Rigidity Induce Traction Force Polarity and Durotaxis. *Cell Mol Bioeng* 2014;**7**:26–34. <https://doi.org/10.1007/s12195-013-0307-6>.
- 27 Riching KM, Cox BL, Salick MR, Pehlke C, Riching AS, Ponik SM, *et al.* 3D Collagen Alignment Limits Protrusions to Enhance Breast Cancer Cell Persistence. *Biophys J* 2014;**107**:2546–58. <https://doi.org/10.1016/j.bpj.2014.10.035>.
- 28 Carey SP, Kraning-Rush CM, Williams RM, Reinhart-King CA. Biophysical control of invasive tumor cell behavior by extracellular matrix microarchitecture. *Biomaterials* 2012;**33**:4157–65. <https://doi.org/10.1016/j.biomaterials.2012.02.029>.
- 29 Ray A, Slama ZM, Morford RK, Madden SA, Provenzano PP. Enhanced Directional Migration of Cancer Stem Cells in 3D Aligned Collagen Matrices. *Biophys J* 2017;**112**:1023–36. <https://doi.org/10.1016/j.bpj.2017.01.007>.
- 30 Islam A, Younesi M, Mbimba T, Akkus O. Collagen Substrate Stiffness Anisotropy Affects Cellular Elongation, Nuclear Shape and Stem Cell Fate towards Anisotropic Tissue Lineage n.d. <https://doi.org/10.1002/adhm.201600284>.
- 31 Xu B, Chow M-J, Zhang Y. Experimental and Modeling Study of Collagen Scaffolds with the Effects of Crosslinking and Fiber Alignment. *Int J Biomater* 2011;**2011**:12. <https://doi.org/10.1155/2011/172389>.
- 32 Provenzano PP, Eliceiri KW, Keely PJ. Multiphoton microscopy and fluorescence lifetime imaging microscopy (FLIM) to monitor metastasis and the tumor microenvironment. *Clin Exp Metastasis* 2009:357–70. <https://doi.org/10.1007/s10585-008-9204-0>.
- 33 Pham JT, Xue L, Del Campo A, Salierno M. Guiding cell migration with microscale

- stiffness patterns and undulated surfaces 2016.
<https://doi.org/10.1016/j.actbio.2016.04.031>.
- 34 Pang Y, Wang X, Lee D, Greisler HP. Dynamic quantitative visualization of single cell alignment and migration and matrix remodeling in 3-D collagen hydrogels under mechanical force. *Biomaterials* 2011;**32**:3776–83.
<https://doi.org/10.1016/j.biomaterials.2011.02.003>.
- 35 Tse JR, Engler AJ. Preparation of Hydrogel Substrates with Tunable Mechanical Properties. *Curr Protoc Cell Biol* 2010;**47**:10.16.1-10.16.16.
<https://doi.org/10.1002/0471143030.cb1016s47>.
- 36 Isenberg BC, DiMilla PA, Walker M, Kim S, Wong JY. Vascular Smooth Muscle Cell Durotaxis Depends on Substrate Stiffness Gradient Strength. *Biophys J* 2009;**97**:1313–22.
<https://doi.org/10.1016/j.bpj.2009.06.021>.
- 37 Joo S, Yeon Kim J, Lee E, Hong N, Sun W, Nam Y. Effects of ECM protein micropatterns on the migration and differentiation of adult neural stem cells. *Sci Rep* 2015;**5**:13043. <https://doi.org/10.1038/srep13043>.
- 38 Lagunas A, Rolli CG, Shakesheff K, Cavalcanti-Adam EA, Hauff K, Zambarda C, *et al*. Matrix-immobilized BMP-2 on microcontact printed fibronectin as an in vitro tool to study BMP-mediated signaling and cell migration 2015.
<https://doi.org/10.3389/fbioe.2015.00062>.
- 39 Du Y, Woo HK, Li L, Mak KY, Wong CM, Shi J, *et al*. Effect of bi-directional microfabricated topographical cues on cellular behavior of mammalian cell line 2014.
<https://doi.org/10.1016/j.mee.2014.04.010>.
- 40 Sochol RD, Higa AT, Janairo RRR, Chou A, Li S, Lin L. UNIDIRECTIONAL

- CELLULAR DUROTAXIS VIA MICROFABRICATED POSTS OF VARYING ANISOTROPY. *TRANSDUCERS 2009 - 2009 Int Solid-State Sensors, Actuators Microsystems Conf* 2009;604–7. <https://doi.org/10.1109/sensor.2009.5285397>.
- 41 Saez A, Ghibaudo M, Buguin A, Silberzan P, Ladoux B. Rigidity-driven growth and migration of epithelial cells on microstructured anisotropic substrates. *Proc Natl Acad Sci* 2007;**104**:8281–6. <https://doi.org/10.1073/pnas.0702259104>.
- 42 Lemmon CA, Chen CS, Romer LH. Cell Traction Forces Direct Fibronectin Matrix Assembly. *Biophys J* n.d.;**96**:729–38. <https://doi.org/10.1016/j.bpj.2008.10.009>.
- 43 Lemmon CA, Chen CS, Romer LH. Cell Traction Forces Direct Fibronectin Matrix Assembly. *Biophys J* 2009;**96**:729–38. <https://doi.org/10.1016/j.bpj.2008.10.009>.
- 44 Scott LE, Mair DB, Narang JD, Feleke K, Lemmon CA. Fibronectin fibrillogenesis facilitates mechano-dependent cell spreading, force generation, and nuclear size in human embryonic fibroblasts. *Integr Biol* 2015;**7**:1454–65. <https://doi.org/10.1039/c5ib00217f>.
- 45 Ghibaudo M, Saez A, Trichet L, Xayaphoummine A, Browaeys J, Silberzan P, *et al.* Traction forces and rigidity sensing regulate cell functions. *Soft Matter* 2008;**4**:1836–43. <https://doi.org/10.1039/b804103b>.
- 46 Ray A, Slama ZM, Morford RK, Madden SA, Provenzano PP. Enhanced Directional Migration of Cancer Stem Cells in 3D Aligned Collagen Matrices. *Biophys J* 2017;**112**:1023–36. <https://doi.org/10.1016/j.bpj.2017.01.007>.
- 47 Katsumi A, Orr AW, Tzima E, Schwartz MA. Integrins in Mechanotransduction* 2004. <https://doi.org/10.1074/jbc.R300038200>.
- 48 Jaalouk DE, Lammerding J. Mechanotransduction gone awry. *Nat Rev Mol Cell Biol* 2009;63–73. <https://doi.org/10.1038/nrm2597>.

- 49 Serbo J V, Kuo S, Lewis S, Lehmann M, Li J, Gracias DH, *et al.* Patterning of Fibroblast and Matrix Anisotropy within 3D Confinement is Driven by the Cytoskeleton. *Adv Healthc Mater* 2016;**5**:146–58. <https://doi.org/10.1002/adhm.201500030>.
- 50 Re'em T, Kaminer-Israeli Y, Ruvinov E, Cohen S. Chondrogenesis of hMSC in affinity-bound TGF-beta scaffolds 2011. <https://doi.org/10.1016/j.biomaterials.2011.10.007>.
- 51 Eslaminejad MB, Karimi N, Shahhoseini M. Chondrogenic differentiation of human bone marrow-derived mesenchymal stem cells treated by GSK-3 inhibitors. *Histochem Cell Biol* 2013;**140**:623–33. <https://doi.org/10.1007/s00418-013-1121-x>.
- 52 Ramirez AM, Wongtrakool C, Welch T, Steinmeyer A, Zügel U, Roman J. Vitamin D inhibition of pro-fibrotic effects of transforming growth factor β 1 in lung fibroblasts and epithelial cells. *J Steroid Biochem Mol Biol* 2010;**118**:142–50. <https://doi.org/10.1016/j.jsbmb.2009.11.004>.
- 53 Julian L, Olson MF. Rho-associated coiled-coil containing kinases (ROCK), structure, regulation, and functions. *Small GTPases* 2014. <https://doi.org/10.4161/sgtp.29846>.
- 54 Kovács M, Tóth J, Hetényi C, Málnási-Csizmadia A, Seller JR. Mechanism of blebbistatin inhibition of myosin II. *J Biol Chem* 2004;**279**:35557–63. <https://doi.org/10.1074/jbc.M405319200>.
- 55 Wessels DJ, Pradhan N, Park YN, Klepitsch MA, Lusche DF, Daniels KJ, *et al.* Reciprocal signaling and direct physical interactions between fibroblasts and breast cancer cells in a 3D environment. *PLoS One* 2019;**14**:. <https://doi.org/10.1371/JOURNAL.PONE.0218854>.
- 56 Acerbi I, Cassereau L, Dean I, Shi Q, Au A, Park C, *et al.* Human breast cancer invasion and aggression correlates with ECM stiffening and immune cell infiltration. *Integr Biol*

- (United Kingdom) 2015;7:1120–34. <https://doi.org/10.1039/c5ib00040h>.
- 57 Li J, Wu Y, Schimmel N, Al-Ameen MA, Ghosh G. Breast cancer cells mechanosensing in engineered matrices: Correlation with aggressive phenotype. *J Mech Behav Biomed Mater* 2016;**61**:208–20. <https://doi.org/10.1016/j.jmbbm.2016.01.021>.
- 58 Zhang H, Lin F, Huang J, Xiong C. Anisotropic stiffness gradient-regulated mechanical guidance drives directional migration of cancer cells. *Acta Biomater* 2020. <https://doi.org/10.1016/j.actbio.2020.02.004>.
- 59 Designed Research; W LLH, Performed Research; W LLH. Oriented collagen fibers direct tumor cell intravasation 2016;**113**:11208–13. <https://doi.org/10.1073/pnas.1610347113>.
- 60 Madar S, Goldstein I, Rotter V. 'Cancer associated fibroblasts'-more than meets the eye n.d. <https://doi.org/10.1016/j.molmed.2013.05.004>.
- 61 Guo L, Zhang Y, Zhang L, Huang F, Li J, Wang S. MicroRNAs, TGF- β signaling, and the inflammatory microenvironment in cancer. *Tumour Biol* 2016;**37**:115–25. <https://doi.org/10.1007/s13277-015-4374-2>.
- 62 Imbalzano KM, Tatarkova I, Imbalzano AN, Nickerson JA. Increasingly transformed MCF-10A cells have a progressively tumor-like phenotype in three-dimensional basement membrane culture 2009. <https://doi.org/10.1186/1475-2867-9-7>.
- 63 Santner SJ, Dawson PJ, Tait L, Soule HD, Eliason J, Mohamed AN, *et al.* *Malignant MCF10CA1 cell lines derived from premalignant human breast epithelial MCF10AT cells*. vol. 65. 2001.
- 64 Kim BJ, Hannanta-anan P, Chau M, Kim YS, Swartz MA, Wu M. Cooperative Roles of SDF-1 α and EGF Gradients on Tumor Cell Migration Revealed by a Robust 3D

- Microfluidic Model. *PLoS One* 2013;**8**:e68422.
<https://doi.org/10.1371/journal.pone.0068422>.
- 65 McLane JS, Ligon LA. Stiffened Extracellular Matrix and Signaling from Stromal Fibroblasts via Osteoprotegerin Regulate Tumor Cell Invasion in a 3-D Tumor in Situ Model. *Cancer Microenviron* 2016;**9**:127–39. <https://doi.org/10.1007/s12307-016-0188-z>.
- 66 Peela N, Sam FS, Christenson W, Truong D, Watson AW, Mouneimne G, *et al.* A three dimensional micropatterned tumor model for breast cancer cell migration studies. *Biomaterials* 2016;**81**:72–83. <https://doi.org/10.1016/j.biomaterials.2015.11.039>.
- 67 Isenberg BC, Dimilla PA, Walker M, Kim S, Wong JY. Vascular Smooth Muscle Cell Durotaxis Depends on Substrate Stiffness Gradient Strength n.d.
<https://doi.org/10.1016/j.bpj.2009.06.021>.
- 68 Lo C-M, Wang H-B, Dembo M, Wang Y. Cell Movement Is Guided by the Rigidity of the Substrate. *Biophys J* 2000;**79**:144–52. [https://doi.org/10.1016/s0006-3495\(00\)76279-5](https://doi.org/10.1016/s0006-3495(00)76279-5).
- 69 Kim D-H, Seo C-H, Han K, Kwon KW, Levchenko A, Suh K-Y. Guided Cell Migration on Microtextured Substrates with Variable Local Density and Anisotropy. *Adv Funct Mater* 2009;**19**:1579–86. <https://doi.org/10.1002/adfm.200990041>.
- 70 Tinevez JY, Perry N, Schindelin J, Hoopes GM, Reynolds GD, Laplantine E, *et al.* TrackMate: An open and extensible platform for single-particle tracking. *Methods* 2017;**115**:80–90. <https://doi.org/10.1016/J.YMETH.2016.09.016>.

Curriculum Vitae

JITEN NARANG

narangjd@vcu.edu | (804) 510-9266
12201 Keats Grove Ct.
Glen Allen, VA 23059

Focused and self-motivated scientist who works well independently yet welcomes the opportunity to be part of a collaborative multidisciplinary team. Proven track record of developing novel cell-based assays to study biomechanical and biochemical phenomenon present in severe disease states. Strong expertise in microfabrication, microfluidics, and live cell immunofluorescence imaging. Seeking a position in the research and development of cell-based assays or point of care diagnostics.

EDUCATION

Virginia Commonwealth University

- Doctor of Philosophy in Biomedical Engineering GPA: 3.6
- Bachelor of Science in Biomedical Engineering GPA: 3.1
Minor Concentrations in Math and Physics

Richmond, VA

Expected Spring 2022
May 2012

RESEARCH EXPERIENCE

**Virginia Commonwealth University
VA**

Richmond,

Doctoral Candidate, Department of Biomedical Engineering
Present

Aug 2012 –

Advisor: Dr. Christopher Lemmon

Research Topics:

1. Analyzing traction forces and FN assembly in healthy and diseased tissues
 - Microfabricated micropillar arrays of various stiffness
 - Assessed differences between fibroblasts and myofibroblasts
 - Assessed differences across mammary epithelial cells of increasing malignancy
2. Influencing cellular orientation and migration utilizing anisotropic stiffness cues.
 - Developed a micropillar substrate to expose a single population of cells to anisotropic stiffness and isotropic stiffness simultaneously
 - Analyzed how anisotropic stiffness alters morphology and ECM assembly
3. Studying cell migration in a microfluidic model of metastasis.
 - Developed a novel microfluidic device to study how anisotropic

mechanical cues and chemotactic gradients in the tumor
microenvironment influence stromal invasion

Undergraduate Researcher, Department of Biomedical Engineering Sept 2011-
May 2012

Primary Investigator: Dr. Rebecca Heise

Research Summary: Developed a novel bioreactor to recapitulate conditions of the lung microenvironment. Our device allowed lung epithelial cells to be cultured at an air-liquid interface while also being exposed to cyclic radial strain. No other products on the market could reproduce these two phenomena concomitantly. Our work resulted in a provisional patent for our innovative bioreactor.

SKILLS

Laboratory Skills: Cell Culture, Immunofluorescence Microscopy, Live Cell Imaging, Microfabrication (Photolithography and Soft Lithography processes), Microfluidic Design and Assembly, Micro-Contact Printing, PDMS, Cryopreservation, Image Processing, Data Analysis, Gel Electrophoresis, Scanning Electron Microscopy, Protein Purification, Operating Shop Machinery

Computer Skills: MATLAB, Prism, ImageJ, SOLIDWORKS, CleWin, ZEN Imaging Software, LabView, Microsoft Office Suite, JMP

TEACHING EXPERIENCE

Virginia Commonwealth University **Richmond,**
VA

Teaching Assistant, Department of Biomedical Engineering Fall 2014,
Spring 2015

Course: Computational Methods

Assisted the professor by teaching lectures, holding weekly office hours and grading weekly assignments.

Guest Speaker, Course: Cellular Mechanics and Mechanobiology Spring 2015,
Spring 2016

Topic: Methods to measure cellular traction forces

MENTORING EXPERIENCE

Virginia Commonwealth University **Richmond,**
VA

Research mentor, Dean's Undergraduate Research Initiative Spring 2014 –
Fall 2014

Designed a research project, trained, and mentored an undergraduate researcher in the areas of laboratory techniques, data collection, and conference preparation. Investigated the ability of bone morphogenic proteins (BMPs) to revert hepatic stellate cells activated by inflammatory cytokines such as transforming growth factor – beta 1 (TGF-B1).

Graduate Mentor, Graduate Student Mentorship Program
Spring 2015

Fall 2013 –

Mentored undergraduate students interested in pursuing a graduate career in the areas of resume development, undergraduate research experience, researching potential graduate schools, and PI selection.

PUBLICATIONS

Peer Reviewed Publications

1. Scott LE, Mair DB, **Narang JD**, Feleke K, Lemmon CA. Fibronectin Fibrillogenesis Facilitates Mechano-Dependent Cell Spreading, Force Generation, and Nuclear Size in Human Embryonic Fibroblasts. *Integr Biol (Camb)* 2015;7::1454–65.
2. Arsenovic PT, Ramachandran I, Bathula K, Zhu R, **Narang JD**, Noll NA, *et al.* Nesprin-2G, a Component of the Nuclear LINC Complex, Is Subject to Myosin-Dependent Tension. *Biophys J* 2016;110::34–43.

Manuscripts In Progress

1. **Narang JD**, Dalton CJ, Lemmon CA. Anisotropic Stiffness Micropillar Substrates Influence Fibroblast Alignment, Force Generation, and ECM assembly.
2. **Narang JD**, Lemmon CA. Elucidating The Role Of Biomechanical and Biochemical Cues In Malignant Cell Invasion Using A Novel Biomimetic Model Of The Tumor Microenvironment.

Abstracts

Oral Presentations

- The Virginia Academy of Science 2014, 2015

Poster Presentations

- Biomedical Engineering Society Meeting 2015
- Cellular and Molecular Bioengineering Meeting 2014
- Virginia Commonwealth University School of Engineering Research Symposium 2014

HONORS

- **Provisional Patent:** Extendable membrane bioreactor with an air-liquid interface. Spring 2012

EXTRACURRICULAR EXPERIENCE

- **Engineering Graduate Student Association (EGSA)**
2014 - 2016
 - Position: Risk Management Chair
 - Planned and organized social events for engineering graduate students
 - Ensured all events were conducted according to safety regulations determined by the university

PROFESSIONAL AFFILIATIONS

- **Biomedical Engineering Society** 2015 -
Present
- **Virginia Academy of Science** 2014 -
Present

REFERENCES

Christopher A. Lemmon PhD
Associate Professor, Associate Chair
Department of Biomedical Engineering
Virginia Commonwealth University
301 W Main St
Richmond, VA 23284
Clemmon@vcu.edu

Lauren A. Griggs PhD
Director of the Multicultural
Engineering Program
Pennsylvania State University
112 Hammond Building
State College, PA 16802
Lag5817@psu.edu